CRC Report No. AV-33-22

World Jet Fuel Survey Part 1: 2023-2024

Final Report

December 2025

COORDINATING RESEARCH COUNCIL, INC.
1 CONCOURSE PARKWAY • SUITE 800 • ATLANTA, GA 30328

The Coordinating Research Council, Inc. (CRC) is a non-profit corporation supported by the petroleum and automotive equipment industries with participation from other industries, companies, and governmental bodies on research programs of mutual interest. CRC operates through the committees made up of technical experts from industry and government who voluntarily participate. The five main areas of research within CRC are: air pollution (atmospheric and engineering studies); aviation fuels, lubricants, and equipment performance; heavy-duty vehicle fuels, lubricants, and equipment performance (e.g., diesel trucks); light-duty vehicle fuels, lubricants, and equipment performance (e.g., passenger cars); and sustainable mobility (e.g., decarbonization). CRC's function is to provide the mechanism for joint research conducted by industries that will help in determining the optimum combination of products. CRC's work is limited to research that is mutually beneficial to the industries involved. The final results of the research conducted by, or under the auspices of, CRC are available to the public.

University of Dayton Research Institute

World Jet Fuel Survey Part 1: 2023-2024

UDR-TR-2025-39

December 2025

Prepared for:

Federal Aviation Administration (FAA)
Center of Excellence: ASCENT Project 90

Ana Gabrielian
Engineer
Ana.B.Gabrielian@faa.gov

Prepared by:

University of Dayton Research Institute (UDRI)
Fuels & Energetic Materials Division

Shane Kosir, Amanda Mae Arts, Taylor Nicely, CJ Nesbit, Susan Mueller, April Landsaw, Maria Baker, Lisa Brown, Jim Thompson, Carlie Anderson, Linda Shafer, William H. Steinecker, Steven Zabarnick, Zachary J. West*

*GL Principal Chemical Engineer
Zachary.West@udri.udayton.edu

Table of Contents

1. Introduction

This report contains the results of a coordinated worldwide survey of current aviation turbine fuels (i.e., fuels at a refinery and not in the field or distribution systems) to support the development of a jet fuel technical property database. The project aims to: 1) provide a snapshot of physicochemical and performance properties of current jet fuels on the world market, 2) establish a baseline of fuel properties for comparison to new/synthetic fuels, and 3) become a reference benchmark of property data for designers, operators, producers, researchers, and other fuels practitioners. Where possible, comparisons are made with historical fuel data, primarily CRC Report 647 [1]. This report is organized into four sections: 1) an introduction, 2) certificate of analysis (CoA) data, 3) fit-for-purpose data, and 4) composition-to-property (C2P) modeling. The titles for Section 3 align with the Fit-for-Purpose Properties Table in ASTM D4054-23: "Standard Practice for Evaluation of New Aviation Turbine Fuels and Fuel Additives" [2]. In addition to fit-for-purpose property data, Section 3 contains specific test methods, errors, and instrumentation. Additional descriptions and analysis are available for select fit-for-purpose properties in the Appendix. The C2P modeling work in Section 4 demonstrates preliminary correlations between fuel chemistry and physicochemical properties. These models are meant to be illustrative, not definitive; more details about the models and the techniques used are included in Section 4.

The samples collected for this report were intended to be representative of 1) typical manufacturing conditions for jet fuel at the point of manufacture, and 2) representative of the batch of fuel being sampled. As such, sample providers were instructed to provide volumetric composite samples prepared from the upper, middle, and lower tank locations representative of a single batch of fuel and consistent with a sample used for certification purposes. The sample volume was nominally five (5) US gallons. The following steps were recommended for sample procurement, but local sampling procedures could also be used. Fuel producers were referred to EI/JIG 1530 [3] Chapter 4 on "Sampling and testing of aviation fuel" for specific guidance:

1. Samples should not be taken when environmental contaminants (e.g. rain, sand, dust, etc.) are present.
2. Prior to sampling, the sample apparatus and sample container shall be flushed and rinsed thoroughly at least three times with the product to be sampled, and all rinsings discarded before filling with the actual sample.
3. Samples should not be taken via stilling wells that may not contain product representative of the full batch.
4. Composite samples should be prepared in a clean, laboratory environment to avoid environmental contamination.

38 fuel samples were received between August 2023 and February 2024 for this study. Table *1* below shows fuel counts for each continent that provided samples (some values have been combined to anonymize sample providers). The fuels were primarily received from North America and Europe, with a limited contribution from Asia. The median batch volume is 2.9 US MGal, with 107 US MGal represented in total for all 38 samples. The jet fuel samples received consisted of 23 Jet A fuels and 15 Jet A-1 fuels [4] [5].

Table 1. Jet fuel sample set description.

Continent of Origin	**Fuel Count**	**Total Batch Volume (US MGal)**
North America	28	71
Europe	9	27
Asia	1	8

Three types of plots are used in this report to represent composition and property distributions: 1) box plots, 2) violin plots, and 3) histograms. The boxes on the box plots represent the interquartile range ($IQR = Q_3 - Q_1$), where Q_1 is the first quartile and Q_3 is the third quartile. The whiskers represent the last data points within the outlier threshold range. This threshold range is calculated as $threshold_{low} = Q1 - 1.5 \times IQR$ and $threshold_{high} = Q3 + 1.5 \times IQR$. When present, outlier measurements are represented by scatter points above and below the whiskers. Violin plots use a kernel density estimate (KDE) of the underlying distribution, which is represented as a curved vertical line. KDE produces what is essentially a smoothed histogram by placing a kernel function (in this case a Gaussian distribution) at each observation and summing the kernel values. A Gaussian KDE can handle non-normal data because it builds the distribution by summing many small Gaussian kernels at each data point, allowing the combined curve to approximate any overall shape, not just a normal one. The violin plots also include horizontal lines representing the IQR, which acts as a nested box plot. Histograms were used when only one data category was available for a property. Data from CRC Report 647 is shown on the distribution plots where available.

2. Certificate of Analysis Data

Jet A CoA Statistics

Table 2 shows Jet A CoA data provided by fuel suppliers compared to the specification limits from ASTM D1655-22a: "Standard Specification for Aviation Turbine Fuels" *[4]*. The specification limits are taken from Table 1: "Detailed Requirements of Aviation Turbine Fuels." This table has been formatted similar to those found in the 2013 PQIS Annual Report *[6]*. In addition to mean values, batch volume-weighted mean values are provided. These were calculated using Equation 1 where the $Volume_i$ is the batch volume for fuel i, $Property_i$ is the property value for fuel i, and n is the total number of fuels. Property counts are listed to account for the fact that some properties have CoA measurements for fewer than 38 fuels.

Equation 1. $$Volume\ Weighted\ Mean = \frac{\sum_{i=1}^{n}(Volume_i \times Property_i)}{\sum_{i=1}^{n} Volume_i}$$

Jet A fuels near/outside the specification limits included:

- One Jet A fuel had a mercaptan sulfur value at the maximum limit of 0.003 mass%.
- One Jet A fuel had a freezing point value at the maximum limit of -40°C.
- Smoke point had a weighted mean value of 23.0 mm, which is below the minimum specification limit of 25.0 mm. However, all the fuels had smoke point values above 18 mm, and the fuels with smoke point values between 18-25 mm had naphthalenes less than 3.0 vol%.
- Seven Jet A fuels had electrical conductivity below the minimum limit of 50 pS/m.

Table 2. Statistics for Jet A CoA data compared to specification limits from ASTM D1655.

Property	Specification Limits		Jet A CoA Data				
	Min	Max	Min	Max	Mean	Weighted Mean	Count
Acidity (mg KOH/g)	N/A	0.10	0.00	0.02	0.00	0.00	23
Aromatics (vol%)	N/A	25	10	22	16	17	23
Mercaptan Sulfur (mass%)	N/A	0.003	0.000	0.003	0.001	0.001	17
Total Sulfur (mass%)	N/A	0.30	0.00	0.21	0.05	0.06	23
10 vol% Recovered (°C)	N/A	205	167	196	177	176	21
50 vol% Recovered (°C)	Report		192	218	207	207	20
90 vol% Recovered (°C)	Report		221	263	248	248	21
Final Boiling Point (°C)	N/A	300	249	295	273	273	21
Residue (%)	N/A	1.5	0.8	1.3	1.1	1.2	14
Loss (%)	N/A	1.5	0.0	1.3	0.5	0.5	14
Flash Point (°C)	38	N/A	41	58	47	45	23
Density at 15°C (kg/m^3)	775	840	793	816	805	806	15
Freezing Point (°C)	N/A	-40	-62	-40	-50	-49	23
Viscosity at -20°C (mm^2/s)	N/A	8.0	3.6	6.2	4.8	4.8	22
Net Heat of Combustion (MJ/kg)	42.8	N/A	43.0	43.5	43.2	43.2	23
Smoke Point (mm)	18.0 or 25.0	N/A	18.9	28.1	23.1	23.0	23
Naphthalenes (vol%)	N/A	3.0	0.2	2.0	1.0	1.1	23
Thermal Stability Filter Pressure Drop (mmHg)[1]	N/A	25	0	3	0	0	23
Existent Gum (mg/100 mL)	N/A	7	1	4	2	1	23
Microseparometer Rating Without Electrical Conductivity Additive	85	N/A	99	99	99	99	1
Microseparometer Rating With Electrical Conductivity Additive	70	N/A	94	100	98	98	21
Electrical Conductivity (pS/m)[2]	50	600	0	292	87	24	10

[1] The thermal stability runs ranged from 260-275°C, while the ASTM D1655 specification temperature is 260°C. All runs were done for the specified 2.5 hours.

[2] Electrical conductivity measurements ranged from 19-21°C.

Table 3 shows Jet A-1 CoA data provided by fuel suppliers compared to the specification limits from Defence Standard 91-091 Issue 18 *[5]*. Jet A-1 fuels near/outside the specification limits included:

- Two Jet A-1 fuels had acidity greater than the Defence Standard maximum limit of 0.015 mg KOH/g but within the ASTM D1655 limit of 0.10 mg KOH/g.
- One Jet A-1 fuel had a distillation loss at the maximum limit of 1.5%.
- One Jet A-1 fuel had a flash point at the minimum limit of 38°C.
- Three Jet A-1 fuels had electrical conductivity below the minimum limit of 50 pS/m, a permissible situation prior to addition of static dissipater additive.

Table 3. Statistics for Jet A-1 CoA data compared to specification limits from DEF STAN 91-091.

Property	Specification Limits		Jet A-1 CoA Data				
	Min	Max	Min	Max	Mean	Weighted Mean	Count
Acidity (mg KOH/g)	N/A	0.015	0.000	0.040	0.006	0.003	15
Aromatics (vol%)	N/A	25	14	24	19	19	15
Mercaptan Sulfur (mass%)	N/A	0.003	0.000	0.001	0.001	0.001	14
Total Sulfur (mass%)	N/A	0.30	0.00	0.12	0.05	0.05	15
10 vol% Recovered (°C)	N/A	205	159	177	167	167	15
50 vol% Recovered (°C)	Report		173	212	192	188	15
90 vol% Recovered (°C)	Report		208	266	230	224	15
Final Boiling Point (°C)	N/A	300	229	296	252	245	15
Residue (%)	N/A	1.5	1.1	1.4	1.2	1.2	15
Loss (%)	N/A	1.5	0.0	1.5	0.6	0.5	15
Flash Point (°C)	38	N/A	38	53	41	41	15
Density at 15°C (kg/m^3)	775	840	793	825	805	801	15
Freezing Point (°C)	N/A	-47	-80	-48	-58	-59	15
Viscosity at -20°C (mm^2/s)	N/A	8.0	2.8	5.5	3.6	3.4	15
Net Heat of Combustion (MJ/kg)	42.8	N/A	43.0	43.4	43.2	43.2	15
Smoke Point (mm)	18.0 or 25.0	N/A	19.0	25.0	21.8	22.2	15
Naphthalenes (vol%)	N/A	3.0	0.2	2.4	1.1	1.0	13
Thermal Stability Filter Pressure Drop (mmHg)[3]	N/A	25	0	7	1	1	15
Existent Gum (mg/100 mL)	N/A	7	0	5	2	2	15
Microseparometer Rating Without Electrical Conductivity Additive	85	N/A	92	96	94	94	6
Microseparometer Rating With Electrical Conductivity Additive	70	N/A	90	100	95	97	9
Electrical Conductivity (pS/m)[4]	50	600	0	570	293	277	12

[3] The thermal stability runs ranged from 260-280°C, while the specification temperature is 260°C. All runs were done for the specified 2.5 hours.

[4] Electrical conductivity measurements ranged from 8-28°C.

CoA Histograms

Histograms for the CoA data are shown below. Some observations are:

- Jet A fuels had lower total aromatics than Jet A-1 fuels.
- Jet A fuels had higher values for 10 vol% recovered and final boiling point than Jet A-1 fuels.
- Jet A fuels tended to have lower distillation residue than Jet A-1 fuels.
- Jet A fuels generally had higher flash points than Jet A-1 fuels.
- Jet A fuels generally had higher values for viscosity at -20°C compared to Jet A-1 fuels.
- Jet A fuels generally had higher naphthalenes than Jet A-1 fuels, neglecting two Jet A-1 fuels with 2.4 vol% naphthalenes.
- Jet A-1 fuels generally had lower MSEP values than Jet A fuels.

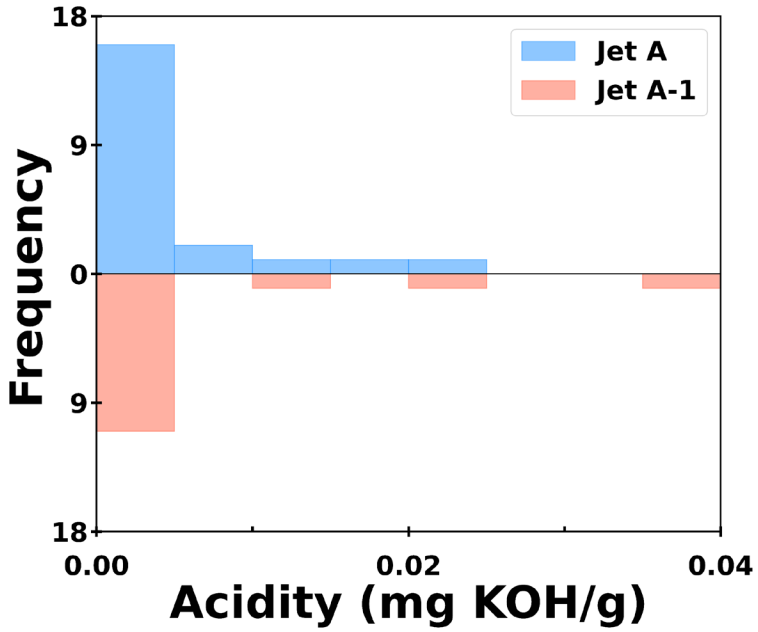

Figure 1. Histogram for acidity, with Jet A fuels on the top and Jet A-1 fuels on the bottom.

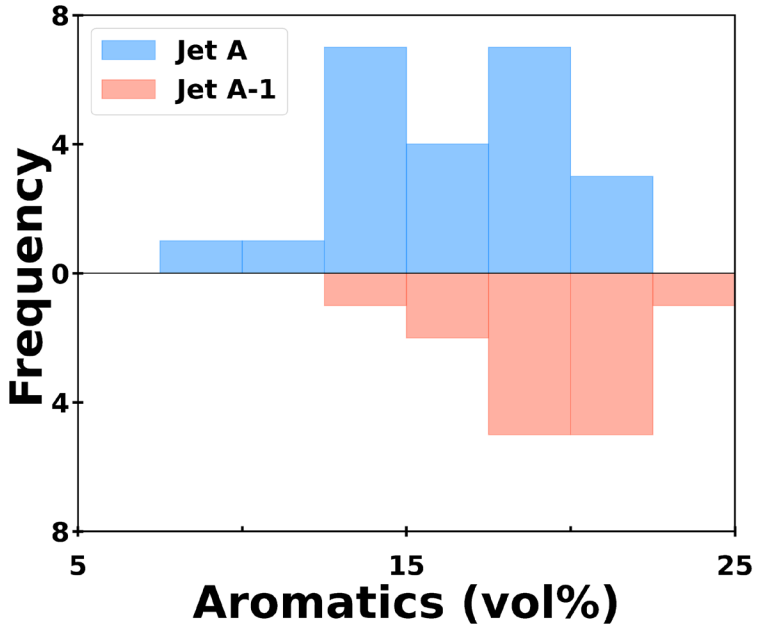

Figure 2. Histogram for aromatics, with Jet A fuels on the top and Jet A-1 fuels on the bottom.

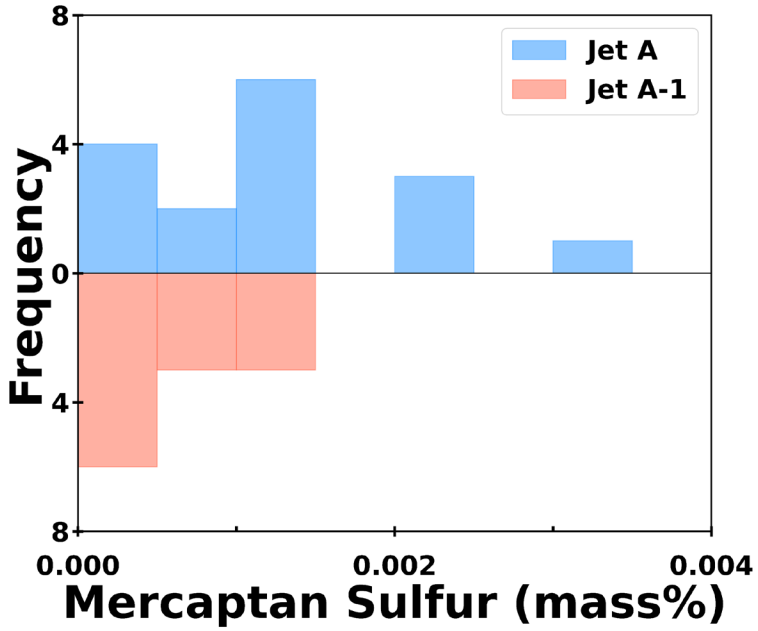

Figure 3. Histogram for mercaptan sulfur, with Jet A fuels on the top and Jet A-1 fuels on the bottom.

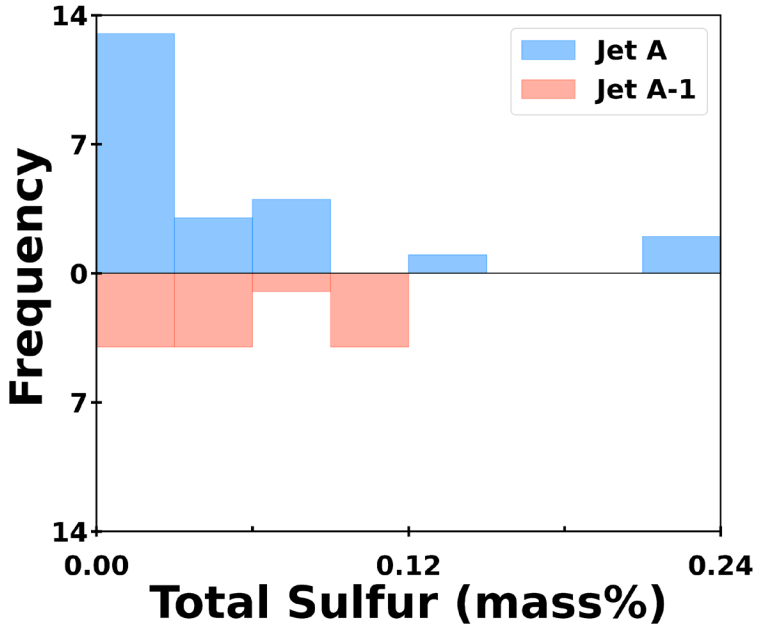

Figure 4. Histogram for total sulfur, with Jet A fuels on the top and Jet A-1 fuels on the bottom.

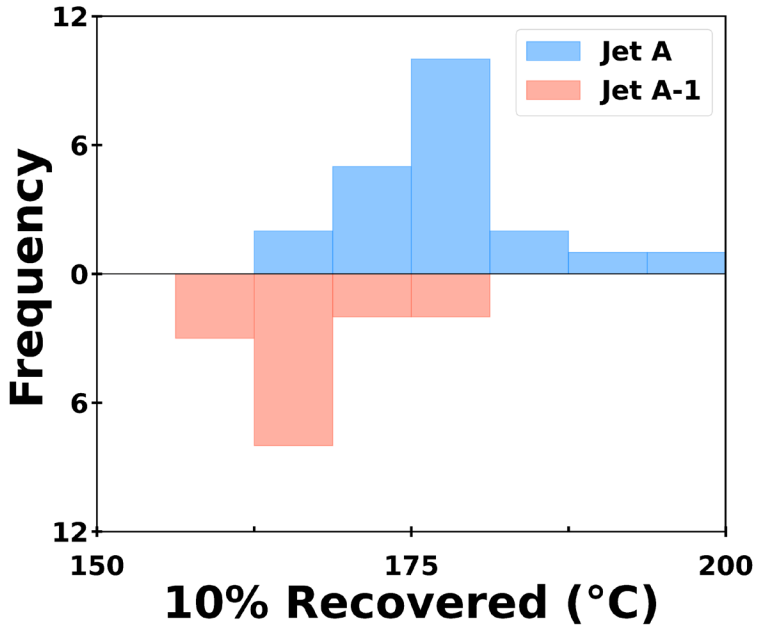

Figure 5. Histogram for 10 vol% recovered, with Jet A fuels on the top and Jet A-1 fuels on the bottom.

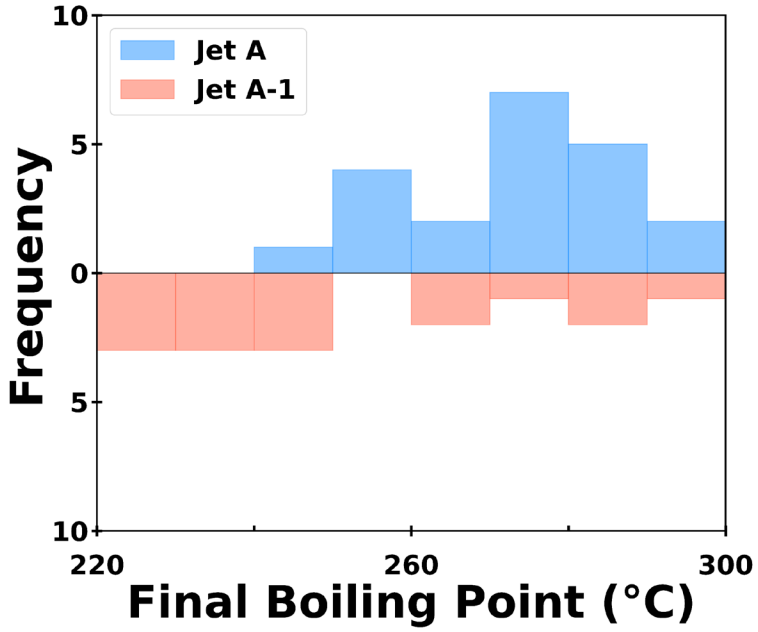

Figure 6. Histogram for final boiling point, with Jet A fuels on the top and Jet A-1 fuels on the bottom.

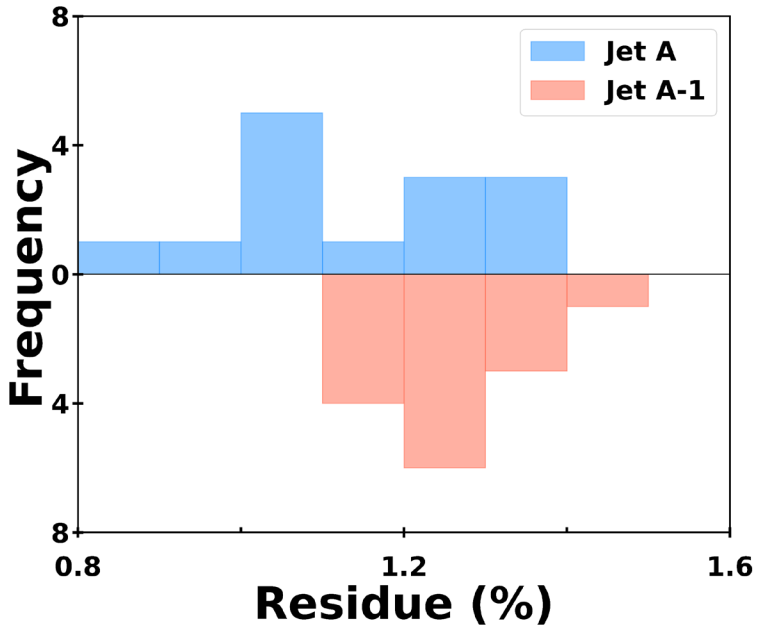

Figure 7. Histogram for distillation residue, with Jet A fuels on the top and Jet A-1 fuels on the bottom.

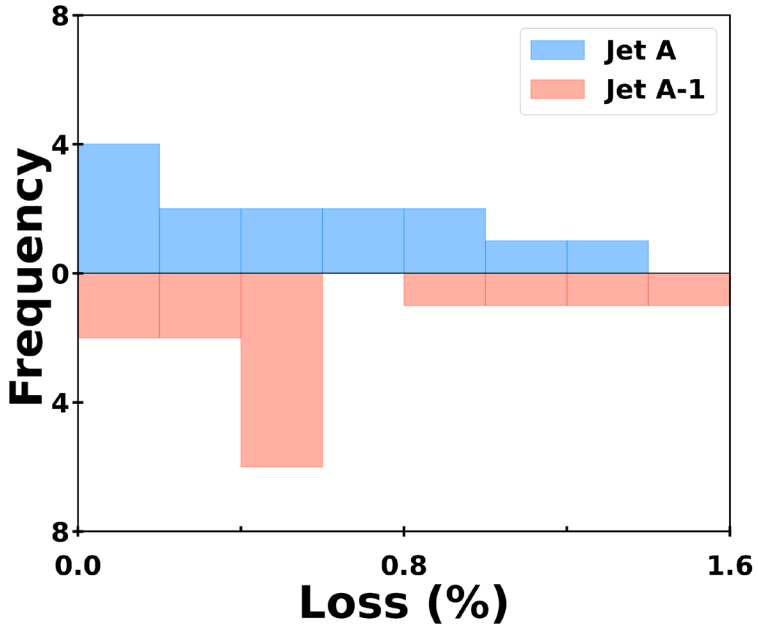

Figure 8. Histogram for distillation loss, with Jet A fuels on the top and Jet A-1 fuels on the bottom.

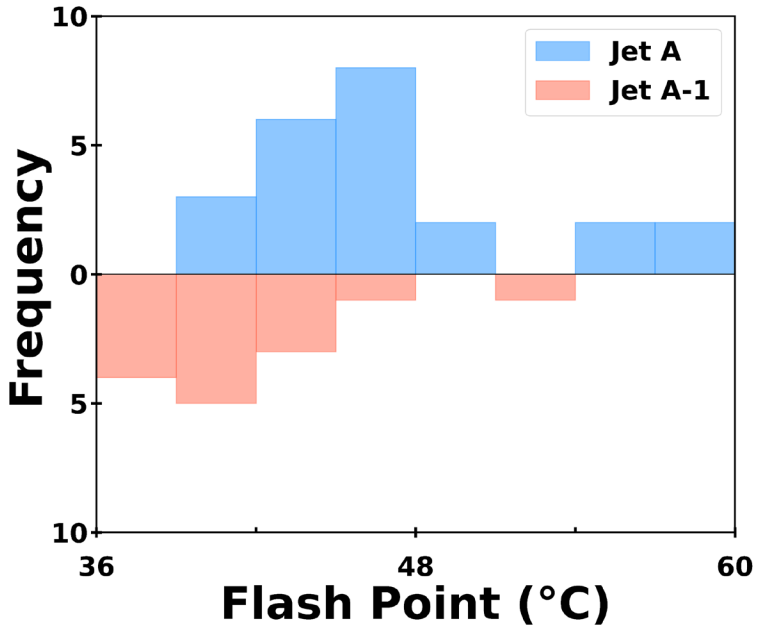

Figure 9. Histogram for flash point, with Jet A fuels on the top and Jet A-1 fuels on the bottom.

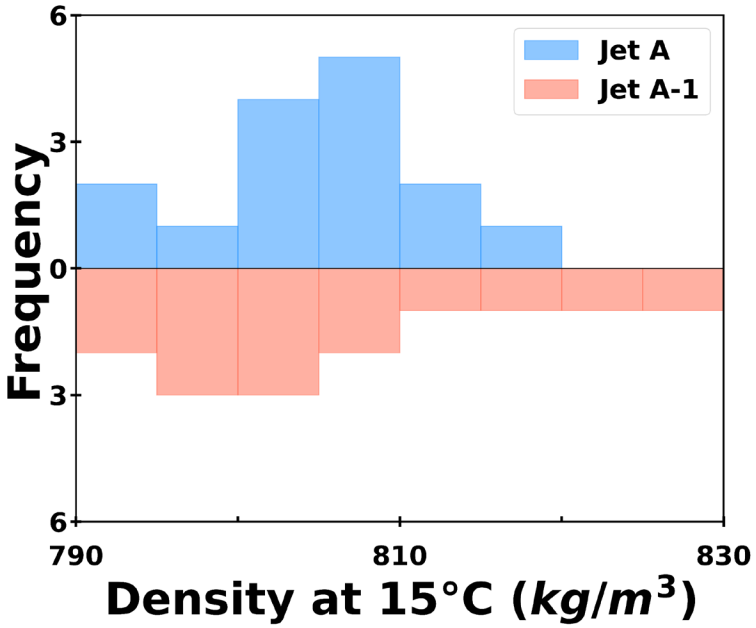

Figure 10. Histogram for density at 15°C, with Jet A fuels on the top and Jet A-1 fuels on the bottom.

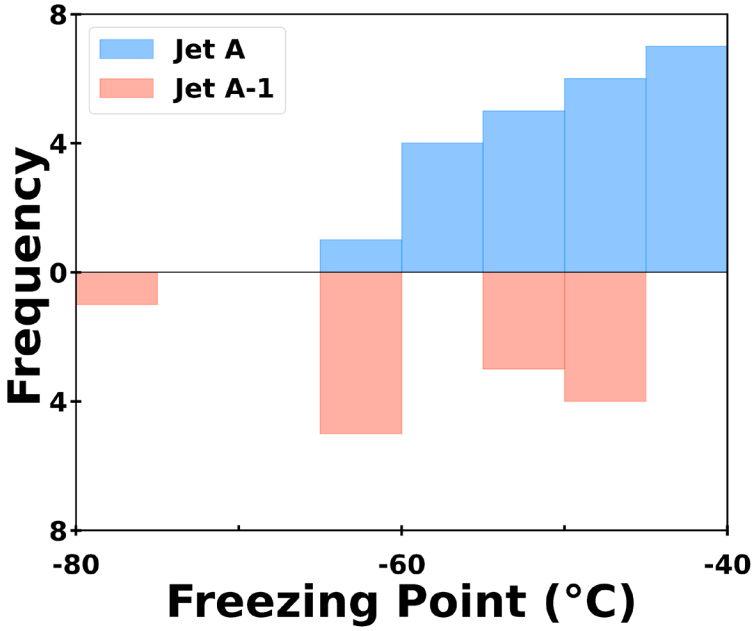

Figure 11. Histogram for freezing point, with Jet A fuels on the top and Jet A-1 fuels on the bottom.

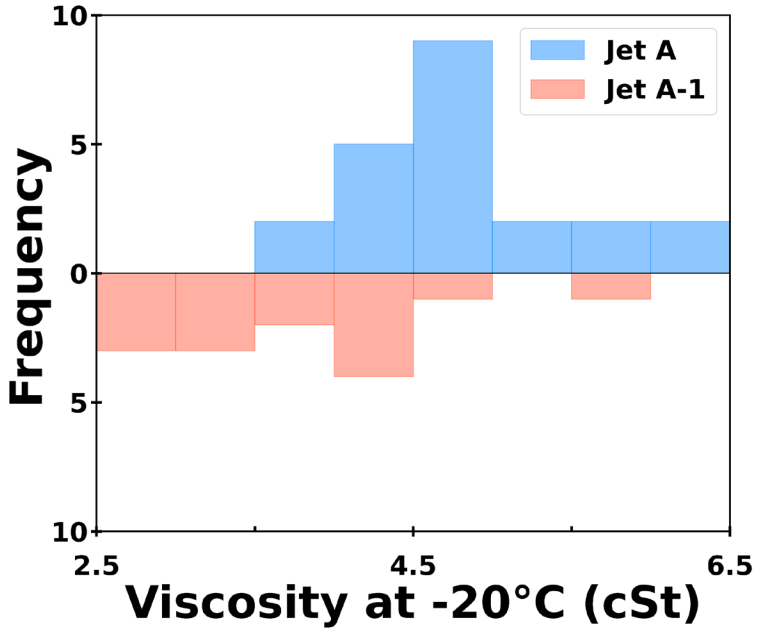

Figure 12. Histogram for viscosity at -20°C, with Jet A fuels on the top and Jet A-1 fuels on the bottom.

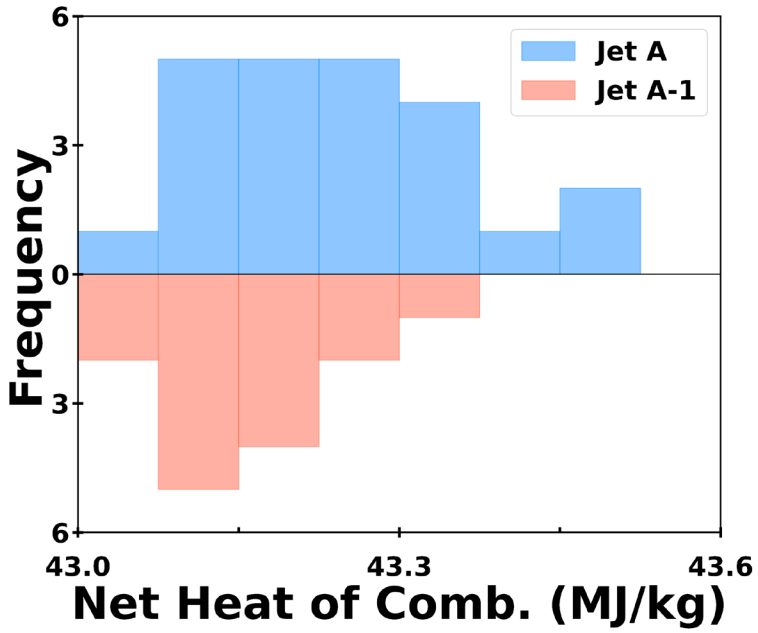

Figure 13. Histogram for net heat of combustion, with Jet A fuels on the top and Jet A-1 fuels on the bottom.

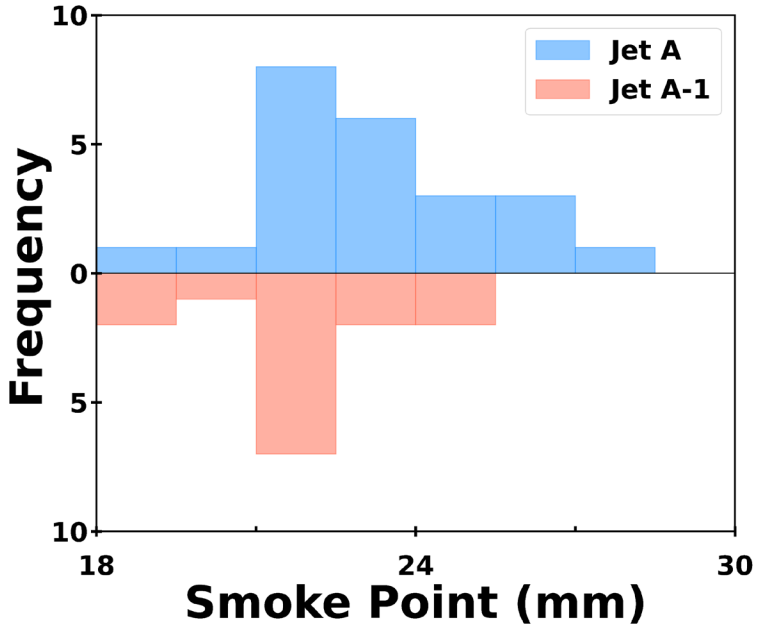

Figure 14. Histogram for smoke point, with Jet A fuels on the top and Jet A-1 fuels on the bottom.

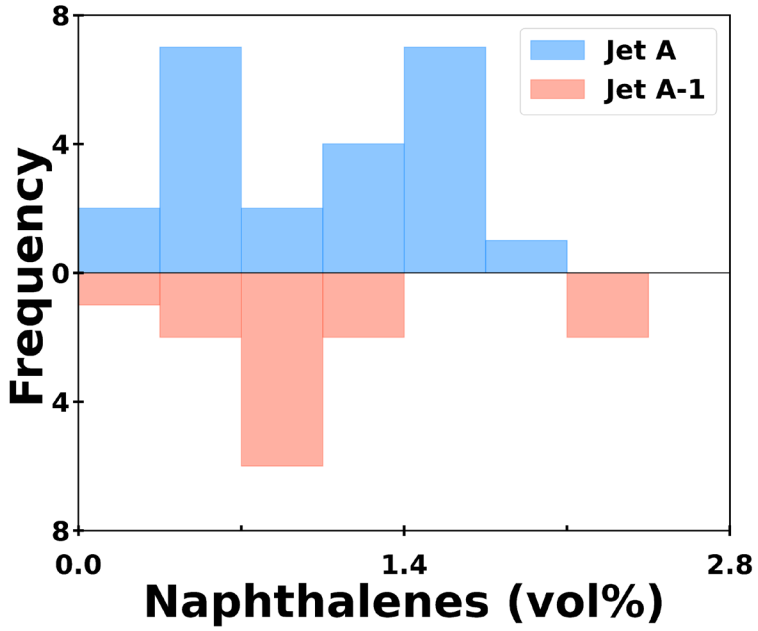

Figure 15. Histogram for naphthalenes, with Jet A fuels on the top and Jet A-1 fuels on the bottom.

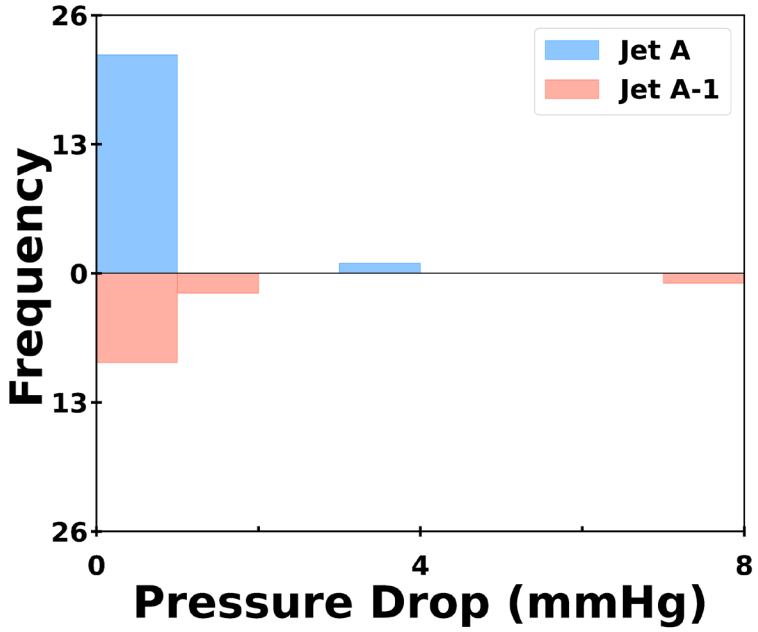

Figure 16. Histogram for thermal stability filter pressure drop, with Jet A fuels on the top and Jet A-1 fuels on the bottom. Thermal stability was run for 2.5 hours and ranged from 260-280°C.

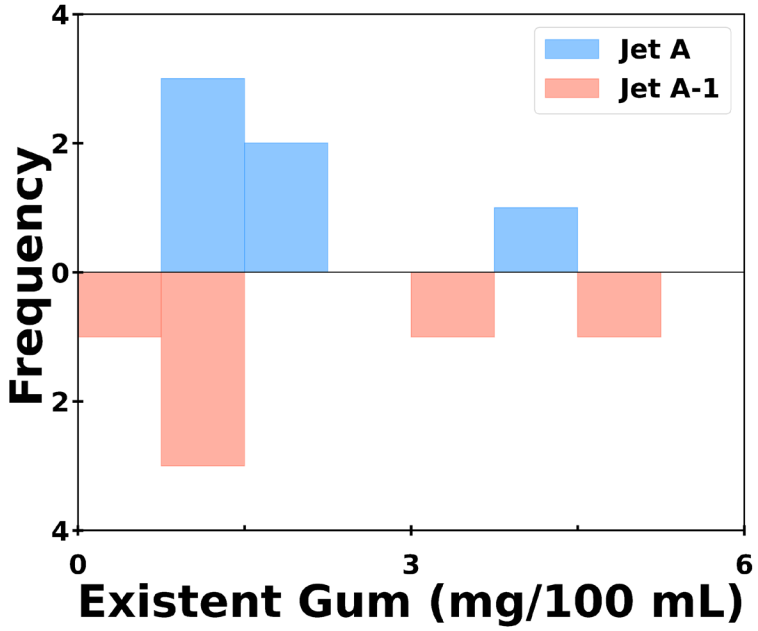

Figure 17. Histogram for existent gum, with Jet A fuels on the top and Jet A-1 fuels on the bottom.

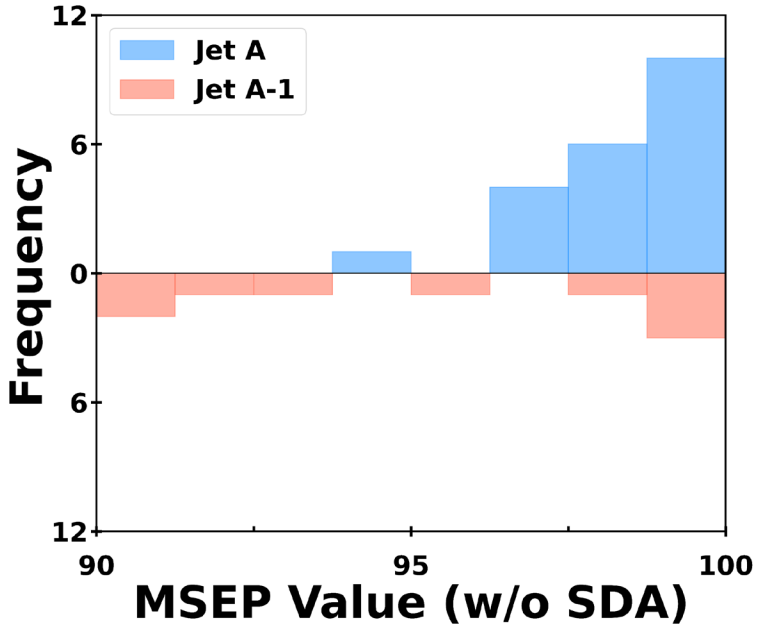

Figure 18. Histogram for microseparometer rating without electrical conductivity additive, with Jet A fuels on the top and Jet A-1 fuels on the bottom.

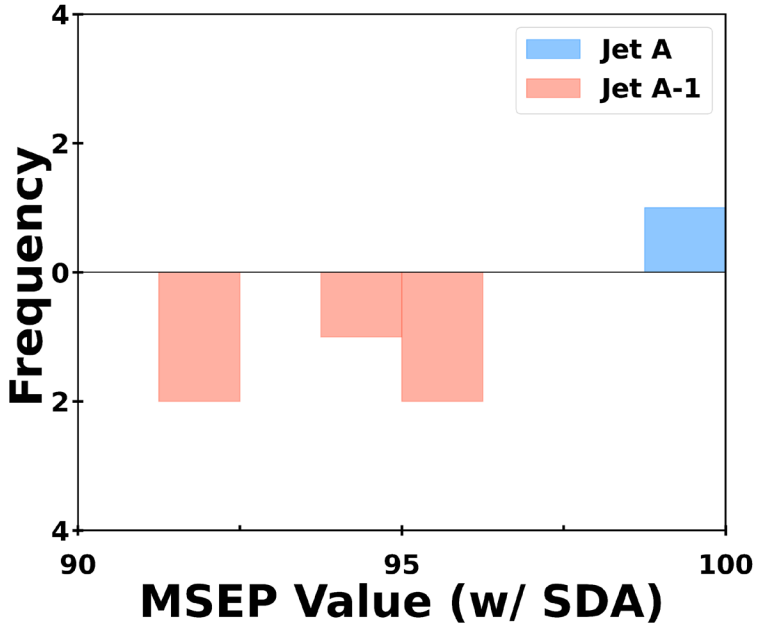

Figure 19. Histogram for microseparometer rating with electrical conductivity additive, with Jet A fuels on the top and Jet A-1 fuels on the bottom.

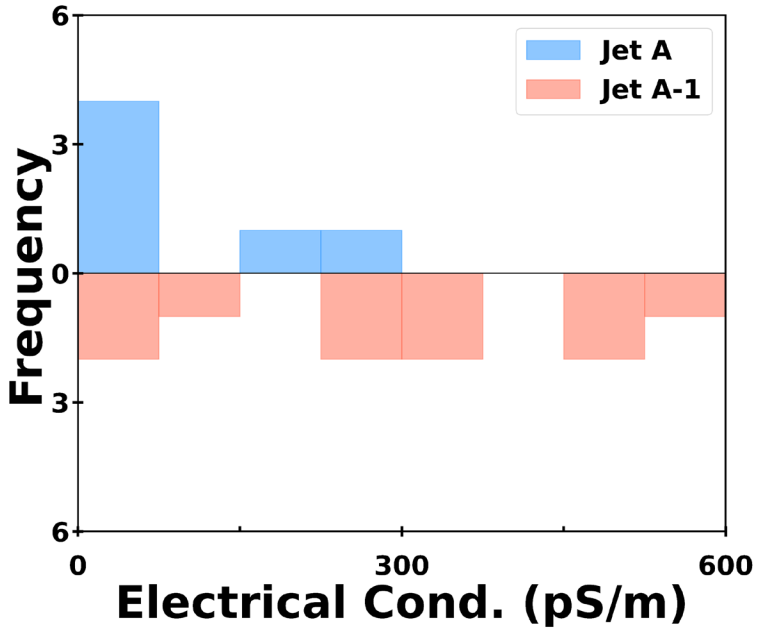

Figure 20. Histogram for electrical conductivity, with Jet A fuels on the top and Jet A-1 fuels on the bottom. Electrical conductivity measurements ranged from 8-28°C.

3. Fit-for-purpose Data

Chemistry (Composition)

Hydrocarbon-Type

Detailed hydrocarbon-type analysis (HTA) was performed using two-dimensional gas chromatography (GCxGC) in a normal phase separation space following UDRI FC-M-101: "Flow Modulation GCxGC for Hydrocarbon-Type Analysis of Conventional and Alternative Aviation Fuels" [7] and FED-STD-791F Test Method 7508.0: "Method for Detailed Hydrocarbon Analysis of Middle Distillate Fuels by Two-Dimensional Gas Chromatography" [8]. All HTA data reported herein were obtained in accordance with the precision and accuracy practices of FED-STD-791F. The specified gravimetric hydrocarbon reference standard was analyzed and satisfied the accuracy criteria within ±0.2 mass% concentrations of each standard compound. This step ensures proper function and comprehensiveness of the instrument. Repeatability of replicate runs was consistent with the method requirements of ±0.04 mass% for Tier 3 groups of a reference fuel (POSF 10325). The demonstrated reproducibility of FED-STD-791F at the Tier 3 level ranges from 0.02 to 0.70 mass%. More details about the experimental method can be found in the Appendix.

Multiple hydrocarbon-type classifications are used in this report and referred to as tiers. Tier 1 classifies hydrocarbons into two broad groups: saturates and aromatics. Tier 2 HTA further refines this classification by grouping hydrocarbons into their respective classes (e.g., monocycloalkanes, alkylbenzenes, etc.). Tier 3 subdivides these Tier 2 groups according to carbon number. Tier 4 provides molecule-specific identifications, such as the cumene analysis in the Appendix of this report.

Figure *21* shows a violin plot for Tier 1.5 HTA groups. Tier 1.5 has fidelity between Tier 1 and Tier 2, with *n*- and *iso*-alkanes grouped together, monocycloalkanes, dicycloalkanes and tricycloalkanes grouped as cycloalkanes, and alkylbenzenes and cycloaromatics grouped as alkylbenzenes. The median and IQR values from this report shown in Table *4*, are reported in mass%. The solid horizontal lines in Figure *21* represent median values, and the dashed horizontal lines signify the 25^{th} and 75^{th} percentiles of the data. The left violins represent a subset of data from CRC Report 647, downselected to only include Jet A, Jet A-1, and JP-8 fuels (56 fuels in total) [9], and the right violins represent data from this report. Compared to CRC Report 647, *n*- and *iso*-alkanes were displaced by cycloalkanes in the set of fuels analyzed in this report. Both CRC Report 647 and this report had a high number of outliers with high cycloalkane concentrations. The alkylbenzene and diaromatic profiles of the two reports mirrored each other, with CRC Report 647 having slightly higher median values for both compared to this report.

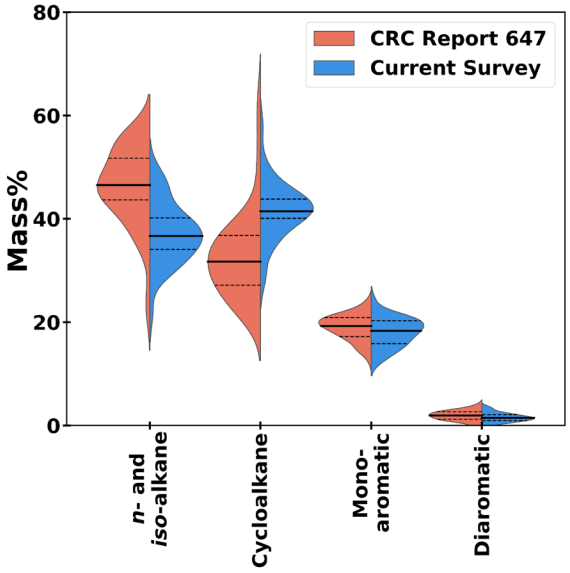

Figure 21. Violin plot for Tier 1.5 hydrocarbon-type groups.

Table 4. Median and IQR for the Tier 1.5 GCxGC hydrocarbon-type data from this report.

Group	25th Percentile (mass%)	Median (mass%)	75th Percentile (mass%)
n- and *iso*-alkanes	34.20	36.73	40.18
Cycloalkane	41.05	42.51	45.39
Alkylbenzene	15.84	18.32	20.27
Diaromatic	1.26	1.56	2.20

Figure *22* shows a violin plot for Tier 2 HTA groups. The groups are ordered from lowest double bond equivalent (DBE) on the left to highest DBE on the right. The median mass% values from this report followed the order: monocycloalkane > *iso*-alkane > *n*-alkane > dicycloalkane ≈ alkylbenzene > cycloaromatic > diaromatic. *n*-alkanes, *iso*-alkanes, and alkylbenzenes had the largest IQRs, and therefore the greatest variation, while tricycloalkanes and diaromatics had the smallest IQRs. Monocycloalkanes and dicycloalkanes are reported at a higher mass% here than CRC Report 647, and they also have a narrower distribution. *n*-alkanes, *iso*-alkanes, and alkylbenzenes are reported at a lower mass% here than CRC Report 647. Cycloaromatic and diaromatic mass% concentrations are consistent between CRC Report 647 and this report.

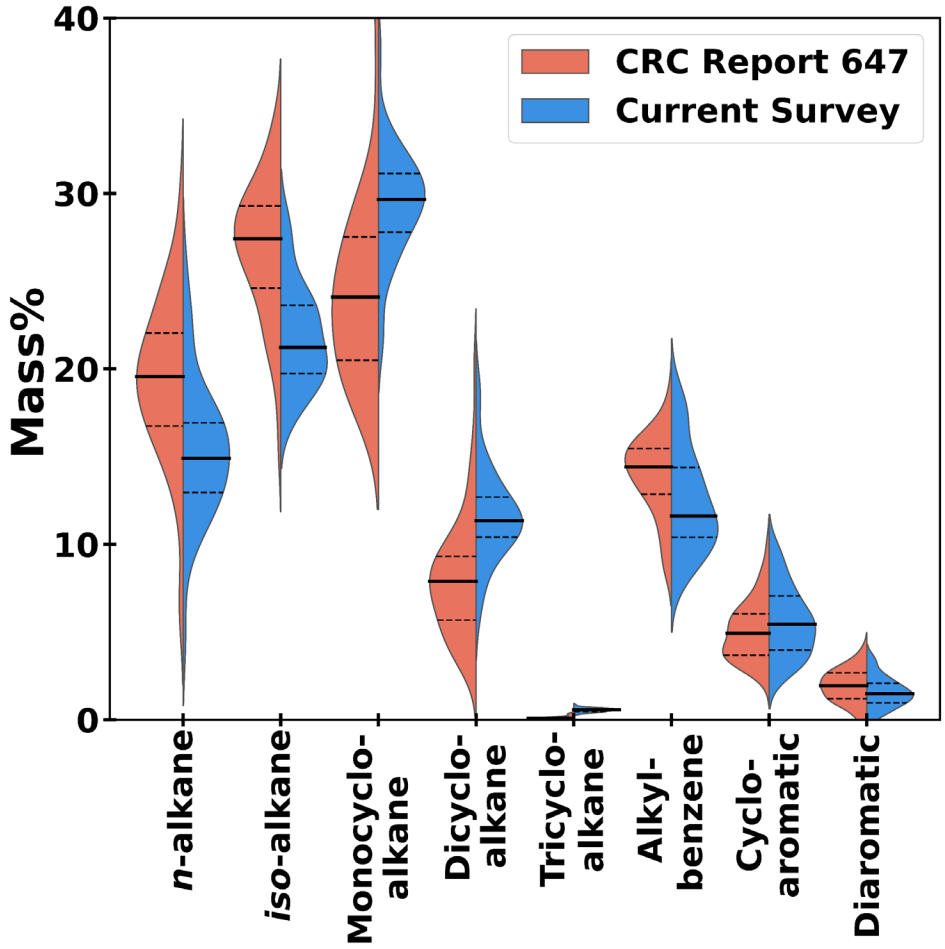

Figure 22. Violin plot for Tier 2 hydrocarbon-type groups, with groups ordered from lowest to highest DBE.

Table 5. Median and IQR for the Tier 2 GCxGC hydrocarbon-type data from this report.

Group	25th Percentile (mass%)	Median (mass%)	75th Percentile (mass%)
n-alkane	13.01	14.92	16.93
iso-alkane	19.75	21.26	23.61
Monocycloalkane	27.98	29.80	31.28
Dicycloalkane	10.54	11.45	12.83
Tricycloalkane	1.02	1.50	1.84
Alkylbenzene	10.40	11.62	14.39
Cycloaromatic	3.97	5.45	7.06
Diaromatic	1.26	1.56	2.20

Aromatics

Aromatics, saturates, and olefins were measured using ASTM D1319-20a: "Standard Test Method for Hydrocarbon Types in Liquid Petroleum Products by Fluorescent Indicator Adsorption" [10]. Custom instrumentation was used (i.e., tube glassware, UV lighting, measuring calipers, etc.). This ASTM method has repeatability values of 1.3 vol%, 1.5 vol%, and $0.26X^{0.6}$ vol% for aromatics, saturates, and olefins, respectively. X is defined as the average of two results in volume percent. Using the median olefin content of 1.0 vol%, the calculated repeatability was 0.3 vol%. Median values for aromatics and saturates measured/calculated using ASTM D1319 and GCxGC hydrocarbon-type analysis are shown in Table *6*. Volume percent reporting for GCxGC requires assuming densities for each hydrocarbon-type region to convert the data from mass%. D1319 had a higher value for aromatics and a lower value for saturates compared to the GCxGC results. The third column shows the mean absolute difference (MAD) between the D1319 and GCxGC data calculated using all the fuels. The MAD values were 0.6 vol% and 1.2 vol%, respectively, for aromatics and saturates. This indicates that D1319 agrees more closely with the GCxGC data for aromatics than saturates for the 38 fuels in the current survey.

Table 6. Median aromatic and saturate values for ASTM D1319 and GCxGC hydrocarbon-type.

Group	D1319 Median (vol%)	GCxGC Median (vol%)	Mean Absolute Difference (vol%)
Aromatic	19.1	18.22	0.6
Saturate	80.1	81.78	1.2

Figure *23* shows a histogram of olefin vol% according to D1319. While olefins are not currently specified in ASTM D1655, they are generally deemed to have poor gum stability which reportedly limits the concentration to about 1% or less [4]. 13 of the 38 fuels in this report exceeded 1 vol% as reported by D1319, with a median value of 1.0 vol%. The median value from CRC Report 647 is 0.5 vol% higher than the fuels analyzed in this report. The p-value from a t-test was 2.7×10^{-10}, indicating that the olefin content decline since 2006 is statistically significant (i.e., $p < 0.05$) between the two sample populations. It is unclear if this statistically significant decline is due to change in olefin content, difference in measurement technique (i.e., change in ASTM D1319 dye reagent), or representative sample populations. ASTM D1319 Table X1.1: "Summary of Precision Analyses" lists a bias of $L = P + 0.4$ vol% for jet fuel, where L and P are the olefin content measured using the pre-2019 legacy dye and post-2019 prototype dye, respectively [10]. This bias was based on an abbreviated analysis where there was inadequate variation of olefin content among samples. The 0.4 vol% bias is not far from the 0.5

vol% upshift of CRC Report 647 compared to the current survey. A potential area for future work is comparison of the ASTM D1319 olefin measurements with vacuum ultraviolet (VUV) detector methods such as 1D GC-VUV [11], GCxGC-VUV [12], or with supercritical fluid chromatography [13].

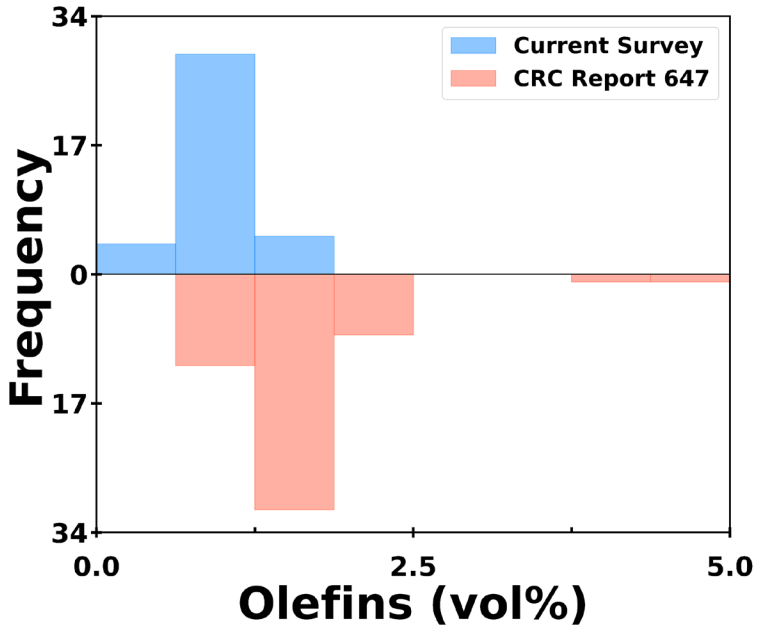

Figure 23. Histogram for D1319 olefin content, with the current survey on the top and CRC Report 647 on the bottom.

Hydrogen

Hydrogen content was measured using ASTM D3701-17: “Standard Test Method for Hydrogen Content of Aviation Turbine Fuels by Low Resolution Nuclear Magnetic Resonance Spectrometry” [14]. The repeatability for this method is 0.09 mass%. The instrumentation used was a Newport Instruments model NA3/WR3. As shown in Figure *24*, the data are normally distributed, with a median value of 13.9 mass%. This is 0.3 mass% lower than the CRC Report 647 median value. See the Appendix for a comparison of the NMR results with the results calculated from the hydrocarbon-type data.

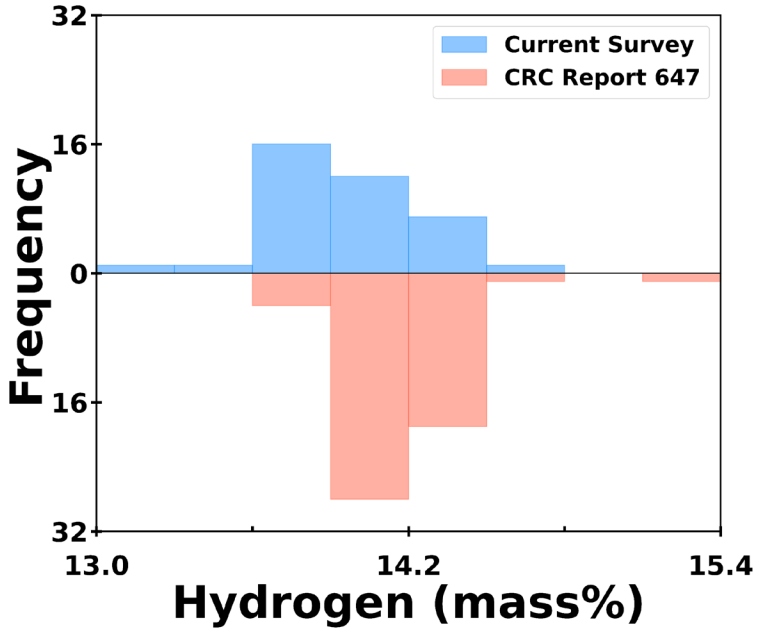

Figure 24. Histogram for hydrogen content, with the current survey on the top and CRC Report 647 on the bottom.

Polars

Polars were measured using UDRI FC-M-102: “Identification and Quantification of Polar Species in Conventional and Alternative Aviation Fuel Using SPE-GCxGC” [15]. In short, solid phase extraction was used to remove and concentrate polar species from the bulk fuel (hydrocarbon matrix) and eluted into methanol. This was followed by GCxGC identification and quantitation of the captured analytes. The precision of this method arises from a combination of several factors. The extraction efficiency of compounds varies among the groups reported. Competitive sorption and steric hinderance is likely the cause of these variations. In a preliminary study (unpublished), extraction efficiencies were >80% for 83 of the 107 analytes investigated. Despite this, the variability in the extraction efficiency remains an inherent error embedded into the overall precision of this method. A comparative study between two labs (unpublished data) gave a reproducibility of 6% RSD for total polar concentration. Individual polar species groups exhibited higher degrees of uncertainty, between ~7-43% RSD for the typical species classes reported.

In Figure *25*, alcohols through phthalates are oxygen-containing polars (blue), and alkylamines through tetrahydroquinolines (THQs) are nitrogen-containing polars (red). The compound classes that can be identified and quantified with this method is an active area of research for UDRI that is evolving with the jet fuel industry. The “Other” group represents the sum of compounds that are chromatographically isolated and detectable but have not yet been

identified by mass spectrometry. Expected carbon number ranges for the polars groups can be found in the Supplementary Data file. Phenols and other polars are plotted separately in Figure *26* because they have significantly higher concentrations. Phenols had some significant high outlier values. Tier 3 polars groups broken out by carbon number remain as future work but could provide useful information for modeling efforts.

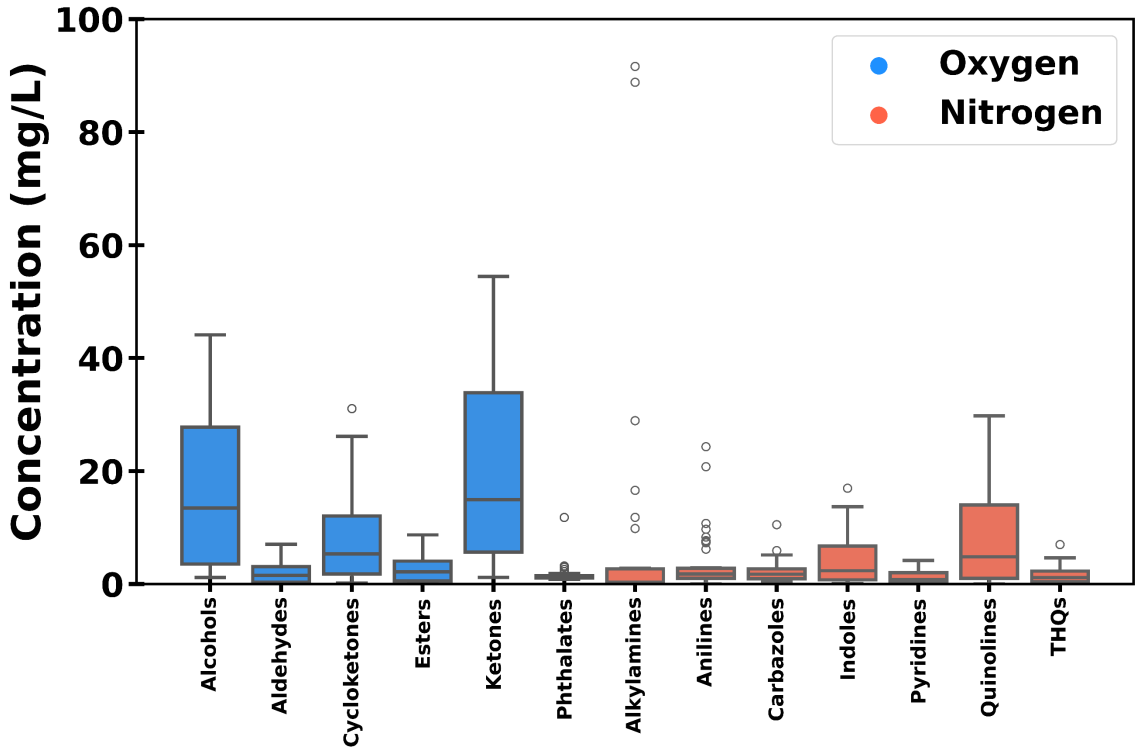

Figure 25. Box plot for trace polars groups with phenols and other polars removed.

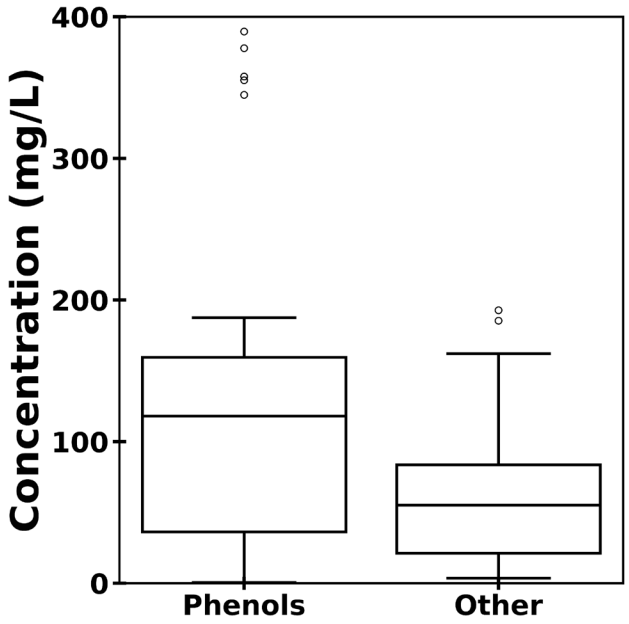

Figure 26. Box plot for phenols and other polars.

Table *7* shows median values and IQR ranges for the polars data in this report. The data were divided into four groups for high-level analysis: nitrogen-containing species, oxygen-containing species, other, and total. The order of summed median values was as follows: nitrogen < other < oxygen. The appreciable concentration of the other group (i.e., compounds that were not identified by the existing polars template) indicates that future work is still needed to expand the polars template.

Table 7. Median and IQR for the polars data in this report.

Group	25th Percentile (mg/L)	Median (mg/L)	75th Percentile (mg/L)
Oxygen	58	187	225
Nitrogen	8	15	37
Other	21	55	84
Total	101	258	345

Inorganics: N

Nitrogen content was measured following ASTM D4629-17: “Standard Test Method for Trace Nitrogen in Liquid Hydrocarbons by Syringe/Inlet Oxidative Combustion and Chemiluminescence Detection” [16]. The method repeatability is $0.1825X^{0.5149}$ mg/kg. Using the median nitrogen content of 1.7 mg/kg, the calculated repeatability was 0.2 mg/kg. The

instrumentation used was an Antek Multitek HNS. The results are shown in Figure *27*. The median value was 1.7 mg/kg.

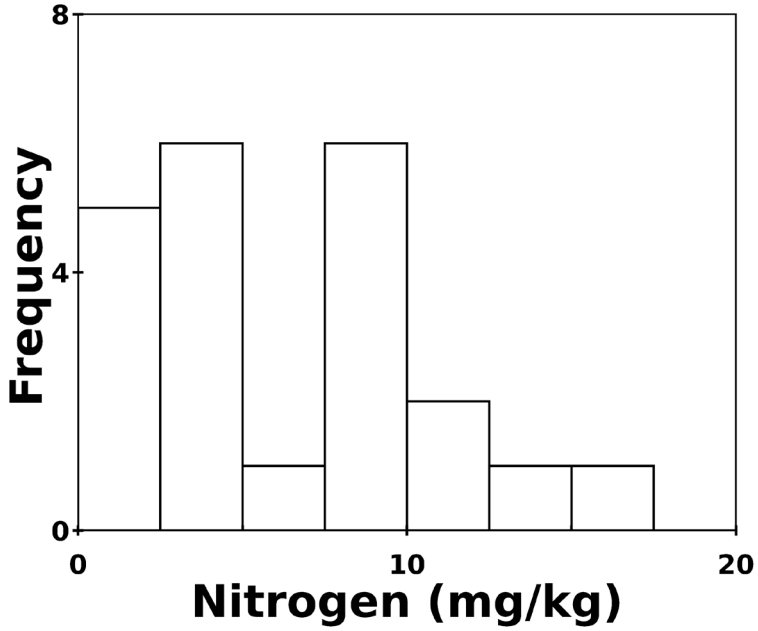

Figure 27. Histogram for nitrogen content in the current survey.

Trace Elements

Trace elements were analyzed following UDRI FC-M-107: “UDRI FC-M-107: Trace Elemental Determination in Jet Fuel via ICP-MS” [17]. Specifically, a Thermo Fisher Scientific inductively coupled plasma (ICP)-MS was used with an iCAP brand reaction cell single quadrupole spectrometer. Results are reported to either one or two significant figures depending on the element and its corresponding reporting limit. Figure *28* and Figure *29* show box plots for trace elements. Phosphorous, silicon, and titanium were broken out in Figure *29* because they had significantly higher concentrations than other trace elements. Silver (Ag), boron (B), barium (Ba), and cadmium (Cd) are monitored here but are not included in ASTM D4054. The following elements had no measurements above their reporting limit: Ba, Ca, Co, Cr, Cu, K, Li, Mg, Mn, Mo, Na, Ni, Pb, Pd, Sn, Sr, V, and Zn. Median trace elements values for calcium (Ca), copper (Cu), iron (Fe), magnesium (Mg), and zinc (Zn) from CRC Report 647, which were also measured using ICP analysis, are represented by the orange horizontal lines. Median values in this report are close to median values from CRC Report 647, with calcium, magnesium, and zinc equal, copper 2 ppb wt lower in this report, and iron 1 ppb higher in this report.

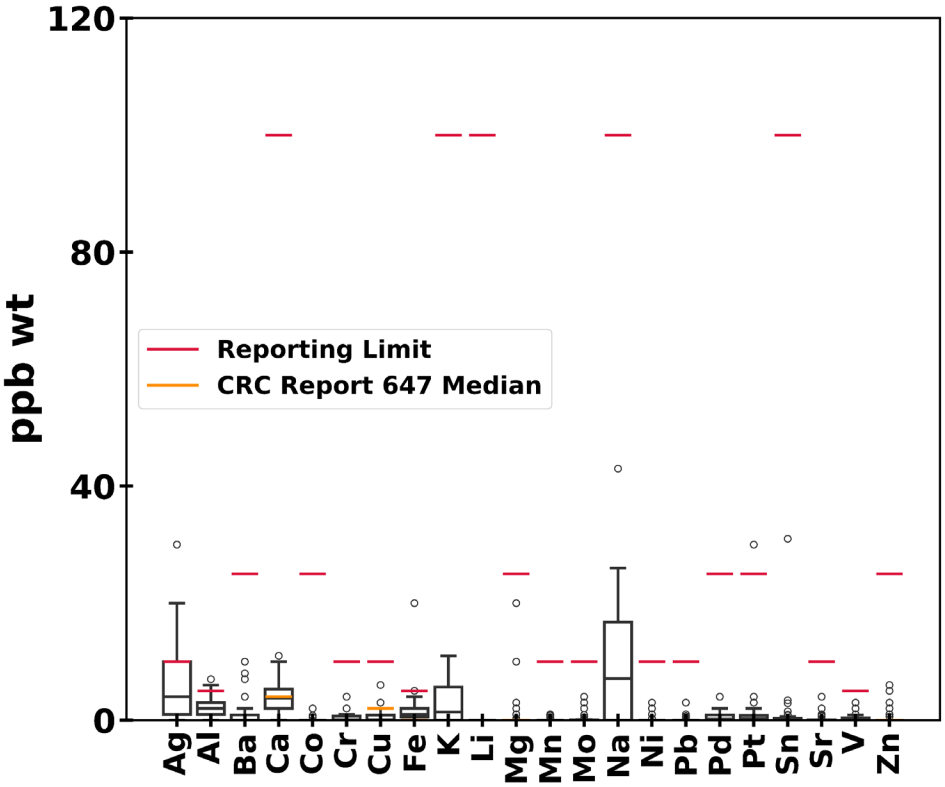

Figure 28. Box plot for trace elements with P, Si, and Ti omitted. Red lines represent the reporting limit, and orange lines represent median values from CRC Report 647.

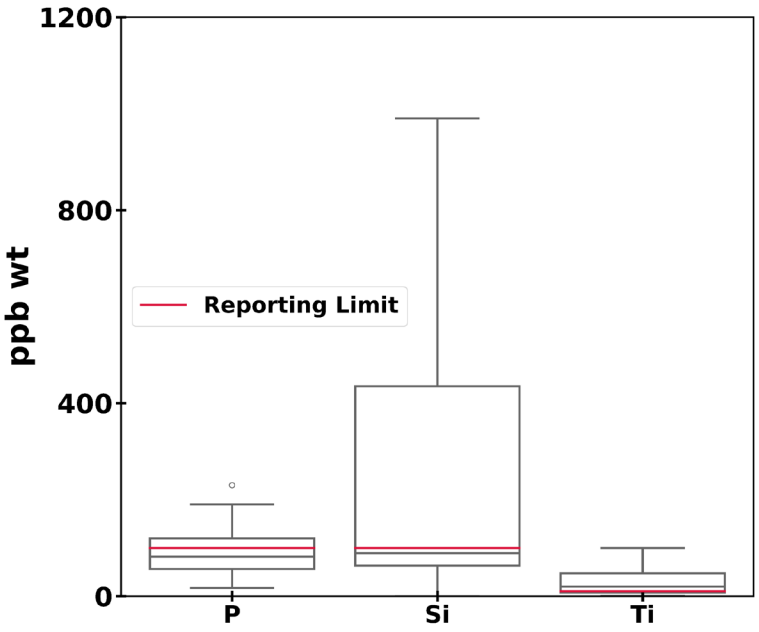

Figure 29. Box plot for trace elements for P, Si, and Ti. Red lines represent the lower reporting limits.

Table *8* shows median and IQR values for phosphorous, silicon, and magnesium. Phosphorous and silicon had similar median values, but silicon had a much higher 75th percentile. Titanium is the only element with a median value above its reporting limit. Titanium has known polyatomic interferents which may result in overreporting.

Table 8. Median and IQR values for phosphorous, silicon, and titanium.

Element	**Reporting Limit (ppb wt)**	**25th Percentile (ppb wt)**	**Median (ppb wt)**	**75th Percentile (ppb wt)**
Phosphorous (P)	100	56	82	120
Silicon (Si)	100	63	89	440
Titanium (Ti)	10	8	20	50

Bulk Physical and Performance Properties

Distillation

Experimental distillation was measured using ASTM D86-23: “Standard Test Method for Distillation of Petroleum Products and Liquid Fuels at Atmospheric Pressure” [18]. The instrumentation used was a PAC OptiDist operated using the automated method. According to ASTM D86 Table 1, the fuels in this report can either be considered Group 2 (final boiling point ≤ 250°C) or Group 4 (initial boiling point >100°C and final boiling point > 250°C). Depending on the group, either Table 7 or Table 10 is used to calculate the precision. Of the 38 fuels in this report, 10 were in Group 2 and 28 were in Group 4. The mean calculated repeatability values for the current survey were as follows: 2.7°C (initial boiling point), 2.5°C (5% recovered), 2.0°C (10% recovered), 1.5°C (20% recovered), 1.3°C (30% recovered), 1.3°C (40% recovered), 1.3°C (50% recovered), 0.9°C (60% recovered), 1.0°C (70% recovered), 1.1°C (80% recovered), 1.3°C (90% recovered), 1.9°C (95% recovered), 3.0°C (final boiling point). Initial and final boiling point had the largest repeatability values, and the middle of the distillation curve had the lowest repeatability values.

Figure *30* shows a box plot of distillation temperature versus vol% recovered. There was a 21°C jump in median temperature between initial boiling point (IBP) and 5 vol% recovered, which is well above the 2.7°C mean repeatability for initial boiling point. A similar jump was also observed for the simulated distillation (SimDis) results in the next section. The jump may be caused by light species such as *n*-hexane, C6 *iso*-alkanes, and C5-C6 cyclohexanes, which all had median concentrations ≥0.01 mass% as measured by GCxGC. Neat C5-C9 *n*-alkanes, for instance, have a logarithmic correlation between carbon number and boiling point [19]. This trend could

suppress the initial boiling point relative to 5 vol% recovered. The IQR increased with temperature, indicating greater variance at elevated temperatures. The red lines represent the 10 vol% recovered and final boiling point limits from ASTM D1655. None of the fuels were above the specification limits. Median values from CRC Report 647 are plotted as orange lines. The CRC data falls within the IQR from this report, although the median from this report is higher from 50 vol% recovered and above.

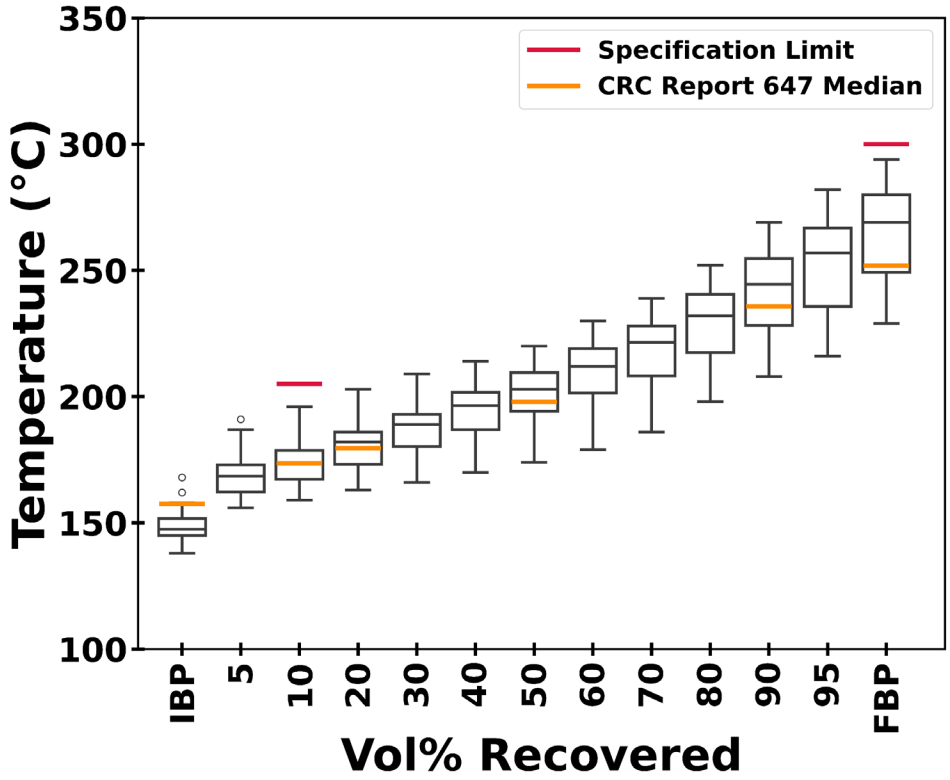

Figure 30. Box plot for D86 distillation. The red lines represent the upper specification limit from ASTM D1655. The orange lines represent the median values from CRC Report 647.

Figure *31* is a violin plot of the D86 distillation data. The initial boiling point is lower in the current survey compared to CRC Report 647 but reaches higher median temperatures from 20 vol% recovered onward. The model coefficients for the initial boiling point partial least squares (PLS) model (see Appendix Figure 57) provide a possible explanation for the downward shift relative to CRC Report 647. Model coefficients for light species (i.e., C8 *n*-alkanes, C8 *iso*-alkanes, and especially C7-C8 monocycloalkanes) indicate a strong negative correlation with the initial boiling point. According to the Tier 3 GCxGC data, the fuels in this survey have a higher concentration of C7-C8 monocycloalkanes. If the modeling coefficients are correct, this would decrease the initial boiling point relative to CRC Report 647.

The model coefficients for the final boiling point PLS model (see Appendix Figure *58*) provide a possible explanation for the upward shift relative to CRC Report 647. Heavy (i.e., roughly ≥ CN 14) *iso*-alkane, monocycloalkane, and dicycloalkane model coefficients had a strong positive effect on final boiling point. According to the Tier 3 GCxGC data (Figure *75*), the fuels in this survey had roughly the same amount of ≥C14 *iso*-alkanes as CRC Report 647. However, the fuels in this survey had a significantly higher concentration of ≥C14 monocycloalkanes and dicycloalkanes compared to CRC Report 647. If the model coefficients are correct, the high concentration of heavy monocycloalkane and dicycloalkanes would increase the final boiling point relative to CRC Report 647. There was also a higher concentration of C14-C15 cycloaromatics in this survey compared to CRC Report 647, which would further increase the final boiling point. Future work is training distillation models using the CRC Report 647 data for a more robust comparison.

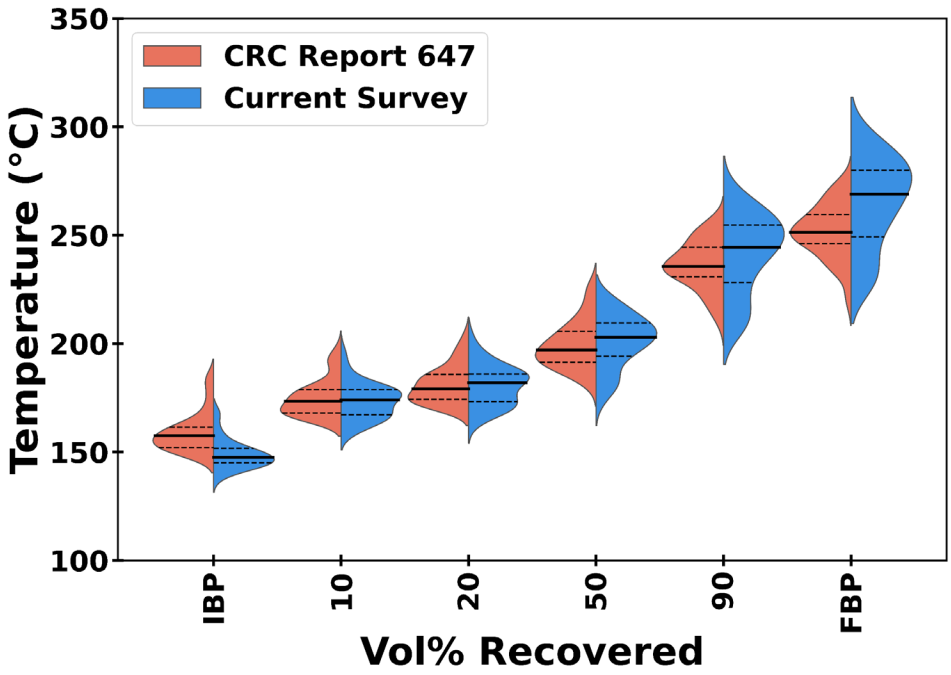

Figure 31. Violin plot for D86 distillation.

Table *9* contains statistics for distillation residue, loss, and slope. Median values for residue and loss were 1.2% and 0.4%. The current survey has a median residue value 0.2% lower than CRC Report 647. None of the residue and loss values exceeded the 1.5% limit from ASTM D1655. Median values for T_{50} - T_{10} and T_{90} - T_{10} were 29°C and 71°C, respectively. The current survey has median T_{50} - T_{10} and T_{90} - T_{10} values 5°C and 9°C higher, respectively, than CRC Report 647. Two of the fuels tested had T_{50} - T_{10} values below the 15°C limit from ASTM D7566-22a: “Standard Specification for Aviation Turbine Fuel Containing Synthesized Hydrocarbons” [20]. None of the fuels had T_{90} - T_{10} values below the ASTM D7566 limit of 40°C.

Table 9. Median and IQR values for distillation residue, loss, and slopes.

Distillation Metric	Median (Current Survey)	Median (CRC Report 647)
Residue (%)	1.2	1.4
Loss (%)	0.4	N/A
T_{50} - T_{10}	29	24
T_{90} - T_{10}	71	62

Simulated Distillation

Simulated distillation was measured following ASTM D2887-23: “Standard Test Method for Boiling Range Distribution of Petroleum Fractions by Gas Chromatography” [21]. The instrumentation used was an Agilent 7890 GC with a Restek Rtx-5 column (30m, 0.32 mmID, 0.25 µm, catalog #10224). SimDis Expert software version 10 (Separation Systems, Inc.) was used for the data analysis. The repeatability is as follows: 0.011X°C (initial boiling point), 0.0032(X + 100)°C (5 vol% recovered), 0.8°C (10-20 vol% recovered), 0.8°C (30 vol% recovered), 0.8°C (40 vol% recovered), 1.0°C (50-90 vol% recovered), 1.2°C (95 vol% recovered), and 3.2°C (final boiling point). Using median temperatures of 105°C and 145°C for initial boiling point and 5% recovered, the calculated repeatability values were 1.2°C and 0.8°C, respectively. Like D86 distillation, initial and final boiling point had the highest repeatability values. Figure *32* shows a violin plot of SimDis temperature versus vol% recovered. The IQR increased with temperature, indicating greater variation at higher temperatures. The CRC data fall within the IQR from this report, although the median values from this report are higher from 20 vol% recovered and above. The CRC Report 647 results had high-temperature tailing at IBP, and the results from this report had low-temperature tailing from about 50 vol% recovered and higher.

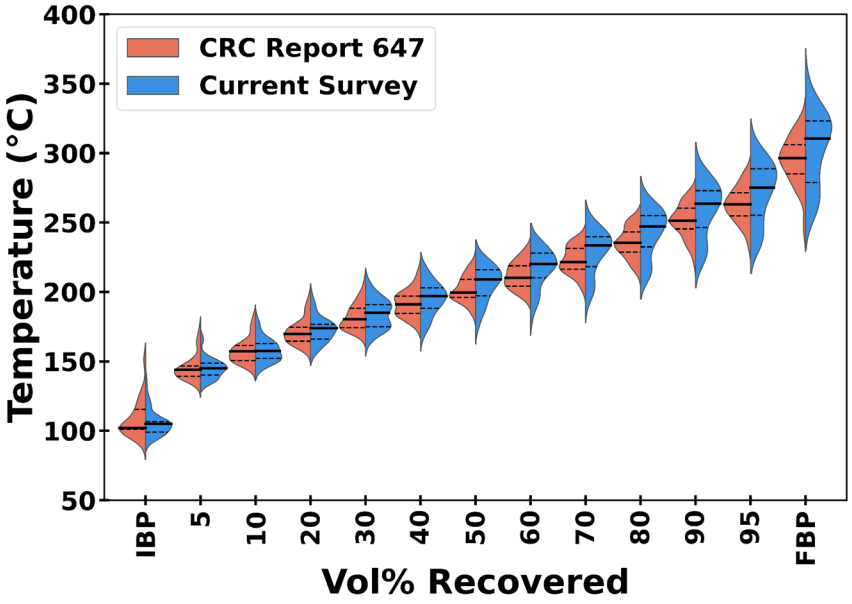

Figure 32. Violin plot for simulated distillation measurements.

SimDis data were converted to ASTM D86 equivalents following the procedure described in ASTM D2887 Section X4: "Correlation for Jet and Diesel Fuel (Procedures A and B)." Figure *33* is a violin plot of the SimDis D86 correlation data. Both CRC Report 647 and the current survey had high-temperature outliers at the IBP. The temperature range of the current survey is larger than CRC Report 647 from 50 vol% and higher. The current survey had non-normal temperature distributions starting at 30 vol% recovered and higher.

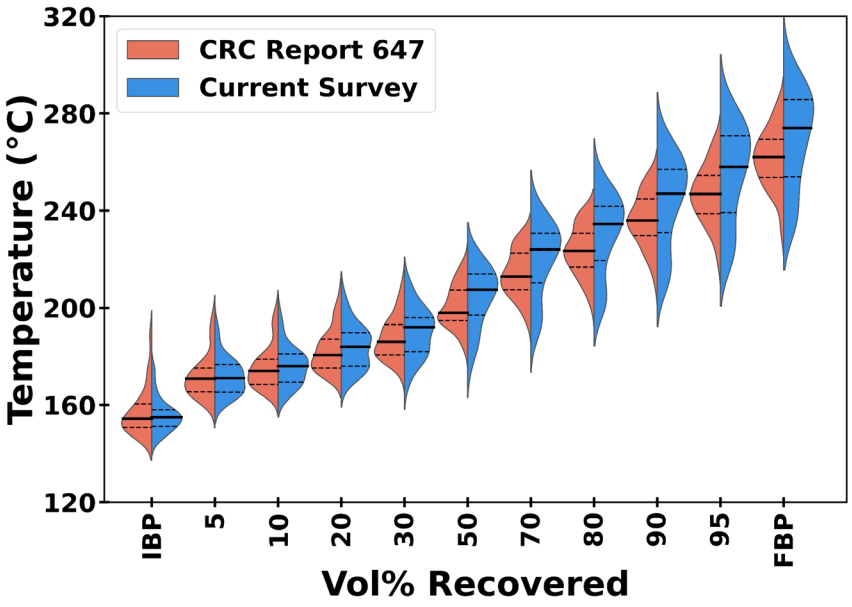

Figure 33. Violin plot for simulated distillation D86 correlation following ASTM D2887 Section X4.

Median values for D86 distillation and SimDis D86 correlation are shown in *Table 10*. The fourth column shows the mean absolute error (MAE) between the D86 and D86 correlation values calculated using all the fuels. The initial and final boiling points had the highest MAE values at 7°C and 5°C, respectively. Median D86 correlation values were always greater than median D86 values. All the MAE values were below the cross-method reproducibility values from ASTM D2887.

Table 10. Median D86 distillation and SimDis D86 correlation values following ASTM D2887 Section X4.

Percent Recovered (vol%)	D86 Median (°C)	D86 Correlation Median (°C)	Mean Absolute Error (°C)	Cross-Method Reproducibility (°C)
IBP	147	155	7	14
5	168	171	3	12
10	174	176	3	11
20	182	184	3	9
30	189	192	3	7
50	203	208	4	7
70	221	224	2	7
80	232	235	2	8
90	244	247	3	9
95	257	258	3	17
FBP	269	274	5	13

Thermal Stability

ASTM D3241 Breakpoint

Breakpoint was measured using ASTM D3241-23a: “Standard Test Method for Thermal Oxidation Stability of Aviation Turbine Fuels” using a protocol developed by researchers at SwRI (see the Appendix) [22]. The instrumentation used was a Falex model 400-1757 and a Falex 430 ellipsometeric tube rater (ETR). The reported repeatability for this method is 0.00981(x + 73.12) nm. Using the median deposit thickness of 46 nm, the calculated repeatability was 1 nm. Figure *34* shows a histogram of the breakpoint results. The median breakpoint highest passing temperature was 295°C, with the data being slightly skewed above the median. This median value is 10°C higher than the CRC Report 647 median.

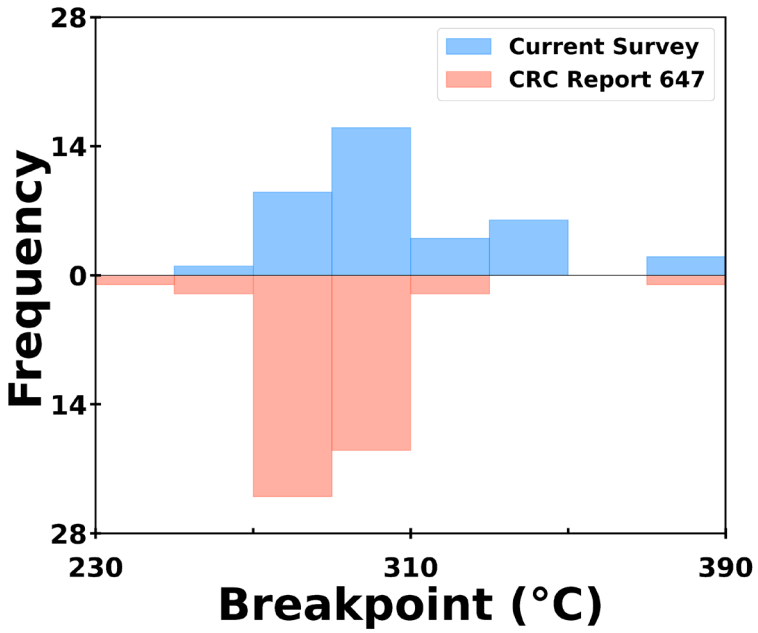

Figure 34. Histogram for breakpoint values, with the current survey on the top and CRC Report 647 on the bottom.

Pressure drop and ETR for the breakpoint highest passing temperature results are shown in Figure *35*. The red lines represent the upper limits of 25 mmHg and 85 nm for the pressure drop and ETR, respectively, from ASTM D1655. The median values for the pressure drop and ETR are 0 mmHg and 46 nm, respectively. These median values are well below the limits. This deviation from the limits is not unexpected due to the exponential nature of jet fuel autoxidation [23], which can cause exponential increases in ETR with temperature [24]. 25 fuels with 0 mmHg pressure drop readings were dropped before plotting to allow for logarithmic y-axis scaling.

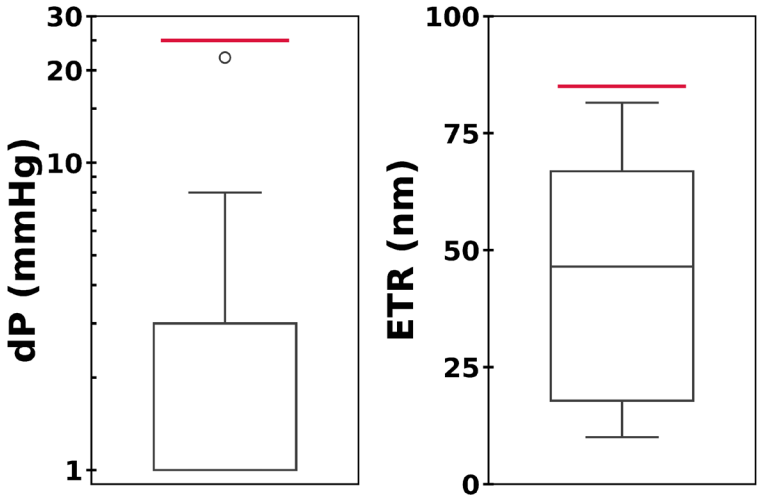

Figure 35. Pressure drop and ellipsometer readings for the breakpoint data. The red lines represent the limits from ASTM D1655.

ASTM D7739 Deposition

Quartz crystal microbalance (QCM) deposition was measured following ASTM D7739-11: "Standard Practice for Thermal Oxidative Stability Measurement via Quartz Crystal Microbalance" [25]. A 100 mL stainless steel reactor and a quartz crystal fitted with gold electrodes were used, as described in the ASTM method. Test conditions involved air saturated fuel stressed at 140°C over a 15-hour duration. See the Appendix for an explanation of the deposition calculations. An abbreviated repeatability study was done with two fuels, which had deposition values of 0.9 and 20.4 µg/cm^2. Repeatability was calculated as 2.8 times the standard deviation, as defined in ASTM E177-20: "Standard Practice for Use of the Terms Precision and Bias in ASTM Test Methods" [26]. Repeatability values for these fuels were 0.8 and 3.6 µg/cm^2, respectively, after three replicates. This corresponds to 87% and 18% of the mean measured deposition values, indicating that the repeatability error becomes more significant for lower deposition values. Figure *36* shows QCM deposition, which was run for approximately 15h at 140°C. The range of QCM deposition was large, spanning from 0.2-26.7 µg/cm^2. The median QCM deposition was 2.5 µg/cm^2, with a significant amount of tailing at higher deposition values. Of the 13 fuels with antioxidant concentration reported in the CoA, 10 had a concentration of 0.0 mg/L. The median QCM deposition for the fuels with a reported antioxidant concentration of zero was 1.2 µg/cm^2. Fuels #25, #3, and #19 had antioxidant concentrations of 15.0, 18.2, and 21.0 mg/L, respectively. Fuels #25, #3, and #19 had QCM deposition values of 8.1, 3.1, and 0.5 µg/cm^2, respectively. More fuels with non-zero antioxidant concentrations (i.e., ≥ 5-10 fuels)

would be required to determine whether there is a statistically significant inverse correlation with QCM deposition.

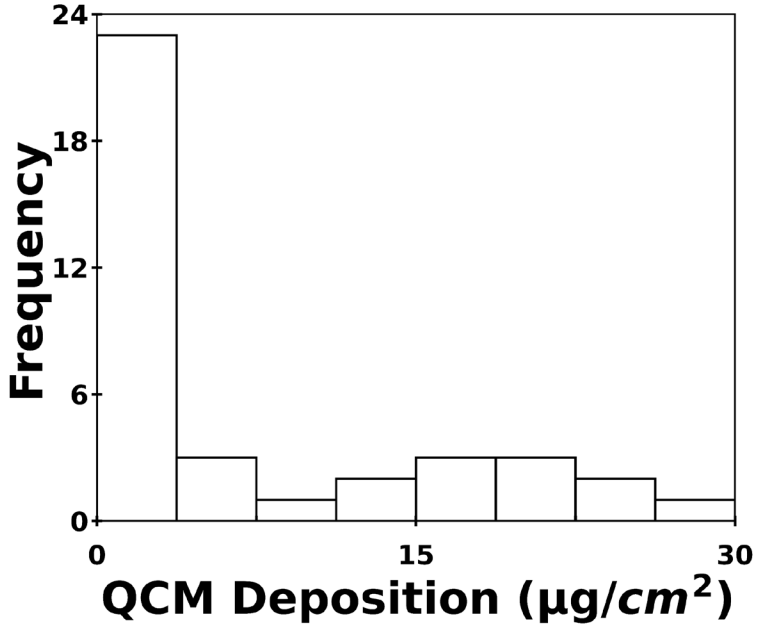

Figure 36. Histogram of QCM deposition for fuels from the current survey run for approximately 15 hours at 140°C.

Lubricity

Lubricity was measured following ASTM D5001-19e1: “Standard Test Method for Measurement of Lubricity of Aviation Turbine Fuels by the Ball-on-Cylinder Lubricity Evaluator (BOCLE)” [27]. The instrumentation used was a PCS Instruments ABS Auto BOCLE run using the fully automatic method. The repeatability is $0.08580X^{2.5083}$ mm. Using the median wear scar diameter (WSD) of 0.67 mm from the current survey, the calculated repeatability was 0.03 mm. Figure 37 shows stacked histograms of WSD for the current survey and CRC Report 647. The median of 0.67 mm from the current survey is 0.05 mm higher than the CRC Report 647 median of 0.62 mm. The maximum WSD from the current survey was 0.83 mm, which is below the recommended limit of 0.85 mm required for coprocessing.

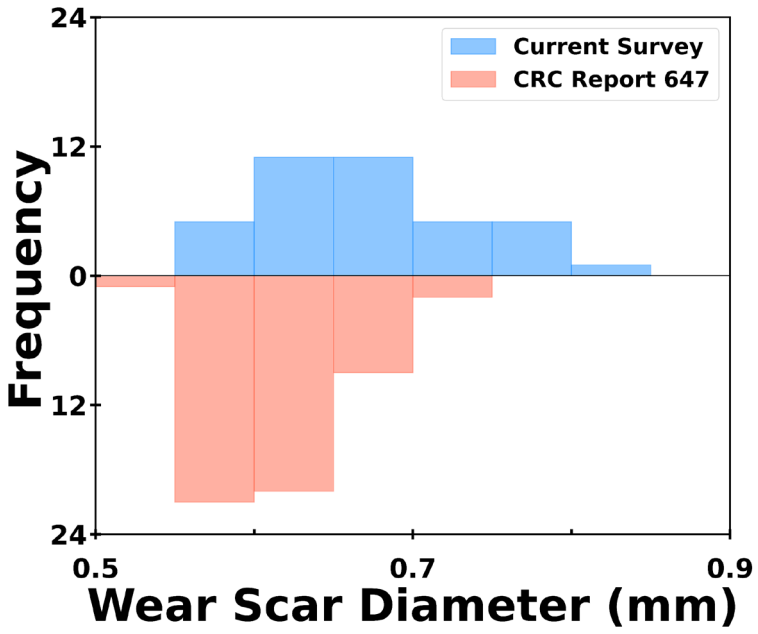

Figure 37. Histogram for WSD values, with the current survey on the top and CRC Report 647 on the bottom.

Viscosity versus Temperature

Kinematic viscosity was measured as a function of temperature following ASTM D7042-21a: “Standard Test Method for Dynamic Viscosity and Density of Liquids by Stabinger Viscometer (and the Calculation of Kinematic Viscosity)” [28]. The instrumentation used was an Anton Paar SVM 3001. The repeatability is 0.007074X cSt at -20°C and 0.005261X cSt at -40°C. Using the median viscosity values of 4.33 cSt at -20°C and 8.74 at -40°C, calculated repeatability values were 0.03 cSt and 0.05 cSt, respectively. Figure *38* shows a box plot of the measured viscosity values from -40 to 100°C. The red line represents the -20°C viscosity specification limit of 8 mm^2/s from ASTM D1655. The viscosity was below the -20°C specification limit. The trend with temperature was as expected, with median viscosity values increasing exponentially at low temperatures. The IQR increased at lower temperatures, indicating greater variance. Median values from CRC Report 647, plotted as orange lines, are lower than the median values from this report at -40°C and -20°C. Viscosity was measured via ASTM D455 in CRC Report 647.

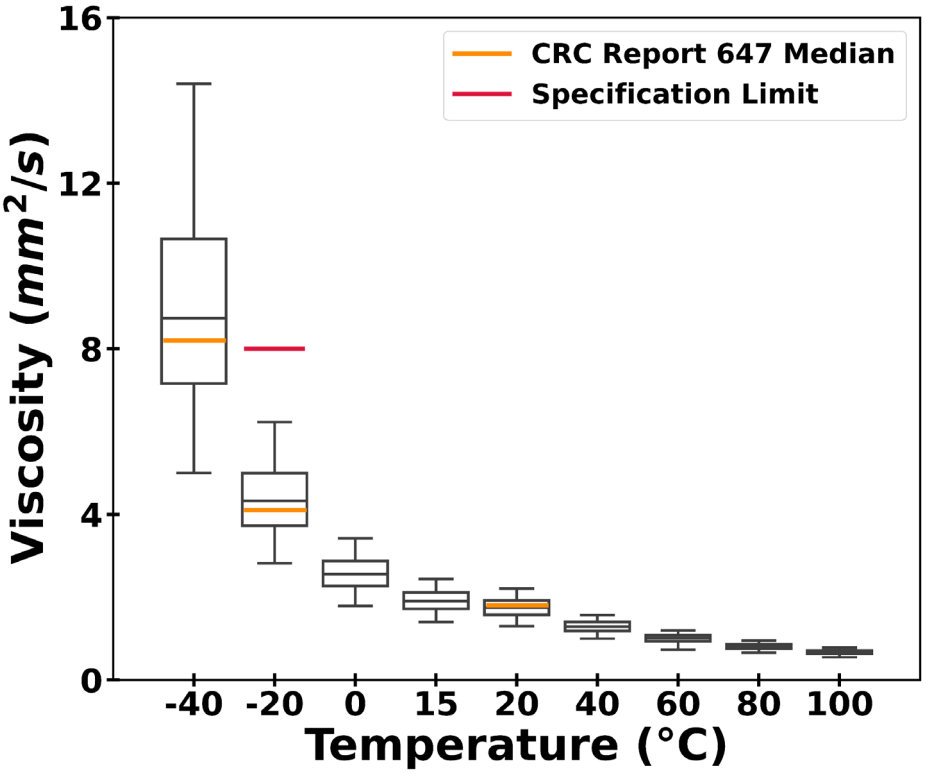

Figure 38. Box plots for viscosity at the measured temperatures. The red lines represent the -20°C upper specification limit from ASTM D1655. The orange lines represent median values from CRC Report 647.

Figure 39 is a violin plot of viscosity at the temperatures measured in CRC Report 647. The distributions from this report are similar to those in CRC Report 647.

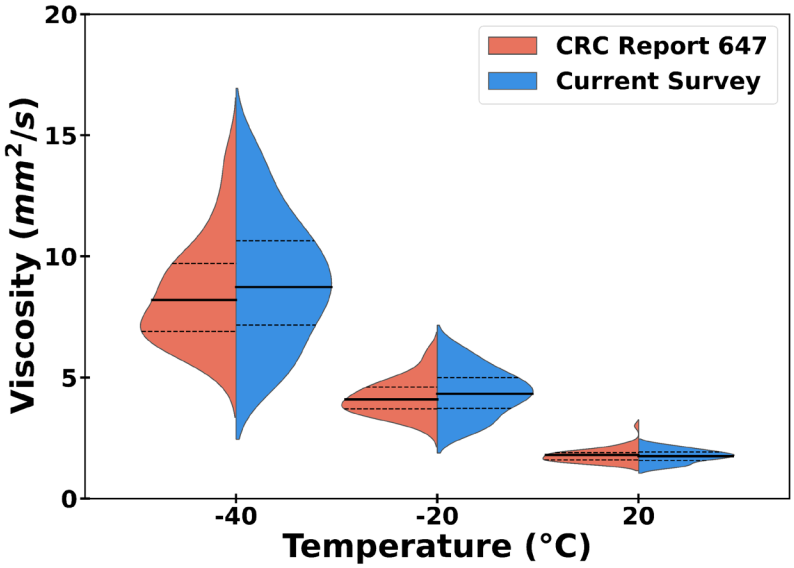

Figure 39. Violin plot for viscosity at the measured temperatures.

Specific Heat versus Temperature

Specific heat capacity was measured following ASTM E2716-09: “Standard Test Method for Determining Specific Heat Capacity by Sinusoidal Modulated Temperature Differential Scanning Calorimetry” [29]. The reported repeatability for this method is 1.1%. Figure *40* shows a box plot for specific heat capacity measured from -40°C to 140°C. As expected, specific heat capacity increased linearly with temperature. The IQR was similar across the temperature range, with the median value tending towards the first quartile. Linear regression of specific heat versus temperature was performed on all individual fuel samples and the resulting R^2 values were all >0.99. The median slope value was 0.0039 kJ/(kg·K^2) with 5th and 95th percentiles of 0.0036 and 0.0042 kJ/(kg·K^2), respectively.

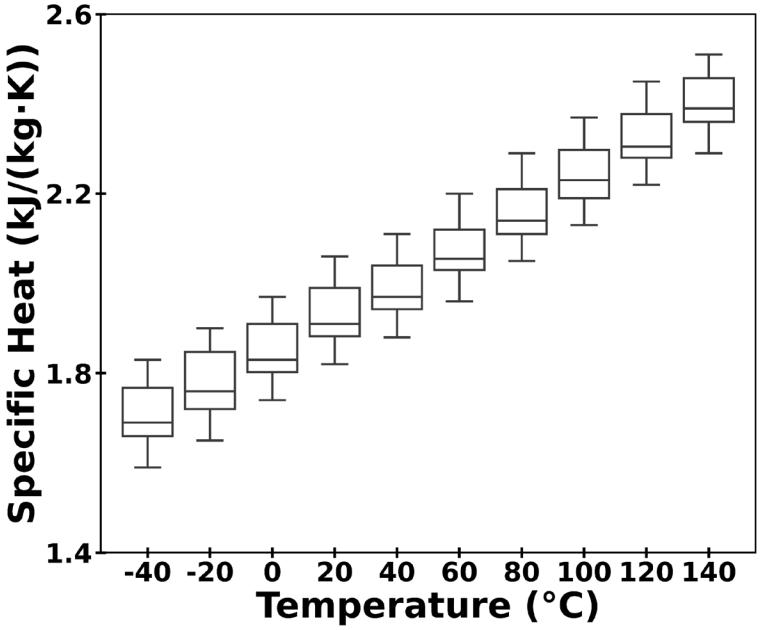

Figure 40. Box plot for specific heat capacity measured from -40°C to 140°C.

Density versus Temperature

Density was measured as a function of temperature following ASTM D4052-22: “Standard Test Method for Density, Relative Density, and API Gravity of Liquids by Digital Density Meter [30]. The instrumentation used was an Anton Paar SVM 3001. The repeatability for this method is 0.11 kg/m^3. Figure *41* shows a box plot of the measured density values from -40 to 100°C. The red lines represent the 15°C density specification limits of 775-840 kg/m^3 from ASTM D1655. All fuels were within the 15°C specification limits. The trend with temperature was as expected, with density decreasing at higher temperatures. At low temperatures, the median

value was centered in the IQR, indicating a normal distribution. At 80-100°C, the median value began to shift towards the third quartile, indicating a non-normal distribution. The range of the IQR increased slightly at 80-100°C, indicating increased variance at elevated temperatures. The R^2 for linear regression of density versus temperature was >0.999 for all the fuels.

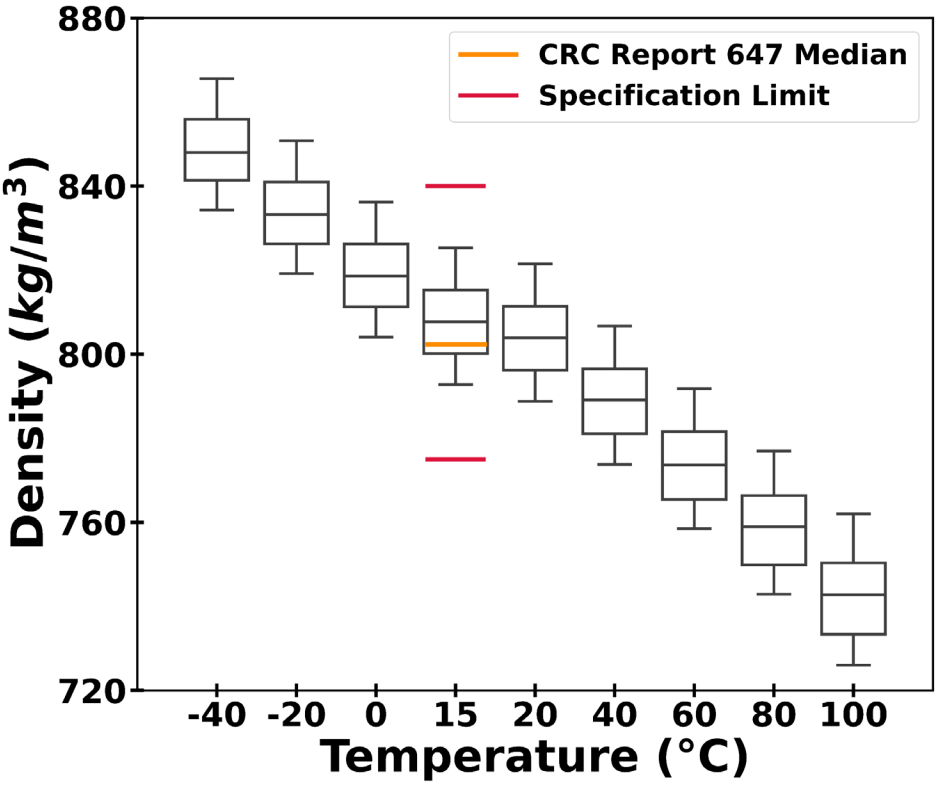

Figure 41. Box plot for density at the measured temperatures. The red lines represent the 15°C specification limits from ASTM D1655. The orange line represents the median value from CRC Report 647 corrected to 15°C.

Figure *42* is a histogram for density at 15°C. The distribution from this report generally aligns with CRC Report 647, which has been corrected from 60°F (15.6°C) to 15°C as described in the Appendix. The density values from CRC Report 647 were also measured following ASTM D4052. The current survey has a median density of 807.7 kg/m^3 at 15°C, which is 5.4 kg/m^3 higher than the median value of 802.3 kg/m^3 from CRC Report 647. The higher density in the current survey compared to CRC Report 647 may be caused by the concentration shift from *n*- and *iso*-alkanes to cycloalkanes.

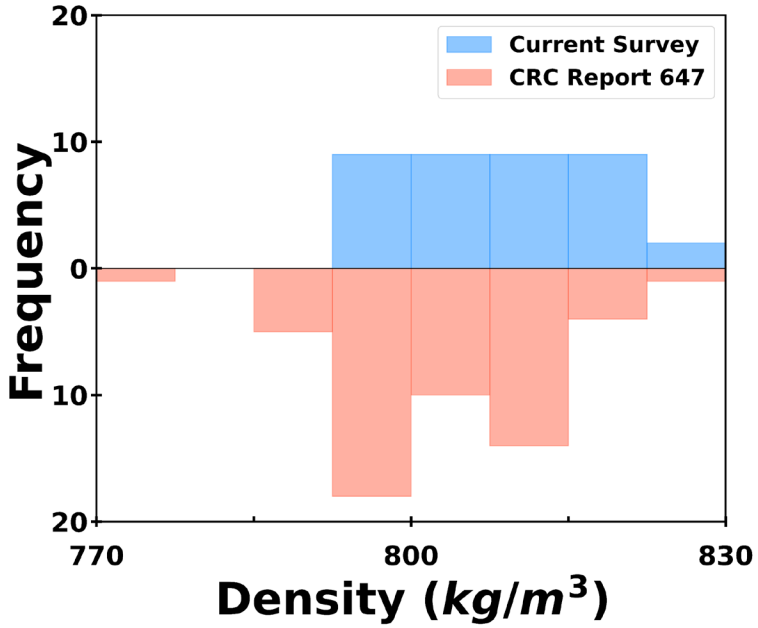

Figure 42. Histogram for density at 15°C, with the current survey on the top and CRC Report 647 on the bottom.

Surface Tension versus Temperature

Surface tension was measured following ASTM D1331-20: “Standard Test Methods for Surface and Interfacial Tension of Solutions of Paints, Solvents, Solutions of Surface-Active Agents, and Related Materials” [31]. The instrumentation used was a Krüss K100 Tensiometer (i.e., Wilhelmy Plate method). The repeatability limits in the ASTM method range from 0.335 to 6.655 mN/m (jet fuel was not included as one of the reference materials for the interlaboratory study). Figure *43* shows a box plot of surface tension at three different temperatures. Surface tension decreased with increasing temperature as expected. The median values from CRC Report 647 are within the IQR from the current survey and are higher than the median value from the current survey at -10°C and lower at 40°C. Surface tension was measured via ASTM D971 in CRC report 647. The R^2 for linear regression of surface tension versus temperature was >0.95 for all the fuels.

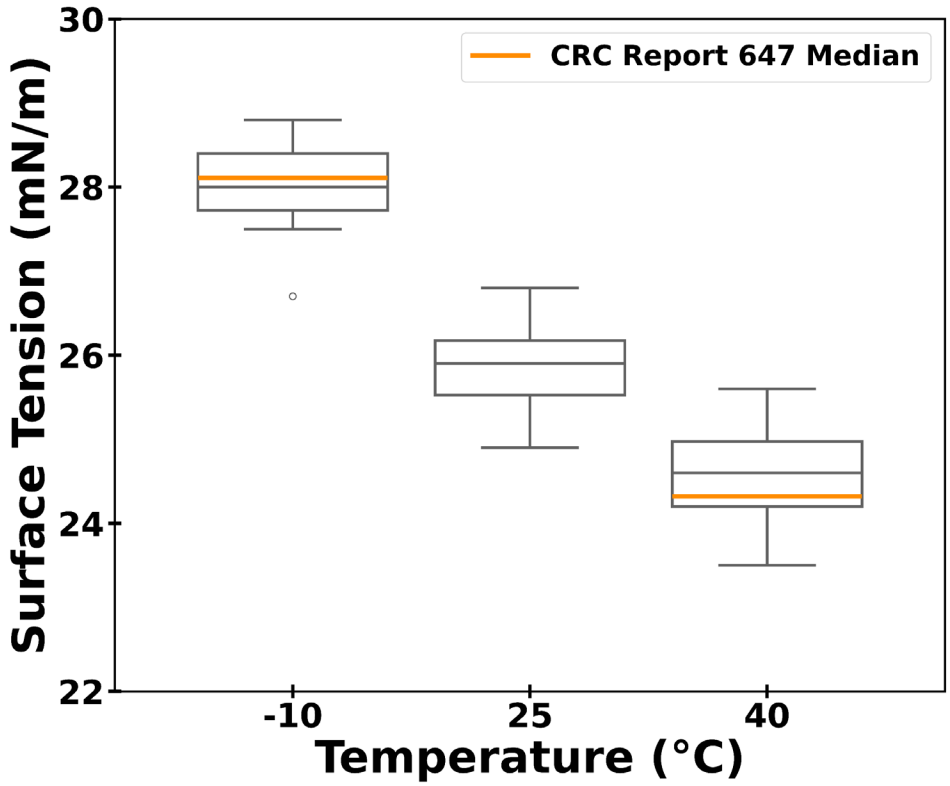

Figure 43. Box plot for surface tension at the temperatures tested. The orange line represents the median value from CRC Report 647.

Figure *44* is a violin plot for surface tension at the temperatures measured in CRC Report 647. The distribution from this report generally mirrored CRC Report 647, with CRC Report 647 having a slight bimodal distribution at both temperatures.

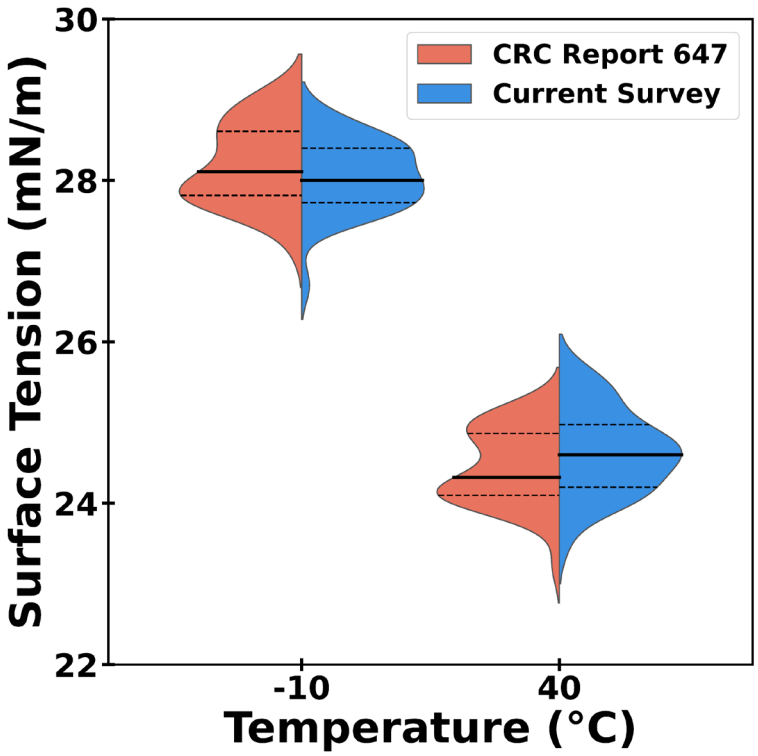

Figure 44. Violin plot for surface tension at the temperatures measured in CRC Report 647.

Isentropic Bulk Modulus versus Temperature and Pressure

Isentropic bulk modulus was run following FED-STD-791E Test Method 7507.0: "Isentropic Bulk Modulus of Aviation Turbine Fuels and Diesel Fuels" [32]. The instrumentation used was a custom-built rig using a Textronix TBS 1052B Digital Oscilloscope. No precision is available for this method. Figure *45* shows bulk modulus versus pressure, with temperature indicated by the legend. Bulk modulus was tested from 0 to 40 MPa and at three median temperatures: 34.8°C, 54.8°C, and 75.2°C. The standard deviation for the temperature was less than 0.1°C. The corresponding speed of sound values are also available in the Supplementary Data file. Bulk modulus increased with pressure and decreased with temperature. There was some overlap between temperature groups, especially as the pressure approached 40 MPa.

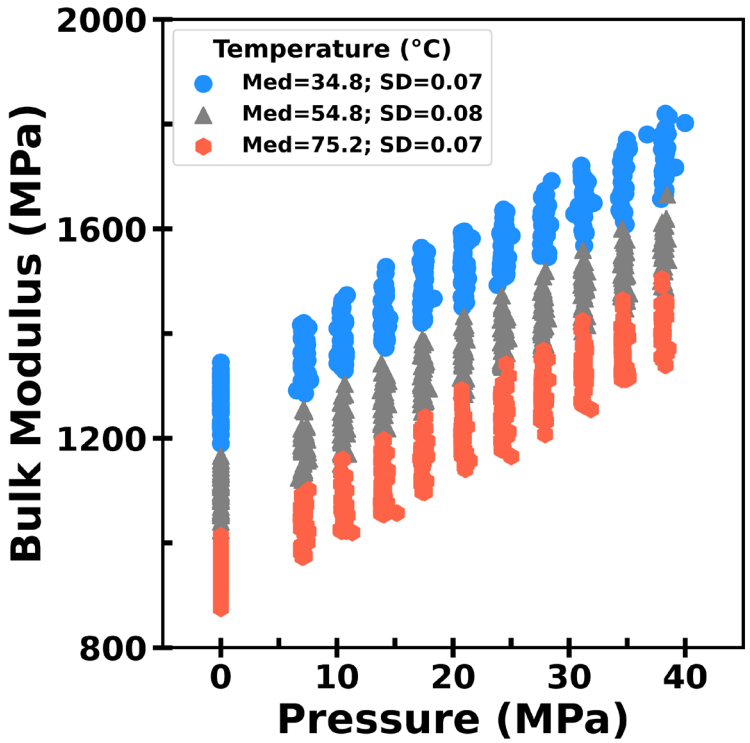

Figure 45. Scatter plot of bulk modulus temperature versus pressure, with the bulk modulus represented by the color map.

Thermal Conductivity versus Temperature

Thermal conductivity was measured following ASTM D7896-19: “Standard Test Method for Thermal Conductivity, Thermal Diffusivity, and Volumetric Heat Capacity of Engine Coolants and Related Fluids by Transient Hot Wire Liquid Thermal Conductivity Method” [33]. The instrumentation used was a Flucon Fluid Control GmbH LAMBDA Thermal Conductivity Meter. Repeatability limits ranged from 0.000135 W/m·K to 0.005534 W/m·K (jet fuel was not included as one of the reference materials for the interlaboratory study). Figure *46* shows a box plot of thermal conductivity at different temperatures. Median thermal conductivity values decreased with temperature. The R^2 for linear regression of thermal conductivity versus temperature was >0.97 for all the fuels.

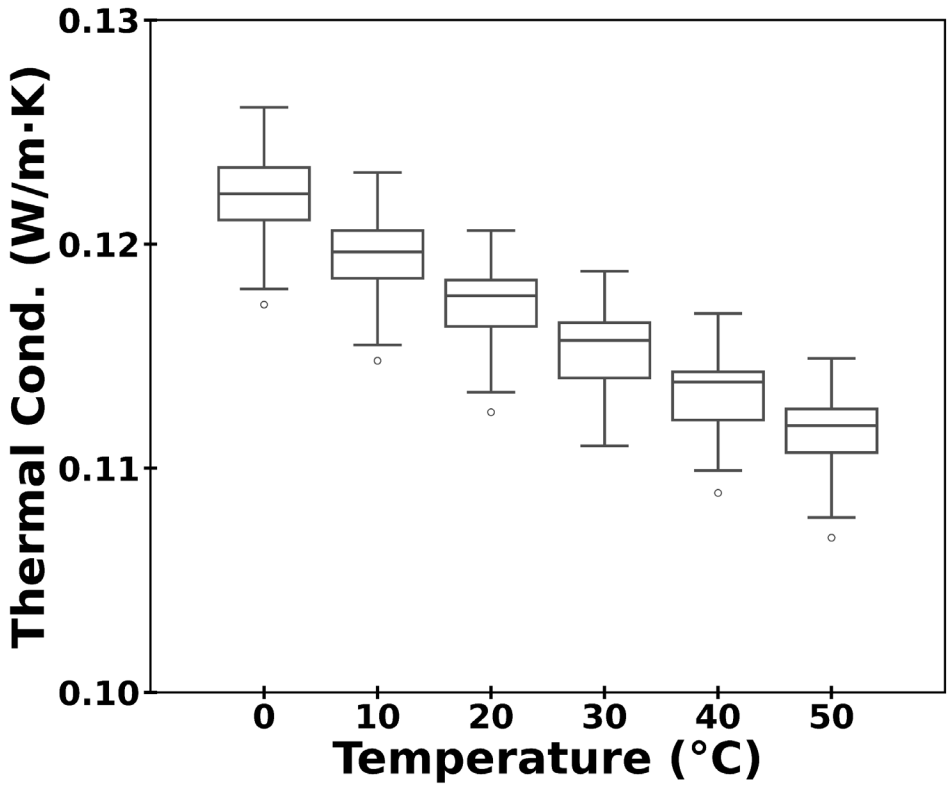

Figure 46. Box plot for thermal conductivity at the temperatures tested.

Water Solubility versus Temperature

To measure water solubility, a sample composed of 2 mL of reagent-grade water and 14 mL of fuel were sealed in a 20-mL septum vial. The vial was gently shaken and then placed in an oven or cold box and allowed to equilibrate to the test temperature. After approximately four hours, the vial was gently shaken again. The vial was then allowed to rest for a period of at least 24 hours at the test temperature. After the rest period, the sample was carefully withdrawn through the septum using a syringe without agitating the vial contents. The total water content of the sample was then measured following ASTM D6304-20: “Standard Test Method for Determination of Water in Petroleum Products, Lubricating Oils, and Additives by Coulometric Karl Fischer Titration” [34]. The instrumentation used was a Karl Fischer Moisture Meter Model CA-310 with direct injection. The repeatability for the ASTM method is $0.9810X^{0.7055}$ mg/kg. Repeatability values calculated using median water solubility values were: 17 mg/kg (0°C), 27 mg/kg (30°C), 33 mg/kg (40°C), and 38 mg/kg (50°C). Figure *47* shows a box plot of water solubility versus temperature. Median water solubility increased with temperature. The IQRs at the endpoints were the slightly larger, indicating higher variance. The 50°C results had the most

outliers, possibly due to the higher repeatability at this temperature. The R^2 of water solubility versus temperature was >0.79 for all the fuels.

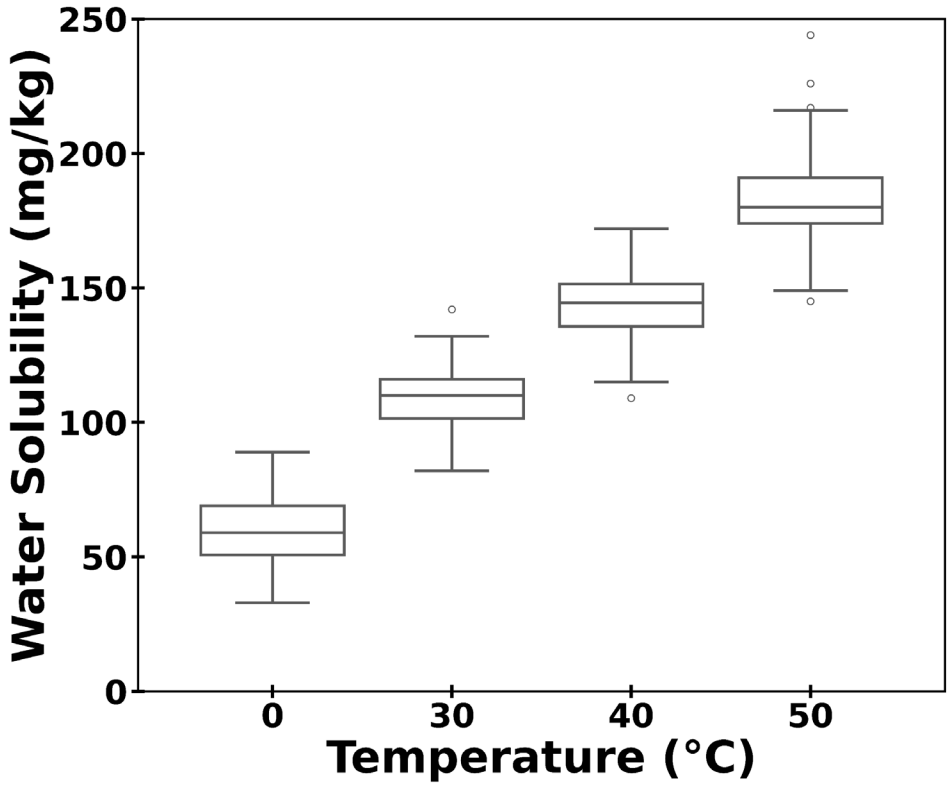

Figure 47. Water solubility box plot for the measured temperatures.

Air Solubility

Air solubility was measured using a LECO Paradigm Shift (i.e., Agilent 8890 with LECO BT TOFMS, PARADIGM flow modulator, and SHIFT FID/MS splitter) following UDRI FC-M-103: "Dissolved Gas Determination in Jet Fuel via GC-MS" [35]. According to the method, calibrations were performed using *n*-alkanes with known gas solubilities. Calibration fluids and samples were equilibrated with air at ambient conditions, i.e., 25°C and 1 atm. Calibration prediction RMSE values of 3.3, 1.8, and 0.1 ppm wt% were recorded for nitrogen, oxygen, and argon, respectively. Figure *48* shows a box plot of dissolved gas concentrations for nitrogen, oxygen, and argon, and their total (i.e., the sum of nitrogen, oxygen, and argon concentrations). These values are consistent with data reported elsewhere [36] [37].

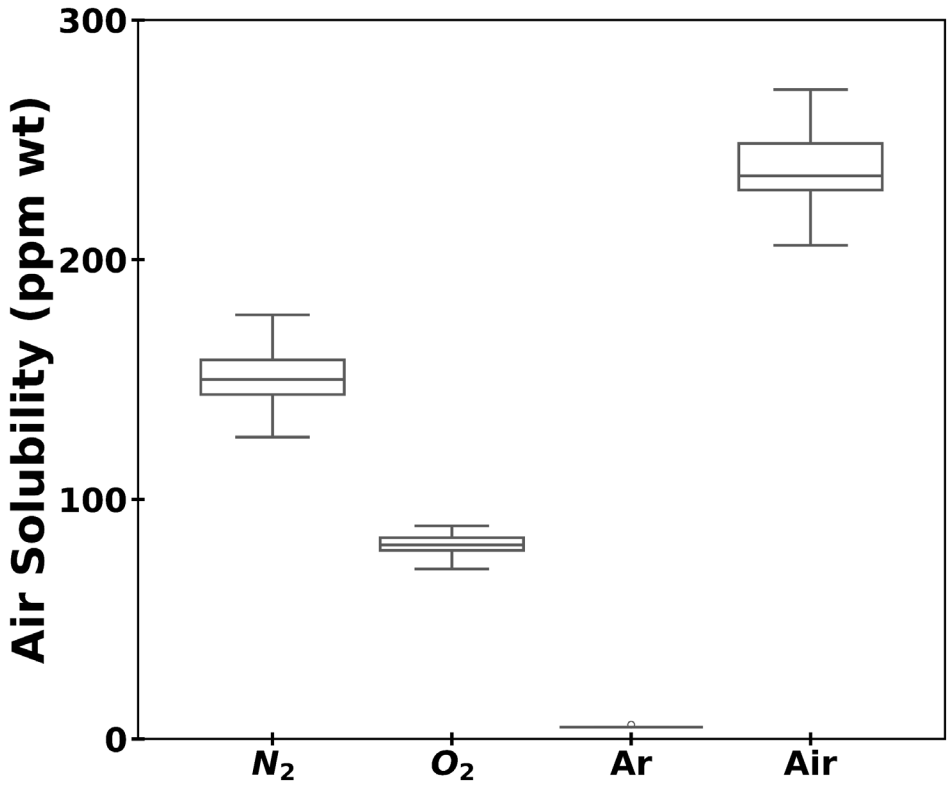

Figure 48. Air solubility box plot at 25°C. The box plot for air represents the total of the dissolved nitrogen, oxygen, and argon.

True Vapor Pressure versus Temperature

Vapor pressure was measured as a function of temperature following ASTM D6378-22: “Standard Test Method for Determination of Vapor Pressure (VPX) of Petroleum Products, Hydrocarbons, and Hydrocarbon-Oxygenate Mixtures (Triple Expansion Method)” [38]. The repeatability for this method is 0.52 kPa. The instrumentation used was a Ayalytical Eravap Vapor Pressure Instrument. Figure *49* shows a box plot of the vapor pressure from 0-120°C. The IQR increased at higher temperatures, indicating a greater variance.

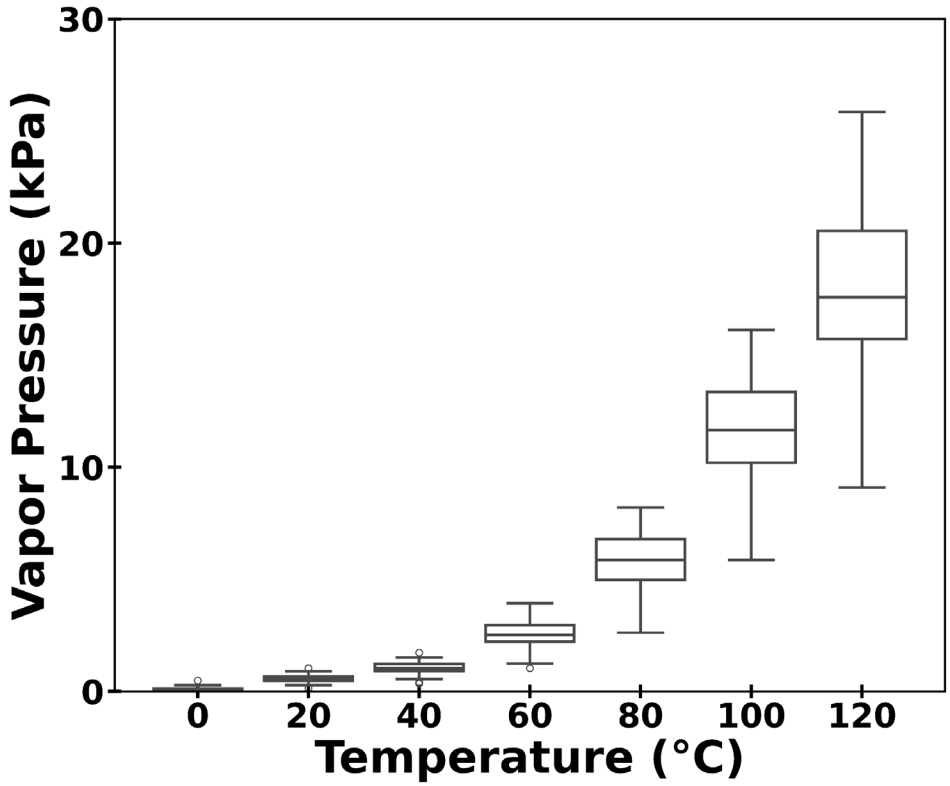

Figure 49. Vapor pressure box plot from 0°C to 120°C.

Refractive Index

Refractive index was measured at 20°C using a Reichert AR200 464 digital refractometer, which has a reported accuracy of 0.0001. Figure *50* shows a histogram of the measured refractive index values. The values are generally normally distributed, with the median value of 1.448 falling 0.002 above the CRC Report 647 median value. The median CRC temperature was 20.7°C, opposed to 20°C used in this paper. Additional data analysis coupling the refractive index with dielectric constant can be found in the Appendix.

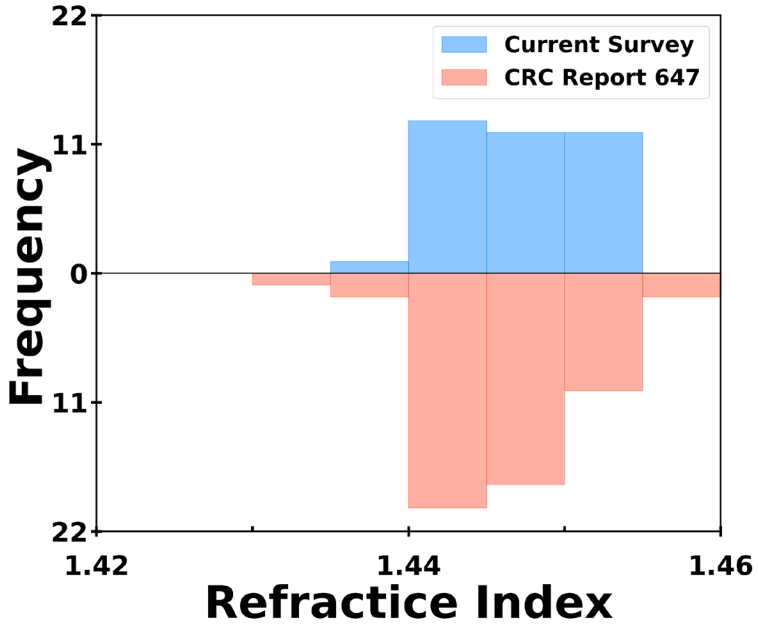

Figure 50. Histogram for refractive index at 20°C, with the current survey on the top and CRC Report 647 on the bottom.

Combustion

Derived Cetane Number

Derived cetane number (DCN) was measured following ASTM D6890-22: “Standard Test Method for Determination of Ignition Delay and Derived Cetane Number (DCN) of Diesel Fuel Oils by Combustion in a Constant Volume Chamber” [39]. The repeatability for this method is 0.01215(DCN + 3.5). The repeatability calculated using the median DCN of 43.5 is 0.6. The instrumentation used was a CFR Engines Ignition Quality Tester Model IQT-XLM. Figure *51* shows a histogram of the measured DCN values. The values are generally normally distributed, with a median value of 43.5.

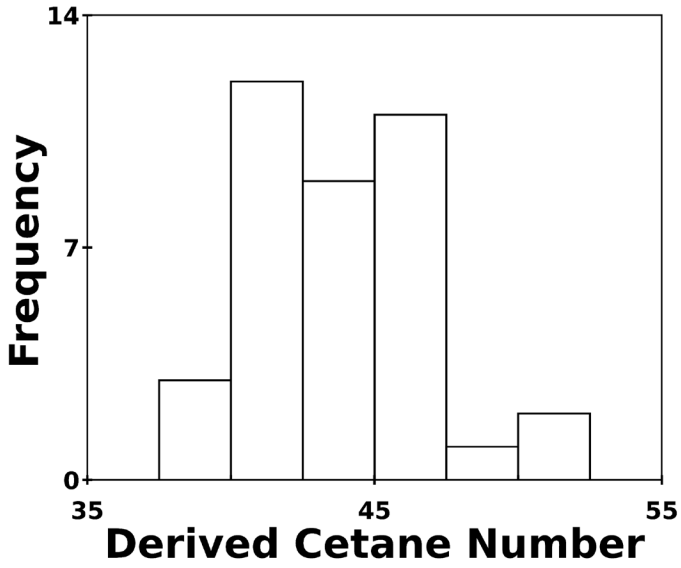

Figure 51. Histogram for DCN measurements from the current survey.

Indicated Cetane Number

Indicated cetane number was measured following ASTM D8183-18: “Standard Test Method for Determination of Indicated Cetane Number (ICN) of Diesel Fuel Oils using a Constant Volume Combustion Chamber— Reference Fuels Calibration Method” [40]. The instrumentation used was an AFIDA Indicated Cetane Number Analyzer. The repeatability for this method is $0.002931(ICN)^{1.47}$. Using the median ICN value of 43.7, the calculated repeatability was 0.8. Figure *52* is a histogram of the ICN measurements from the current survey. The ICN data were normally distributed, with a median value 0.2 higher than DCN.

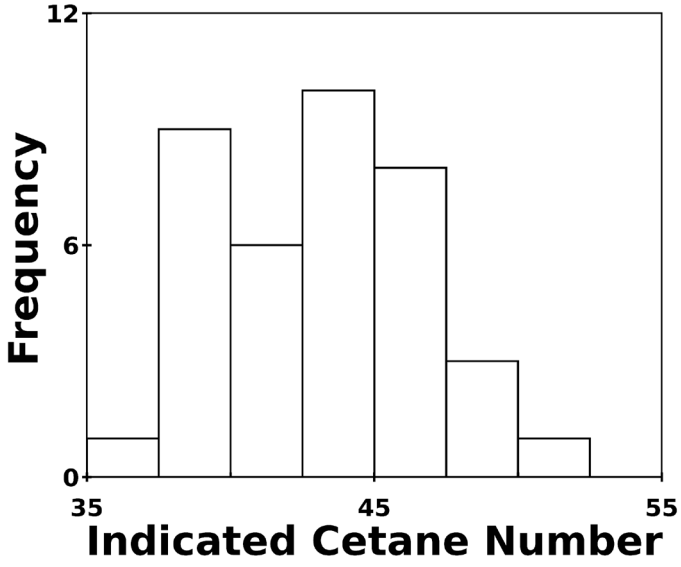

Figure 52. Histogram for ICN measurements from the current survey.

Electrical Properties

Dielectric Constant versus Density

Dielectric constant was measured as a function of temperature following IP 638: "Determination of Relative Permittivity (Dielectric Constant) of Aviation Fuels, Small Scale Automated Temperature Scanning Method" [41]. The instrumentation used was a Stanhope-Seta JetDC. Repeatability values for this method are $0.0006470(X - 1.000)$ and $988400(X^{-2.250})$ kg/m^3 for dielectric constant and density, respectively. Dielectric constant repeatability values calculated using the median measured values were 0.001 from 10-30°C. Figure *53* shows a box plot of the measured dielectric constant values from 10-30°C. Dielectric constant had an inverse correlation temperature. The IQR was consistent for all samples, with the median value falling slightly closer to the first quartile than the third quartile. The R^2 for linear regression of dielectric constant versus temperature was >0.999 for all the fuels in the current survey. The median value at 20°C from CRC Report 647 is slightly below the median from this report. The median CRC Report 647 temperature was 19.6°C, which likely increased the median dielectric constant value relative to 20°C. Dielectric constant was measured using a K-cell in CRC Report 647.

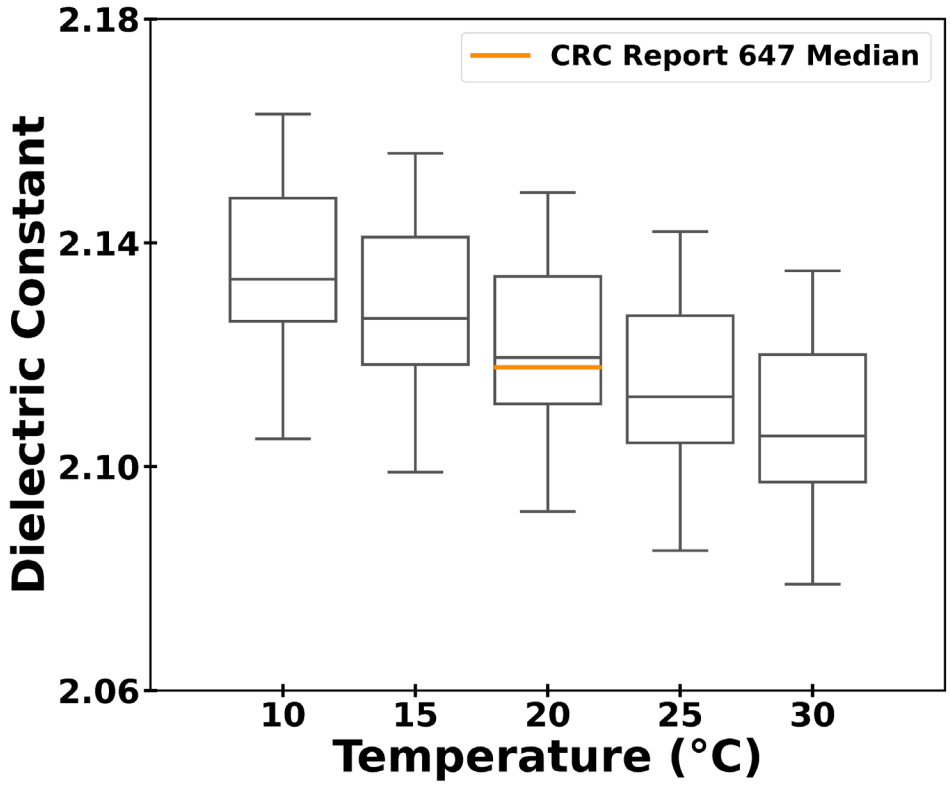

Figure 53. Box plots for dielectric constant at the measured temperatures. The orange line represents the median value from CRC Report 647.

Ground Handling Properties and Safety

Autoignition Temperature

Figure *54* shows a histogram of autoignition temperature measured following ASTM E659-24: “Standard Test Method for Autoignition Temperature of Chemicals” [42]. This method has a repeatability of 2% of the temperature in degrees Celsius. The instrumentation used was a Koehler 47000 Autoignition Apparatus. The median value was 239°C, and the data were skewed to the left of the median.

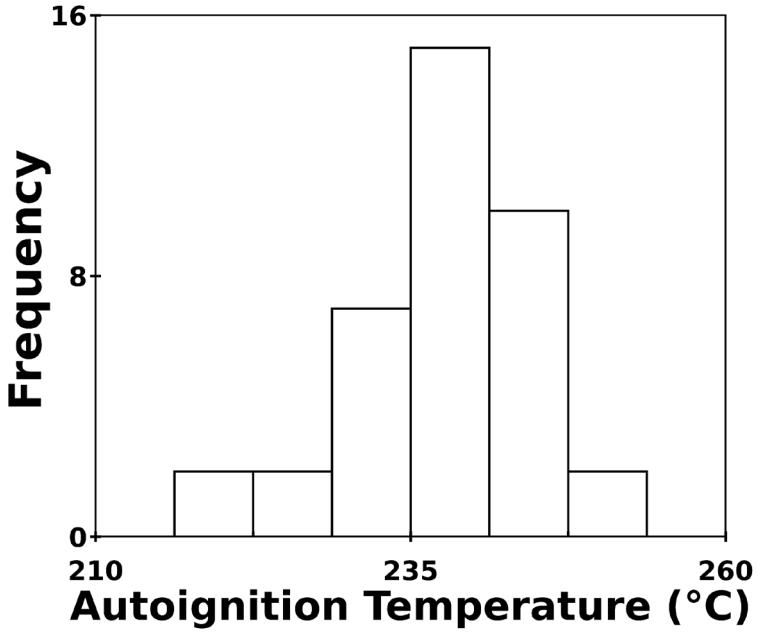

Figure 54. Histogram for autoignition temperature from the current survey.

Hot Surface (Manifold) Ignition Temperature

Hot surface ignition temperature was measured following ISO 20823 (2003): “Petroleum and related products — Determination of the flammability characteristics of fluids in contact with hot surfaces — Manifold ignition test” [43]. There is no precision available for this method. Figure *55* is a histogram of hot surface ignition temperature, which had a median value of 507°C.

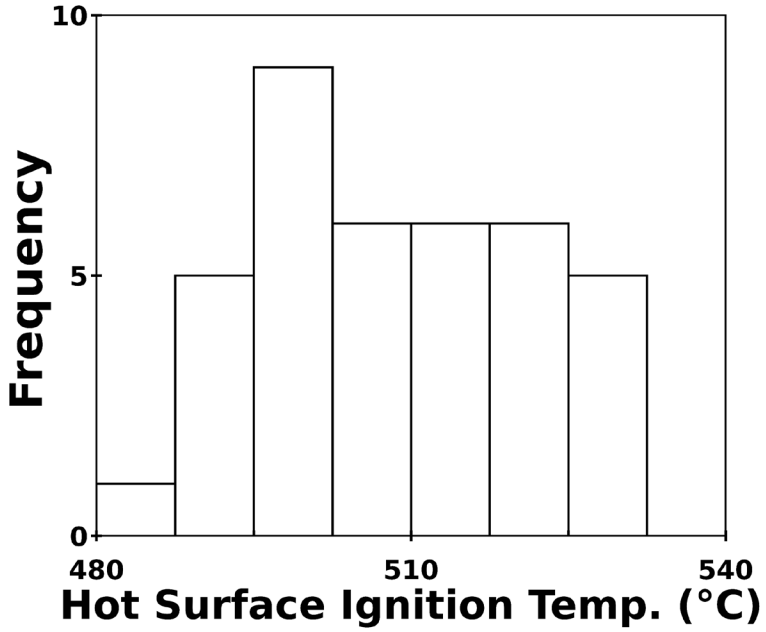

Figure 55. Histogram for hot surface ignition temperature.

4. Composition-to-Property Modeling

C2P models were trained using partial least squares regression to correlate fuel composition (i.e., hydrocarbon-type, polars, and/or trace elements) to the fuel properties measured for this report. The models take a quantitative composition-property relationship (QCPR) approach— as opposed to a quantitative structure-property relationship (QSPR) approach—because they correlate directly with the fuel composition rather than with molecular structure [44]. The models serve a few roles: 1) they provide an indication of how well the measured properties correlate with existing fuel composition measurement techniques, 2) when the model performance is good, the model coefficients provide insight into fuel chemistry, and 3) when the model performance is poor, the models indicate that experimental method development and/or more advanced modeling techniques are required. Because these models are trained solely on conventional fuels, the model coefficients are not applicable to synthetic aviation turbine fuel (SATF). Because PLS regression generally extrapolates poorly, these models should only be applied to fuels within the composition range of the training data. Using these models for SATF prescreening would require the inclusion of SATFs in the training data.

The modeling approach used in this report generally follows the literature [45]. A 1% variance threshold was used to downselect the training features, which were typically hydrocarbon-type, polars, or trace elements. PLS models were trained using k-fold cross-validation with 10 splits and 10 repeats to reduce the likelihood of overfitting. This involved randomly splitting the data into 10 folds, training a model on 9 of the folds, validating the model using the 10^{th} fold, and repeating the process 10 times. The root mean squared error (RMSE) and normalized root mean squared error (NRMSE) values were calculated across all k folds of cross-validation. Similarly, all k folds of cross-validation were used to calculate the mean predicted values in the parity plots. A maximum of four latent variables were used, which is an order of magnitude lower than the number of fuels in the training set ($n = 38$). The latent variable number that produced the lowest RMSE was selected for the reported model. To generate the model coefficients, a PLS model was trained using all the data. This was done, as opposed to using an average from the k-fold cross-validation for stability, because model coefficients can vary from model to model during the cross-validation.

A PLS model was trained for initial boiling point using Tier 3 GCxGC HTA. Species with carbon numbers less than 7 or greater than 12 were dropped. The left of Figure 56 shows a parity plot for the predicted and measured IBP values. A PLS model with three latent variables was used, which produced an RMSE value of 2.8°C. The NRMSE, calculated relative to the median measured IBP value, is 1.9%. Model coefficients are shown on the right of Figure 57. Model coefficients indicate the strength and sign of the correlation between the predictor and the response variables (in this case, GCxGC HTA and IBP, respectively). For instance, the large

negative coefficient for C7 monocycloalkanes indicates that this Tier 3 group decreases IBP. Model coefficients generally increased with carbon number for *n*-alkanes, *iso*-alkanes, and monocycloalkanes.

A simple regression model was trained to predict initial boiling point using total aromatics measured using GCxGC as the independent variable. The result was an RMSE of 6.2°C and a NRMSE of 4.2%, both of which are higher than the Tier 3 hydrocarbon type model below. The R^2 also decreased significantly from 0.89 to 0.07. This highlights the importance of using detailed hydrocarbon composition for property predictions.

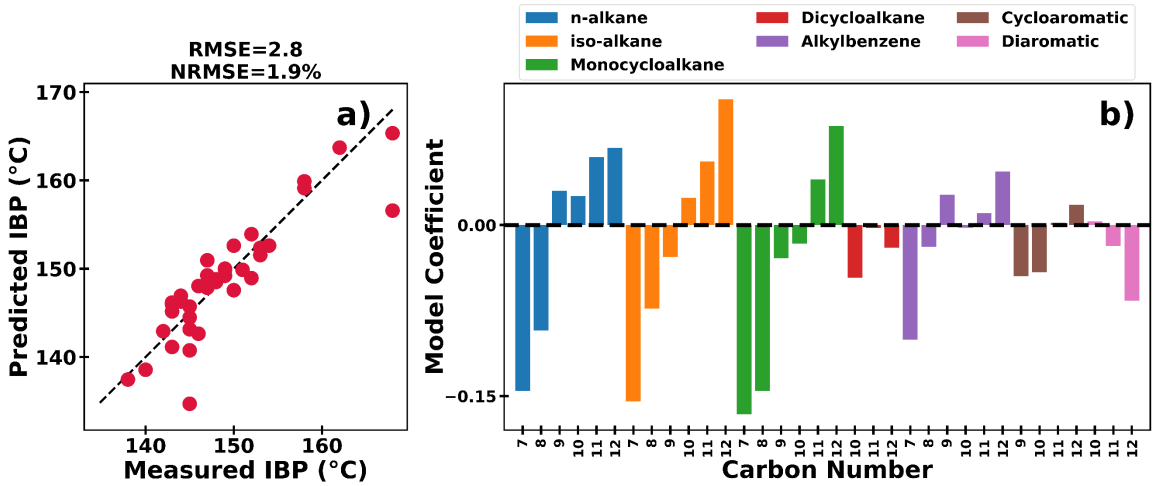

Figure 56. a) PLS initial boiling point predictions made using Tier 3 GCxGC HTA as training features. b) Model coefficients for the initial boiling point model.

A PLS model was trained for 10 vol% recovered (T10) using Tier 3 GCxGC HTA. The left of Figure 57 shows predicted versus measured T10 values. A PLS model with two latent variables was used, which produced an RMSE value of 2.5°C. The NRMSE, calculated relative to the median measured T10 value, is 1.4%. This NRMSE is lower than the 1.9% NRMSE for initial boiling point, possibly due to the due to combination of more robust D86 values for 10% recovered and higher concentrations of relevant hydrocarbons. Model coefficients are shown on the right of Figure 57. The *n*-alkane, *iso*-alkane, and cycloalkane model coefficients generally increased with carbon number.

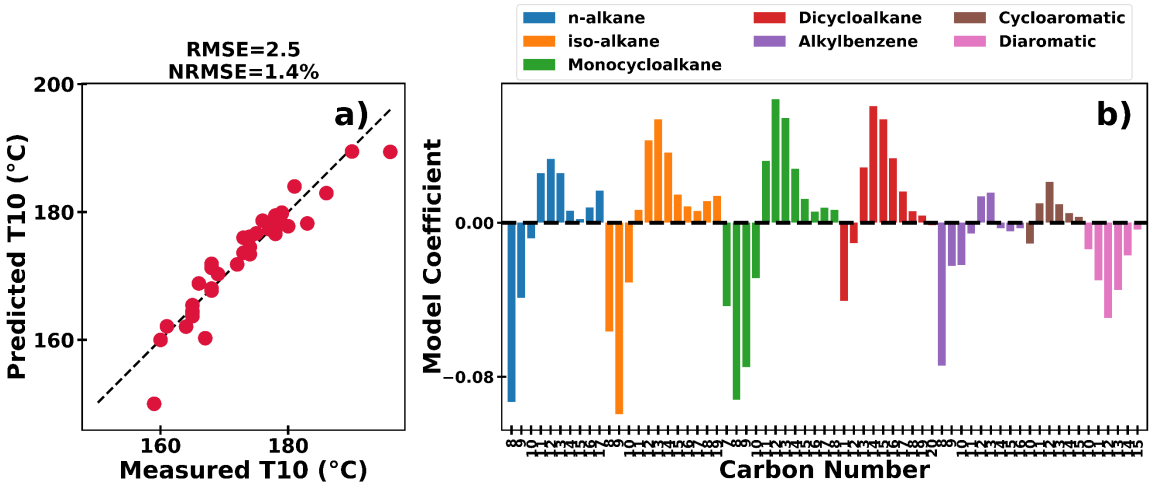

Figure 57. a) PLS 10 vol% recovered predictions made using Tier 3 GCxGC HTA as training features. b) Model coefficients for the PLS 10 vol% recovered model.

A PLS model was trained for final boiling point (FBP) using Tier 3 GCxGC HTA data. Figure *58* shows predicted versus measured FBP values. A PLS model with four latent variables was used, which produced RMSE and NRMSE values of 5.5°C and 2.0%, respectively. This NRMSE is 0.6% higher than that for T10, possibly due to the less robust D86 value for final boiling point and lower concentration of relevant species. The trend of model coefficient increasing from low to high carbon numbers was less consistent than the T10 model.

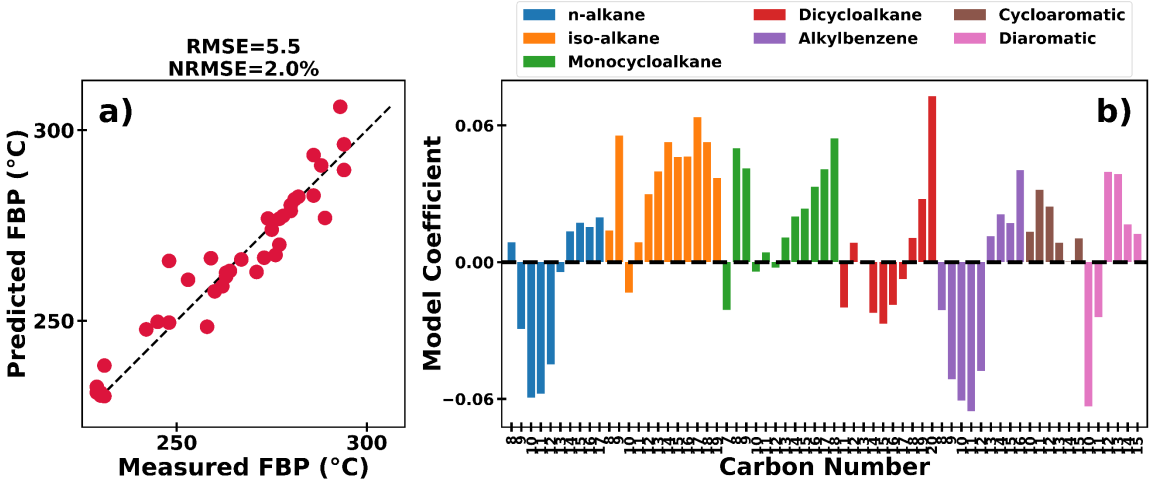

Figure 58. a) PLS final boiling point predictions made using Tier 3 GCxGC HTA as training features. b) Model coefficients for the PLS final boiling point predictions model.

Figure *59* shows a PLS model for breakpoint trained using polars, ASTM D4629 nitrogen, total sulfur (ASTM D2622, D4294, and D5453), and ASTM D1319 aromatics data. ASTM D1319 aromatics (i.e., Tier 1 hydrocarbon-type data) was included to capture bulk fuel composition with a minimum number of features. A model was trained using one latent variable. The resulting RMSE and NRMSE values were 19.4°C and 6.6%, respectively. The predictions did not fit the line of equality, with low values being overpredicted and high values being underpredicted (R^2 of 0.35). Two values with breakpoints of 370°C and 380°C were significantly underpredicted. The model coefficients are likely non-physical due to the low R^2.

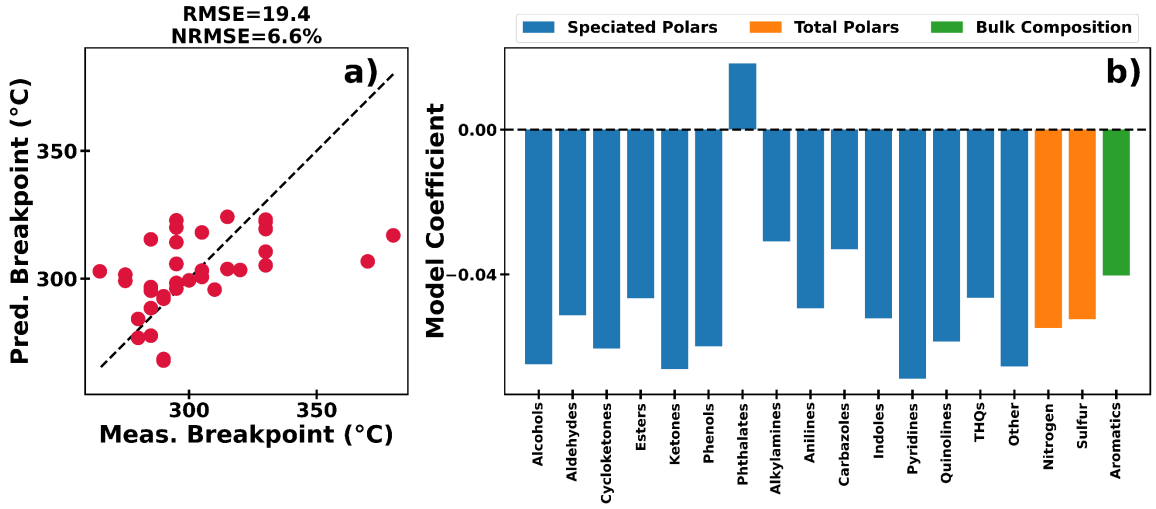

Figure 59. a) PLS breakpoint predictions made using trace polars, trace elements, and aromatics as training features. b) Model coefficients for the PLS breakpoint model.

Figure *60* shows a PLS model for QCM deposition trained using polars, ASTM D4629 nitrogen, total sulfur (ASTM D2622, D4294, and D5453), and ASTM D1319 aromatics data. The model was trained using one latent variable. The RMSE and NRMSE values were 5.6 µg/cm^2 and 81%, respectively. The high NRMSE is partially due to the low mean deposition value used to normalize the RMSE. Some high deposition fuels were also underpredicted. The model coefficients are likely non-physical due to the poor model performance.

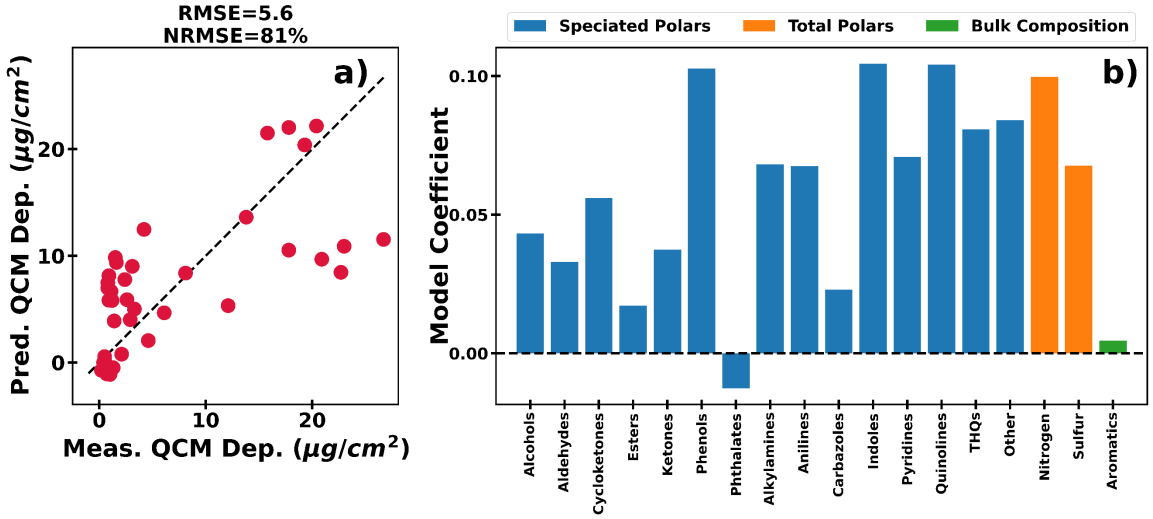

Figure 60. a) PLS QCM deposition predictions made using trace polars, nitrogen, sulfur, and aromatics as training features. b) Model coefficients for the PLS QCM deposition model.

Figure *61* shows a PLS model for WSD trained using Tier 3 HTA data. A model was trained using one latent variable. The RMSE and NRMSE values were 0.05 mm and 7.6%, respectively. The model underpredicted fuels with high WSD values. When polars were omitted, the NRMSE was slightly higher at 8.1%. Bulk hydrocarbon-type model coefficients had mixed signs, except for cycloaromatics and diaromatics, which had almost entirely positive and negative model coefficients, respectively. Polars had primarily negative model coefficients of a similar magnitude to diaromatics, except for phthalates.

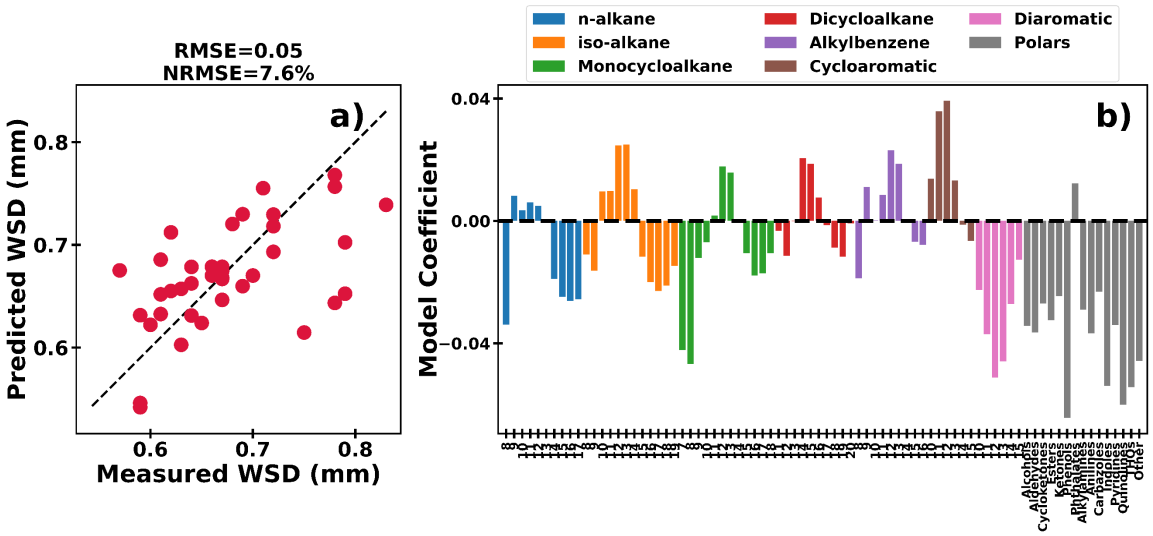

Figure 61. a) PLS WSD predictions using Tier 3 GCxGC HTA and polars as training features. b) Model coefficients for the PLS WSD model.

A PLS model was trained for viscosity at -20°C using Tier 3 GCxGC HTA data. The log of viscosity was taken before scaling the data. Figure *62* shows predicted versus measured viscosity values at -20°C, which have been converted back to the non-log scale. A PLS model with three latent variables was used, which produced RMSE and NRMSE values of 0.09 mm^2/s and 2.0%, respectively. The model coefficients generally increased from low to high carbon numbers as expected. A model trained without log scaling resulted in a higher NRMSE of 4.3%, largely due to underprediction of low-viscosity fuels.

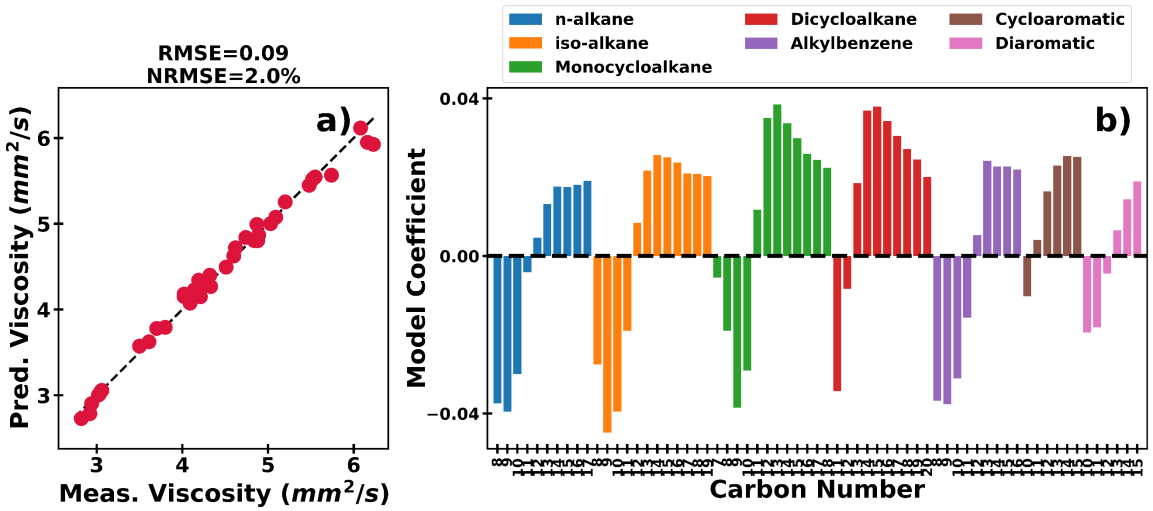

Figure 62. a) PLS -20°C viscosity predictions made using Tier 3 GCxGC HTA as training features. b) Model coefficients for the PLS viscosity model.

A PLS model was trained for specific heat capacity at 140°C using Tier 3 GCxGC HTA as features. Figure *63* shows a parity plot and model coefficients for the PLS model. A PLS model with one latent variable was used, which produced RMSE and NRMSE values of 0.06 kJ/(kg·K) and 2.7%, respectively. However, the R^2 score was low at -0.11. The model coefficients are likely not meaningful due to the low R^2 score. A similar model was trained to predict the slope of specific heat capacity versus temperature. This produced a NRMSE of 5.5% and an R^2 of -0.11.

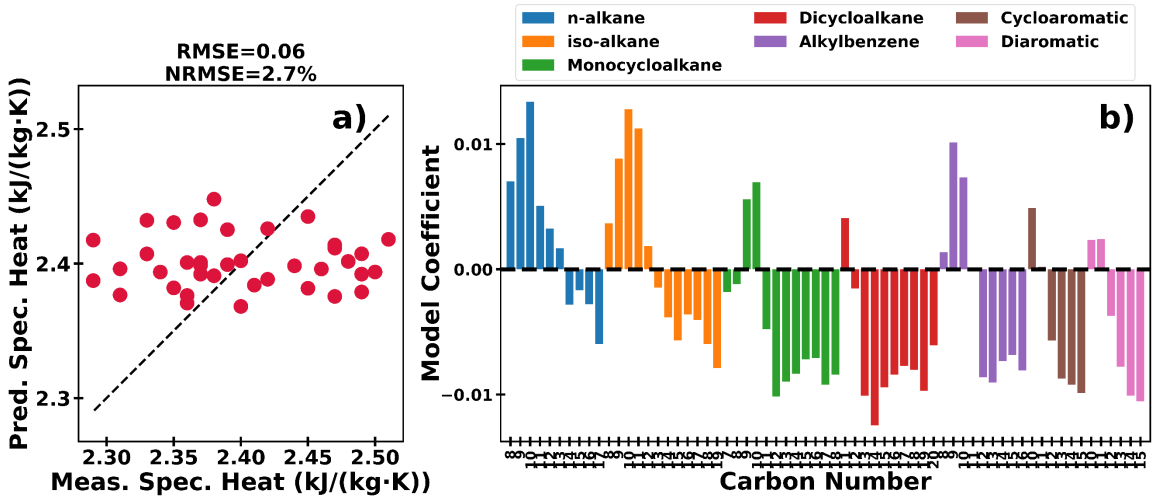

Figure 63. a) PLS 140°C specific heat capacity predictions made using Tier 3 GCxGC HTA as training features. b) Model coefficients for the PLS specific heat capacity model.

A PLS model was trained for density at 15°C using Tier 3 GCxGC HTA as features. Figure *64* shows predicted versus measured density values at 15°C. A PLS model with four latent variables was used, which produced RMSE and NRMSE values of 1.16 kg/m^3 and 0.1%, respectively. The model coefficients are generally as expected, with *n*- and *iso*-alkanes producing negative coefficients, and cycloalkanes and aromatics producing positive coefficients. Monocycloalkanes had lower coefficients than dicycloalkanes and aromatics. There was no consistent trend with carbon number within the molecular groups. It appears that hydrocarbon class exhibited a stronger influence on density than carbon number.

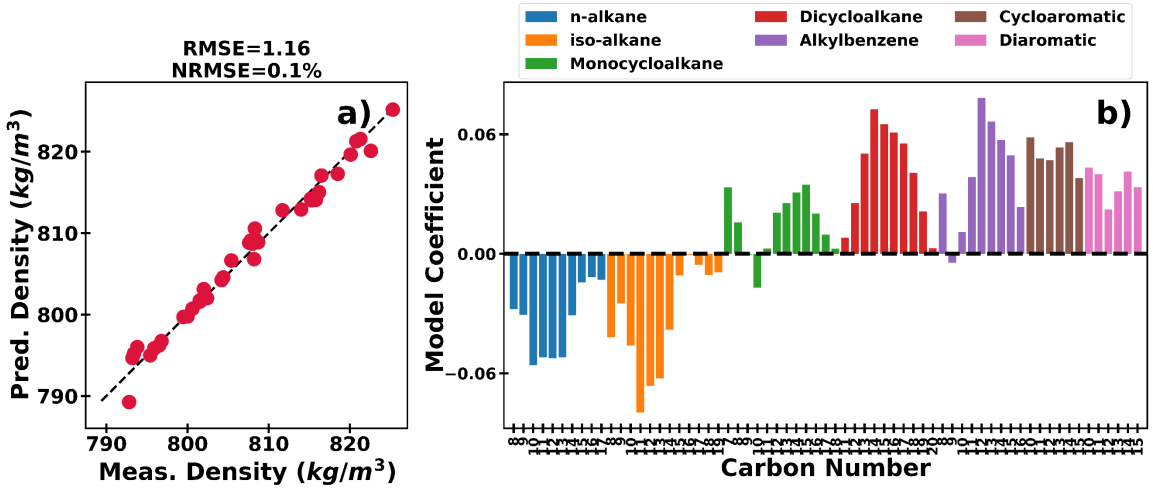

Figure 64. a) PLS density at 15°C predictions made using Tier 3 GCxGC HTA as training features. b) Model coefficients for the PLS density model.

Figure *65* shows a PLS model for surface tension at 25°C trained using Tier 3 HTA data. A model was trained using four latent variables. The RMSE and NRMSE values were 0.09 mN/m and 0.4%, respectively. The model coefficients indicate that *n*- and *iso*-alkanes generally decrease surface tension while cycloalkanes and aromatics increase it. This generally agrees with a Pearson correlation plot in the literature [46] that indicates strong positive correlations with cycloaromatics and dicycloalkanes and a strong negative correlation with *iso*-alkanes. The correlation between density and surface tension is a possible cause of these HTA correlations [47].

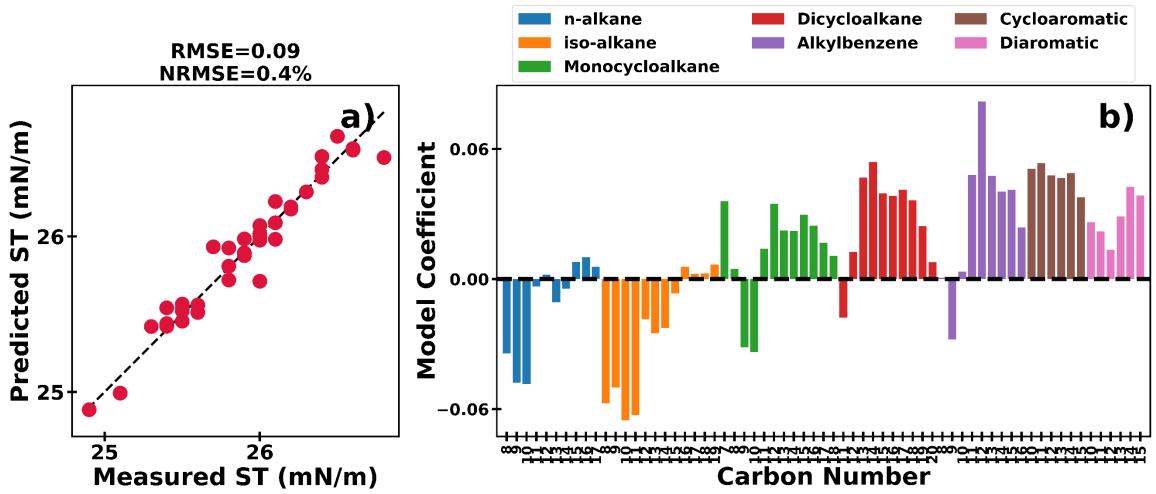

Figure 65. a) PLS surface tension predictions at 25°C using Tier 3 GCxGC HTA data. b) Model coefficients for the PLS surface tension model.

A PLS model was trained for bulk modulus using Tier 3 HTA data. Temperature and pressure were also used as training features, although they are not shown in Figure *66* because they have model coefficients 1-3 orders of magnitude larger than the HTA features. Specifically, temperature and pressure had model coefficients of -0.7 and 0.7, respectively, which agrees with the trends in Figure *45*. The RMSE and NRMSE values were 15.4 MPa and 1.1%, respectively. Model coefficients were generally negative for *n*- and *iso*-alkanes and positive for dicycloalkanes and aromatics. Monocycloalkanes had model coefficients that increased from negative to positive with increasing carbon number.

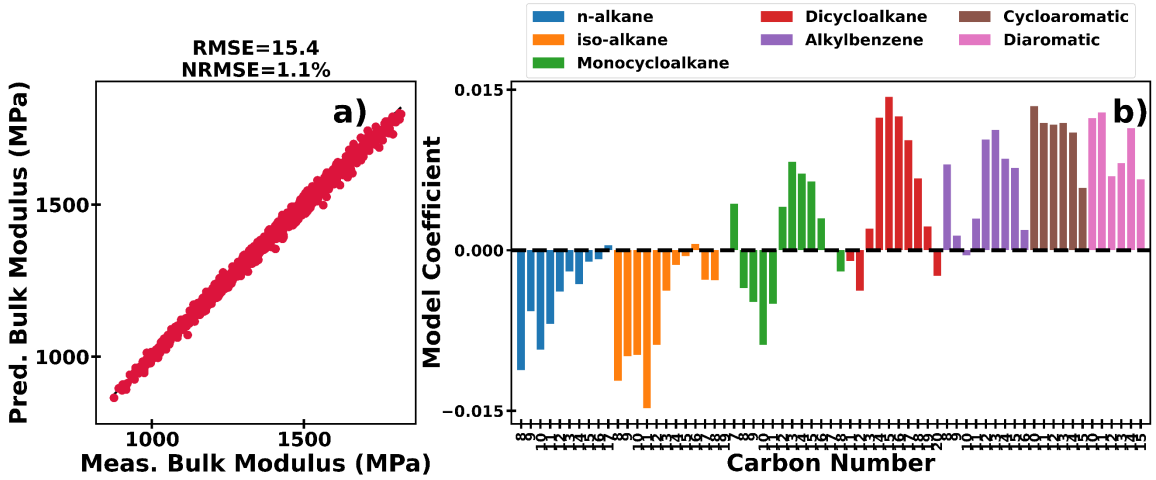

Figure 66. a) PLS bulk modulus predictions made using Tier 3 GCxGC HTA, temperature, and pressure as training features. b) Model coefficients for the PLS bulk modulus model.

A PLS model was trained for thermal conductivity at 50°C using Tier 3 HTA data. The model was trained with two latent variables. As shown in Figure *67*, the RMSE and NRMSE values were 0.0017 W/m·K and 1.6%, respectively. Despite the low NRMSE value, the R^2 value was only 0.07. The model coefficients are likely non-physical due to the poor model performance.

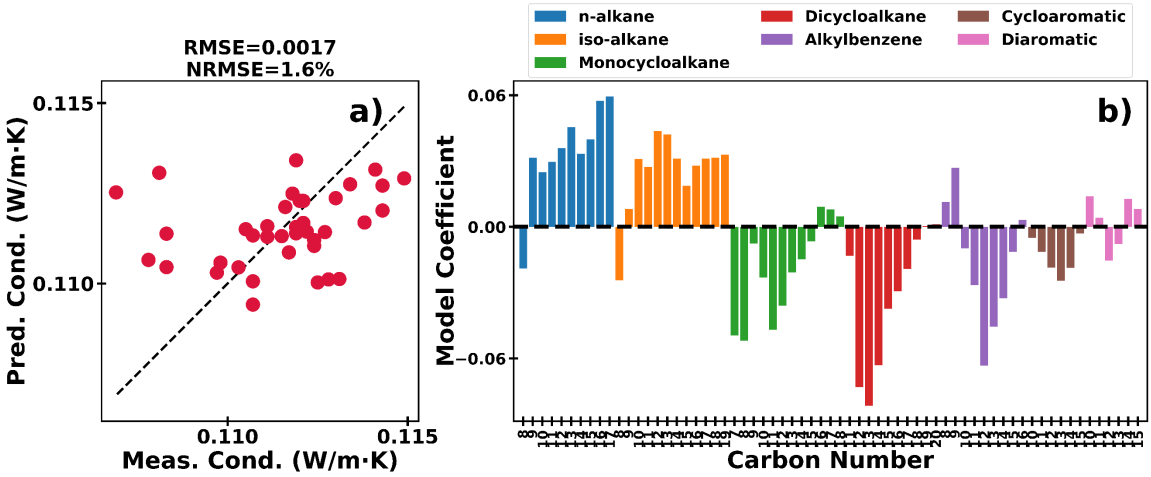

Figure 67. a) PLS thermal conductivity predictions made at 50°C using Tier 3 GCxGC HTA as training features. b) Model coefficients for the PLS thermal conductivity model.

A PLS model was trained for water solubility at 30°C using Tier 3 HTA data. The model was trained with one latent variable. As shown in Figure *68*, the RMSE and NRMSE values were 10.8 mg/kg and 9.9%, respectively. The data roughly agreed with the line of equality, with some low measured values being overpredicted and high measured values being underpredicted. Model coefficients generally decreased with increasing carbon number for *n*-alkanes, *iso*-alkanes, monocycloalkanes, and diaromatics. Including polars as inputs, in addition to Tier 3 HTA, increased the NRMSE from 9.9% to 10.0%, which is somewhat surprising given the know relevance of polars for interfacial tension [46]. It is possible that the significant number of inputs (80 for the HTA + polars model) resulted in too much noise and reduced the model performance.

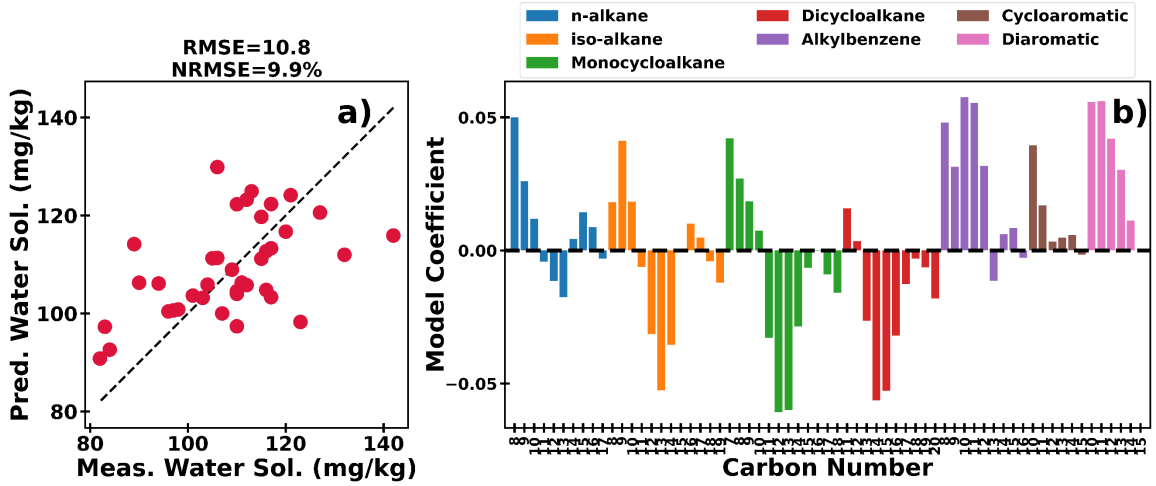

Figure 68. a) PLS water solubility predictions made at 30°C using Tier 3 GCxGC HTA as training features. b) Model coefficients for the PLS water solubility model.

A PLS model was trained for O_2 solubility at 24.8°C using Tier 3 HTA data. The model was trained with one latent variable. As shown in Figure *69*, the RMSE and NRMSE values were 3.0 ppm wt and 3.7%, respectively. Low O_2 solubility samples tended to be overpredicted. Model coefficients generally decreased with increasing carbon number within HTA groups.

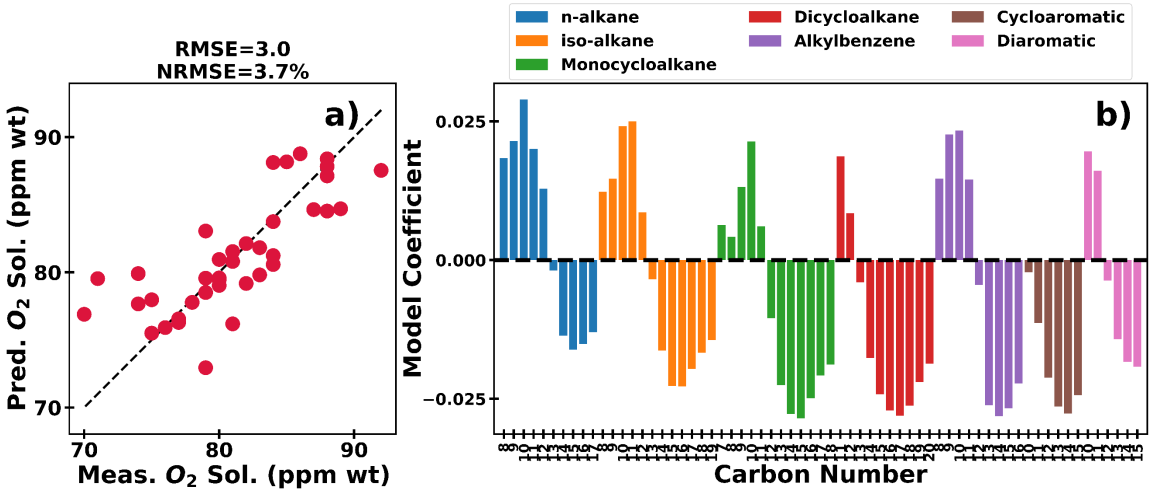

Figure 69. a) PLS O_2 solubility predictions made at 24.8°C using Tier 3 GCxGC HTA as training features. b) Model coefficients for the PLS O_2 solubility model.

A PLS model was trained for vapor pressure at 120°C using Tier 3 GCxGC HTA as features. Species with carbon numbers less than 7 or greater than 12 were dropped. Figure *70* shows predicted versus measured vapor pressure. The PLS model was trained with two latent variables. The RMSE and NRMSE values were 1.0 kPa and 5.6%, respectively. The model coefficients generally decreased from high to low carbon numbers, except for dicycloalkanes and alkylbenzenes, which had no discernable carbon number trend.

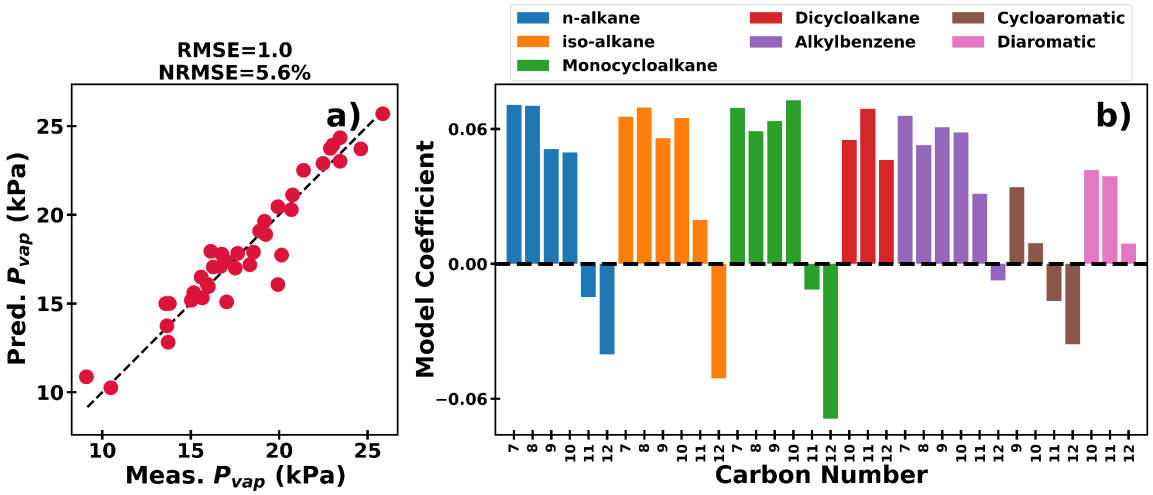

Figure 70. a) PLS vapor pressure predictions at 120°C made using Tier 3 GCxGC HTA as training features. b) Model coefficients for the PLS vapor pressure at 120°C model.

A PLS model was trained for refractive index at 20°C using Tier 3 GCxGC HTA as features. Figure *71* shows predicted versus measured refractive index values at 20°C. A PLS model with four latent variables was used. The RMSE and NRMSE values were 8.3×10^{-4} and 0.06%, respectively. The model coefficients were generally negative for saturates and positive for aromatics. Monocycloalkanes were an exception to this trend, with a mix of positive and negative coefficients. The refractive index model coefficients are similar to those of the dielectric constant PLS model shown later in this section.

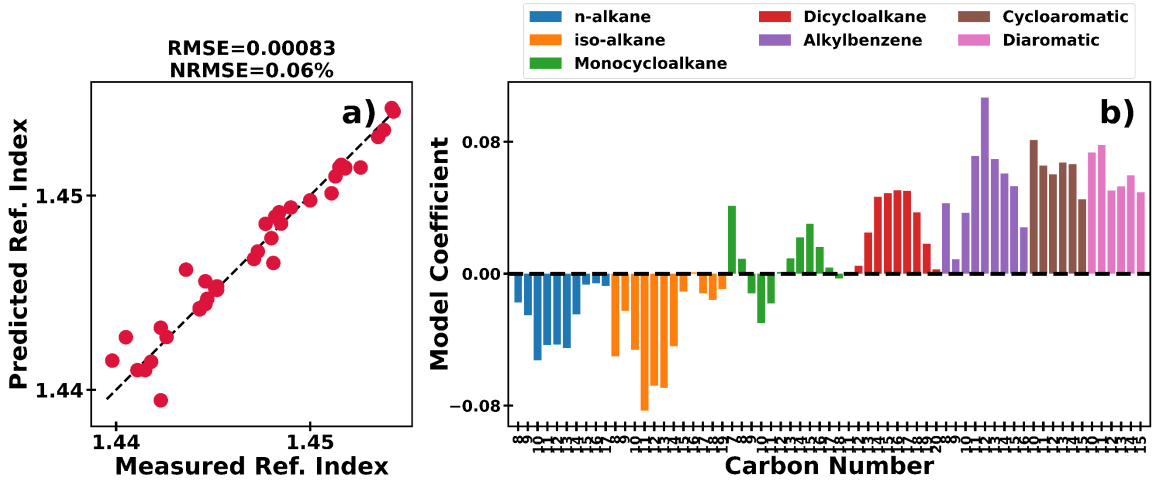

Figure 71. a) PLS refractive index predictions made using Tier 3 GCxGC HTA as training features. b) Model coefficients for the PLS refractive index model.

A PLS model was trained for DCN using Tier 3 GCxGC HTA as features. Figure *72* shows predicted versus measured DCN values. A PLS model with four latent variables was used. The RMSE and NRMSE values were 1.1 and 2.5%, respectively. Three fuels with high measured DCN values were slightly underpredicted. The model coefficients were positive for *n*- and *iso*-alkanes and negative for cycloalkanes and aromatics, except for diaromatics. No consistent trend with carbon number within the hydrocarbon groups was observed. The lack of correlation between the DCN model coefficients and carbon number is somewhat surprising for classes like *n*-alkanes where there is a known correlation between carbon number and DCN [48]. From Figure *75*, it is apparent that heavier *n*-alkanes (≥ CN 14) are present at relatively low concentrations and with relatively little fuel-to-fuel variance compared to *n*-alkanes present at higher concentrations (CN 9-13). The low concentration and variance of heavy *n*-alkanes could lead to unexpectedly low model coefficients.

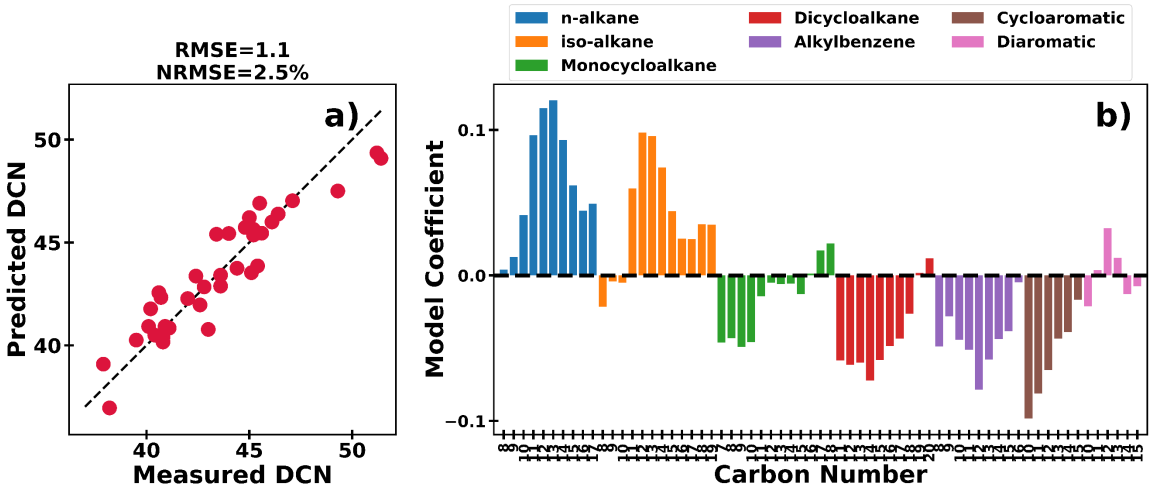

Figure 72. a) PLS DCN predictions made using Tier 3 GCxGC HTA as training features. b) Model coefficients for the PLS DCN model.

A PLS model was trained for dielectric constant at 20°C using Tier 3 GCxGC HTA as features. Figure *73* shows predicted versus measured dielectric constant values at 20°C. A PLS model with four latent variables was used. The RMSE and NRMSE values were 0.0045 and 0.2%, respectively. The model coefficients were generally negative for saturates and positive for aromatics. Dicycloalkanes were an exception to this trend, with primarily positive model coefficients. These trends agree with the literature, where a similar PLS model was trained with blends of synthetic blend components (SBCs) and Jet A [45]. The reason for the discrepancy in dicycloalkane model coefficients (i.e., positive here, negative in the literature) is uncertain. One possible explanation is that the literature only had two fuels—Jet A (POSF 10325) and cycloparaffinic kerosene (CPK)—with a significant amount of dicycloalkanes, whereas the fuels in this study had a median of 11.4 mass% dicycloalkanes.

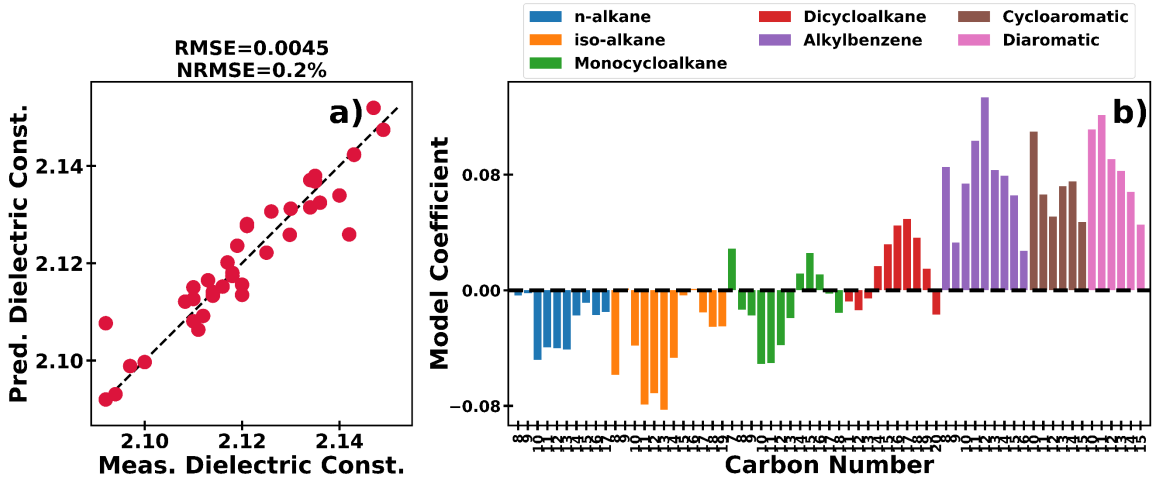

Figure 73. a) PLS dielectric constant predictions at 20°C made using Tier 3 GCxGC HTA as training features. b) Model coefficients for the PLS dielectric constant at 20°C model.

A PLS model was trained for autoignition using Tier 3 GCxGC HTA data as features. Figure *74* shows predicted versus measured autoignition values. A PLS model with two latent variables was used. The RMSE and NRMSE values were 7.3°C and 3.0%, respectively. Despite the low NRMSE, the data did not follow the line of equality (R^2 of 0.16). The model coefficients are likely non-physical due to the poor model performance. Some of the difficulty in predicting autoignition may come from the 2% measurement repeatability listed in ASTM E659-24 and the relatively low variance of autoignition (measured values range from 219-250°C).

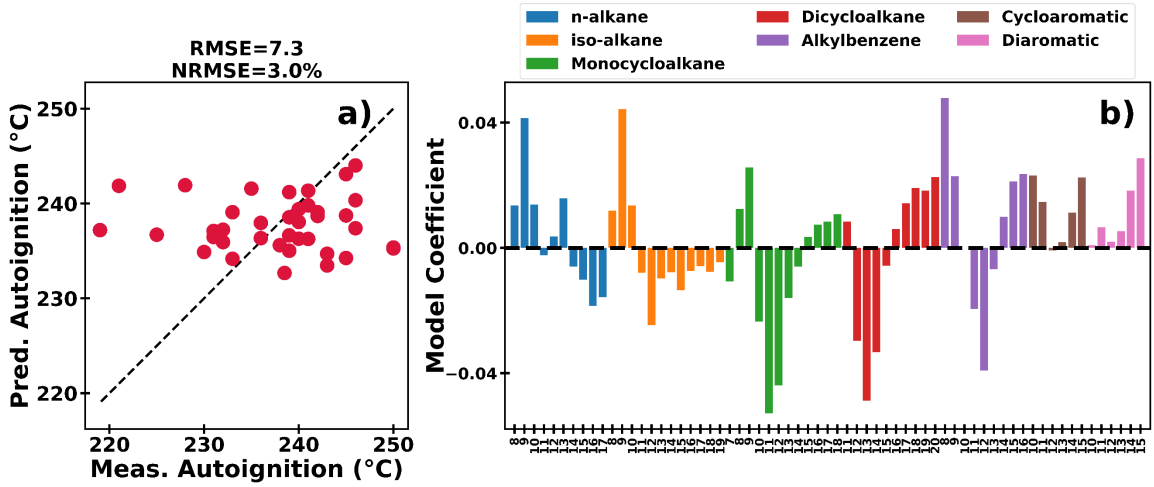

Figure 74. a) PLS autoignition predictions made using Tier 3 GCxGC HTA as training features. b) Model coefficients for the PLS autoignition model.

Acknowledgments

The authors acknowledge support from the U.S. Federal Aviation Administration Office of Environment and Energy through ASCENT, the FAA Center of Excellence for Alternative Jet Fuels and the Environment, Project 90 through FAA Award 13-C-AJFE-UD under the supervision of Ana Gabrielian and Anders Croft.

Although the FAA has sponsored this project through the Center of Excellence for Alternative Jet Fuels and Environment, it neither endorses nor rejects the findings of this research. The presentation of this information is in the interest of involving technical community comment on the results and conclusions of the research.

The University of Dayton Research Institute (UDRI) performed the following measurements: hydrocarbon-type, polars, trace elements, simulated distillation, QCM deposition, viscosity versus temperature, density versus temperature, air solubility, refractive index, and dielectric constant versus density. Southwest Research Institute (SwRI) performed the following measurements: aromatics, hydrogen, inorganics: N, distillation, breakpoint, lubricity, specific heat versus temperature, surface tension versus temperature, isentropic bulk modulus versus temperature and pressure, thermal conductivity versus temperature, water solubility versus temperature, true vapor pressure versus temperature, derived cetane number, autoignition temperature, and hot surface ignition temperature. ASG Analytik ran the indicated cetane number (ICN) measurements.

References

[1] "CRC Report 647," Coordinating Research Council, Alpharetta, 2006.

[2] "ASTM D4054-23: Standard Practice for Evaluation of New Aviation Turbine Fuels and Fuel Additives," ASTM International, West Conshohocken, 2023.

[3] Energy Institute, "EI/JIG Standard 1530 Quality assurance requirements for the manufacture, storage and distribution of aviation fuel to airports (A4)," Energy Institute Publications, London, 2019.

[4] "ASTM D1655-22a: Standard Specification for Aviation Turbine Fuels," ASTM International, West Conshohocken, 2022.

[5] "Defense Standard 91-091 Issue 18," Joint Inspection Group Limited, Cambourne, 2025.

[6] "Petroleum Quality Information System 2013 Annual Report," Defense Logistics Agency Energy, Fort Belvoir, 2013.

[7] "UDRI FC-M-101: Flow Modulation GCxGC for Hydrocarbon-Type Analysis of Conventional and Alternative Aviation Fuels," University of Dayton Research Institute, Dayton, 2018.

[8] "FED-STD-791F Test Method 7508.0: Method for Detailed Hydrocarbon Analysis of Middle Distillate Fuels by Two-Dimensional Gas Chromatography," Defense Logistics Agency, Fort Belvoir, 2024.

[9] C. Moses, "AFRL-RQ-WP-TR-2017-0091: Research for the Aerospace Systems Directorate (R4RQ)," Air Force Research Laboratory, Dayton, 2017.

[10] "ASTM D1319-20a: Standard Test Method for Hydrocarbon Types in Liquid Petroleum Products by Fluorescent Indicator Adsorption," ASTM International, West Conshohocken, 2020.

[11] "ASTM D8071-21: Standard Test Method for Determination of Hydrocarbon Group Types and Select Hydrocarbon and Oxygenate Compounds in Automotive Spark-Ignition Engine Fuel Using Gas Chromatography with Vacuum Ultraviolet Absorption Spectroscopy Detection," ASTM International, West Conshohocken, 2021.

[12] S. Kosir, J. Feldhausen, D. Bell, D. Cronin, R. Boehm and J. Heyne, "Quantitation of olefins in sustainable aviation fuel intermediates using principal component analysis coupled with vacuum ultraviolet spectroscopy," *Frontiers in Fuels,* vol. 1, pp. 1-6, 2023.

[13] "ASTM D6550-20: Standard Test Method for Determination of Olefin Content of Gasolines by Supercritical-Fluid Chromatography," ASTM International, West Conshohocken, 2020.

[14] "ASTM D3701-17: Standard Test Method for Hydrogen Content of Aviation Turbine Fuels by Low Resolution Nuclear Magnetic Resonance Spectrometry," ASTM International, West Conshohocken, 2017.

[15] "UDRI FC-M-102: Identification and Quantification of Polar Species in Conventional and Alternative Aviation Fuel Using SPE-GCxGC," University of Dayton Research Institute, Dayton, 2018.

[16] "ASTM D4629-17: Standard Test Method for Trace Nitrogen in Liquid Hydrocarbons by Syringe/Inlet Oxidative Combustion and Chemiluminescence Detection," ASTM International, West Conshohocken, 2017.

[17] University of Dayton Research Institute, "UDRI FC-M-107: Trace Elemental Determination in Jet Fuel via ICP-MS," University of Dayton Research Institute, Dayton, 2023.

[18] "ASTM D86-23: Standard Test Method for Distillation of Petroleum Products and Liquid Fuels at Atmospheric Pressure," ASTM International, West Conshohocken, 2023.

[19] "Critical Constants," in *CRC handbook of Chemistry and Physics 89th Edition*, Boca Raton, CRC Press, 2008, pp. 6-39 to 6-58.

[20] "ASTM D7566-22a: Standard Specification for Aviation Turbine Fuel Containing Synthesized Hydrocarbons," ASTM International, West Conshohocken, 2022.

[21] "ASTM D2887-23: Standard Test Method for Boiling Range Distribution of Petroleum Fractions by Gas Chromatography," ASTM International, West Conshohocken, 2023.

[22] "ASTM D3241-23a: Standard Test Method for Thermal Oxidation Stability of Aviation Turbine Fuels," ASTM International, West Conshohocken, 2023.

[23] S. Zabarnick, "Chemical Kinetic Modeling of Jet Fuel Autoxidation and Antioxidant Chemistry," *Ind. Eng. Chem. Res.,* vol. 32, no. 6, pp. 1012-1017, 1993.

[24] Z. West, S. Mueller, A. Waite and M. Greisenbrock, "Thermal Stability Assurance: Reference Tubes & Rating Correlations," in *CRC Aviation Meeting*, Portland, 2017.

[25] "ASTM D7739-11: Standard Practice for Thermal Oxidative Stability Measurement via Quartz Crystal Microbalance," ASTM International, West Conshohocken, 2020.

[26] "ASTM E177-20: Standard Practice for Use of the Terms Precision and Bias in ASTM Test Methods," ASTM International, West Conshohocken, 2020.

[27] "Standard Test Method for Measurement of Lubricity of Aviation Turbine Fuels by the Ball-on-Cylinder Lubricity Evaluator (BOCLE)," ASTM International, West Conshohocken, 2023.

[28] "ASTM D7042-21a: Standard Test Method for Dynamic Viscosity and Density of Liquids by Stabinger Viscometer (and the Calculation of Kinematic Viscosity)," ASTM International, West Conshohocken, 2021.

[29] "ASTM E2716-09: Standard Test Method for Determining Specific Heat Capacity by Sinusoidal Modulated Temperature Differential Scanning Calorimetry," ASTM International, West Conshohocken, 2014.

[30] "ASTM D4052-22: Standard Test Method for Density, Relative Density, and API Gravity of Liquids by Digital Density Meter," ASTM International, West Conshohocken, 2022.

[31] "ASTM D1331-20: Standard Test Methods for Surface and Interfacial Tension of Solutions of Paints, Solvents, Solutions of Surface-Active Agents, and Related Materials," ASTM International, West Conshohocken, 2020.

[32] "FED-STD-791E Test Method 7507.0: Isentropic Bulk Modulus of Aviation Turbine Fuels and Diesel Fuels," Defense Logistics Agency, Fort Belvoir, 2015.

[33] "ASTM D7896-19: Standard Test Method for Thermal Conductivity, Thermal Diffusivity, and Volumetric Heat Capacity of Engine Coolants and Related Fluids by Transient Hot Wire Liquid Thermal Conductivity Method," ASTM International, West Conshohocken, 2019.

[34] "ASTM D6304-20: Standard Test Method for Determination of Water in Petroleum Products, Lubricating Oils, and Additives by Coulometric Karl Fischer Titration," ASTM International, West Conshohocken, 2020.

[35] "UDRI FC-M-103: Dissolved Gas Determination in Jet Fuel via GC-MS," University of Dayton Research Institute, Dayton, 2017.

[36] J. T. Edwards, "AFRL-RQ-WP-TR-2020-0017: Jet Fuel Properties," US Air Force Research Laboratory, Wright-Patterson Air Force Base, Dayton, 2020.

[37] C. Anderson, A. M. Arts, R. Cook, S. S. Mueller and Z. J. West, "CRC AV-27-18: Measurement of Aviation Fuel Properties Relevant for the Estimation of V/L Ratio Parameter Calculation," Coordinating Research Council, Alpharetta, 2022.

[38] "ASTM D6378-22: Standard Test Method for Determination of Vapor Pressure (VPX) of Petroleum Products, Hydrocarbons, and Hydrocarbon-Oxygenate Mixtures (Triple Expansion Method)," ASTM International, West Conshohocken, 2022.

[39] "Standard Test Method for Determination of Ignition Delay and Derived Cetane Number (DCN) of Diesel Fuel Oils by Combustion in a Constant Volume Chamber," ASTM International, West Conshohocken, 2022.

[40] "Standard Test Method for Determination of Indicated Cetane Number (ICN) of Diesel Fuel Oils using a Constant Volume Combustion Chamber— Reference Fuels Calibration Method," ASTM International, West Conshohocken, 2018.

[41] "IP 638: Determination of Relative Permittivity (Dielectric Constant) of Aviation Fuels, Small Scale Automated Temperature Scanning Method," Energy Institute, London, 2023.

[42] "ASTM E659-24: Standard Test Method for Autoignition Temperature of Chemicals," ASTM International, West Conshohocken, 2024.

[43] "ISO 20823: “Petroleum and related products — Determination of the flammability characteristics of fluids in contact with hot surfaces — Manifold ignition test”," International Organization for Standardization, Geneva, 2003.

[44] C. Hall, B. Rauch, U. Bauder and M. Aigner, "Comparison of probabilistic jet fuel property models for the fuel screening and design," *Fuel,* vol. 351, 2023.

[45] S. Kosir, A. Landsaw, W. H. Steinecker, Z. J. West and S. Zabarnick, "Synthetic Blend Component Study: The Effects of Hydrocarbon Composition on Aviation Fuel Dielectric Constant," *Energy & Fuels,* 2024.

[46] S. Kosir, S. Mueller, L. Brown, J. Thompson, R. Cook, Z. West and E. Corporan, "Measurement of Jet Fuel Interfacial Tension and its Relation to Micro-Separometer Data," in *IASH 2024*, Louisville, 2024.

[47] Z. J. West, T. Yamada, C. R. Bruening, R. L. Cook, S. S. Mueller, L. M. Shafer, M. J. DeWitt and S. Zabarnick, "Investigation of Water Interactions with Petroleum-Derived and Synthetic Aviation Turbine Fuels," *Energy & Fuels,* vol. 32, pp. 1166-1178, 2018.

[48] J. Yanowitz, M. Ratcliff, R. McCormick, J. Taylor and M. Murphy, "Compendium of Experimental Cetane Numbers," National Renewable Energy Laboratory, Golden, 2017.

[49] D. Deans, "A new gas sampling device for gas chromatography," *J. Chrom. A,* vol. 289, pp. 43-51, 1984.

[50] J. Seeley, N. Micyus, J. McCurry and S. Seeley, "Comprehensive Two-Dimensional Gas Chromatography With a Simple Fluidic Modulator," *Am. Lab.,* 2006.

[51] J. Griffith, W. Winniford, K. Sun, R. Edam and J. Luong, "A reversed-flow differential flow modulator for comprehensive two-dimension gas chromatography," *J. Chrom. A,* vol. 1226, pp. 116-123, 2012.

[52] GC Image, LLC, "About GC Image," GC Image, LLC, [Online]. Available: https://www.gcimage.com/about.html. [Accessed 24 January 2025].

[53] US Department of Health and Human Services, "15th Report on Carcinogens: Cumene," US Department of Health and Human Services, Washington, D.C., 2021.

[54] W. McCabe and J. Smith, Unit Operations of Chemical Engineering, New York: McGraw-Hill, 1976.

[55] "Adjunct to: ASTM D 1250-04 and IP 200/04: Manual of Petroleum Measurement Standards Chapter 11—Physical Properties Data," ASTM International, West Conshohocken, 2019.

[56] "Aviation Fuels Technical Review," Chevron Corporation, 2006.

[57] S. Kosir, J. Heyne and J. Graham, "A machine learning framework for drop-in volume swell characteristics of sustainable aviation fuel," *Fuel,* vol. 274, 2020.

[58] S. Kosir, R. Stachler, J. Heyne and F. Hauck, "High-performance jet fuel optimization and uncertainty analysis," *Fuel,* vol. 281, 2020.

[59] S. Zabarnick, "Studies of Jet Fuel Thermal Stability and Oxidation Using a Quartz Crystal Microbalance and Pressure Measurements," *Industrial & Engineering Chemistry Research,* vol. 33, pp. 1348-1354, 1994.

[60] S. P. Heneghan and R. E. Kauffman, "Analytic Tests and Their Relation to Jet Fuel Thermal Stability," in *5th International Conference on Stability and Handling of Liquid Fuels*, Rotterdam, 1994.

[61] Z. Yang, D. C. Bell, R. Boehm, P. F. Marques, J. A. Boze, I. V. Kosilkin and J. Heyne, "Assessing the Effect of Composition on Dielectric Constant of Sustainable Aviation Fuel," *Fuel,* vol. 380, 2025.

[62] "ARINC611-1: Guidance for the Design and Installation of Fuel Quantity Systems," ARINC, Cedar Rapids, Iowa, 1999.

[63] S. R. Panuganti, F. M. Vargas and W. G. Chapman, "Property Scaling Relations for Nonpolar Hydrocarbons," *I&EC Research,* vol. 52, no. 23, pp. 8009-8020, 2013.

[64] F. M. Vargas, D. L. Gonzalez, J. L. Creek, J. Wang, J. Buckley, G. J. Hirasaki and W. G. Chapman, "Development of a General Method for Modeling Asphaltene Stability," *Energy & Fuels,* vol. 23, no. 3, p. 1147–1154, 2009.

Supplementary Data

An Excel spreadsheet with all the data from this survey is included as a Supplementary Data file. This includes data for the properties discussed above and CoA data from fuel suppliers. The data in the Excel sheet are rounded to match the repeatability limits. For example, ASTM D86 initial boiling point has a repeatability of 2.7°C, and the data have been rounded to the nearest whole number. The CoA data are reported as received from fuel suppliers (i.e., no rounding to match repeatability limits). The “Method min” and “Method max” columns refer to experimental limits of detection, not specification limits.

Appendix

Appendix A: Hydrocarbon-Type

Hydrocarbon-type analysis was performed using an Agilent GC (Agilent 8890, Santa Clara, CA) outfitted with a capillary flow technology (CFT) reverse fill flush modulator (5994-0157), associated pneumatic switching device (PSD), and modulator valve, all operated with hydrogen carrier gas set to constant flow. The first column ("non-polar") dimensions were 40 m x 0.18 mm with a 180-nm 5% phenyl, 95% methyl polysiloxane stationary phase. The second-dimension separation ("polar") was performed on a 5 m x 0.32 mm column with 320 nm 50% phenyl, 50% methyl polysiloxane stationary phase. A 1.85 m x 0.100 mm restrictor (deactivated fused silica) was used to control the Deans' flow within the modulator [49] [50] [51] and its output monitored with a flame ionization detector (FID). A passive three-way CFT splitter was used to divide the second-dimension effluent between a quadrupole mass spectrometer (MS, Agilent 5977c, Santa Clara, CA) and analytical FID with a split ratio of approximately 5% to the MS and the remainder to the FID. To enable the onboard pneumatic controls to achieve constant flow from the modulator through the second-dimension analytical train, the second column was installed as a composite column with the following dimensions: 5 m x 0.32 mm + 0.39 m x 0.2 mm.

Using Agilent's convention of expressing all flows as being normalized to 25°C and 1 atm, the first dimension was operated at 0.30 mL/min and second dimension at 9.28 mL/min. Both columns were held at a constant flow rate. The CFT RFF modulator internal sample loop volume was 0.037 mL. The modulator cycle period was 5.5 seconds with an injection time of 0.40 seconds. Shorter injection periods were found to incompletely flush the loop into the second dimension. Jet fuel samples were injected neat (0.4 µL) with a split ratio of 500:1 onto a 4 mm ID deactivated liner with deactivated glass wool. The gas saver feature was enabled such that the total first dimension flow changed to 25 mL/min two minutes after injection. Longer gas saver times were found not to increase peak areas for any components, indicating that evaporation completes before two minutes. The oven was held at 35°C for the first minute after injection and then ramped at 2.6°C/min to 300°C. Data were processed using GC Image version 2021r3.1 [52].

All fuels reported herein were analyzed within a few weeks on the same GCxGC instrument by the same operator using the same templates. All Tier 3 regions were inspected using the mass spectrometer before quantifying flame ionization detector data. Assignment of peaks to Tier 3 groups is likely the primary source of error for this method.

Figure *75* shows a violin plot for Tier 3 HTA groups. GCxGC data from CRC Report 647, which is contained in AFRL-RQ-WP-TR-2017-0091 [9], are missing the following Tier 3 groups

that were measured for this report: C3-C6 *n*-alkanes, tetracosane, C5-C6 *iso*-alkanes, C25 *iso*-alkanes, C5-C6 monocycloalkanes, C20-C21+ monocycloalkanes, C18+ dicycloalkanes, C13-C16+ tricycloalkanes, and C15+ diaromatics. A concentration of zero was assumed for these Tier 3 groups for visualization purposes. Also, the data were cut off below C7 and above C18 in the violin plot. The carbon number distribution in this report generally mirrored CRC Report 647. Many of the Tier 3 groups (i.e., specific molecular group and carbon number) have non-normal distributions. C10 and C11 *n*-alkanes had pronounced bimodal distributions that were not present in CRC Report 647. The slight bimodal distribution for C10 monocycloalkanes was mirrored by CRC Report 647. Violin plots aggregate data from 38 fuels, so bimodal distributions can be caused by either the collection of fuels or bimodal distributions within individual fuels. A visual inspection of the individual fuel GCxGC results indicates that the bimodal distributions in Figure *75* are caused by the aggregation of fuels and not by individual fuels with bimodal distributions. This report has a higher proportion of ≥C15 cycloalkanes and C15 cycloaromatics compared to CRC Report 647, possibly in part due to lack of reporting in CRC Report 647. There is a notable upshift in C12+ tricycloalkanes in the current survey compared to CRC Report 647. It is unclear if this upshift is real, or if it is due to GCxGC method improvements for the tricycloalkane regions between the two reporting periods.

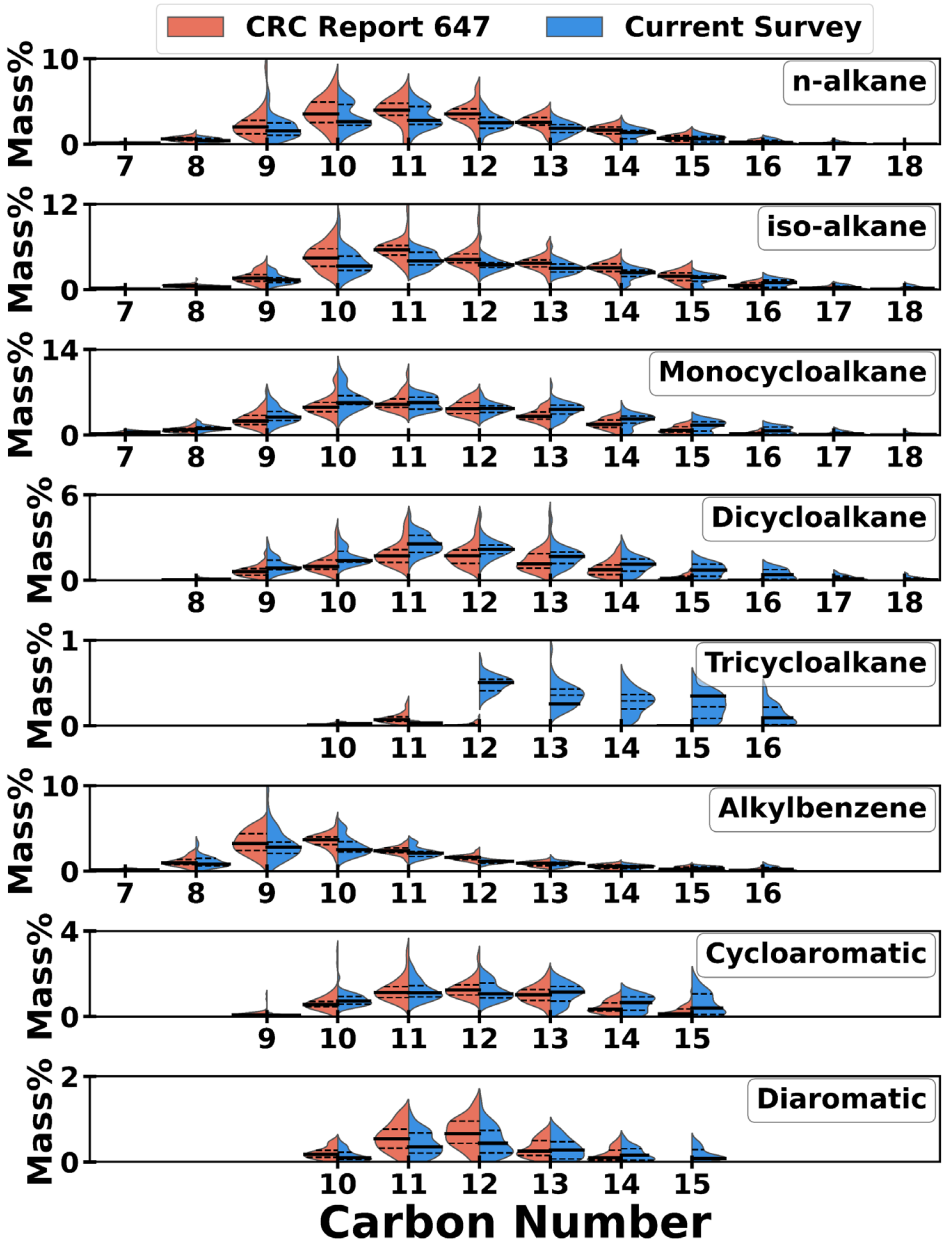

Figure 75. Violin plot for Tier 3 hydrocarbon-type groups.

Figure *76* shows a plot of cumene versus the total alkylbenzene mass%. Cumene, which is a C9 alkylbenzene, can be uniquely identified on the chromatogram (i.e., a Tier 4 identification). Cumene is listed as being “reasonably anticipated to be a human carcinogen” by the US Department of Health and Human Services [53]. Cumene has a strong correlation with the alkylbenzene mass% (R^2 of 0.73), indicating that fuels with a high alkylbenzene content pose

a higher threat of cumene exposure. A lower R^2 0.24 was achieved when cumene was correlated with the total aromatic mass%.

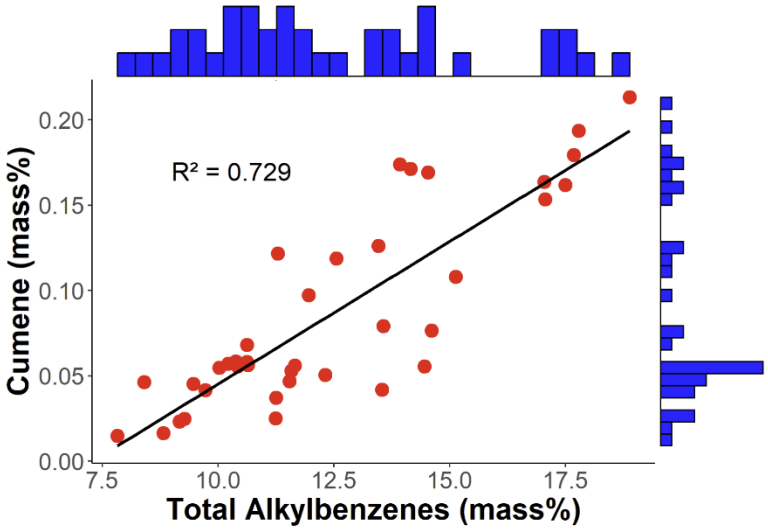

Figure 76. Scatter plot for cumene versus total alkylbenzene mass%. The distribution of the data is represented by the histograms along the axes.

Appendix B: Hydrogen Content

Figure *77* shows hydrogen mass% as calculated using GCxGC HTA versus hydrogen mass% measured by NMR. The hydrogen mass% is calculated for each Tier 3 HTA group from the total mass% of the Tier 3 group (i.e., carbon and hydrogen), stoichiometric number of hydrogens for the Tier 3 group, and molecular weight of the Tier 3 group. The calculated Tier 3 hydrogen mass% values are then summed to provide a total hydrogen mass% for the fuel. The HTA results tend to be lower than the NMR results, with a mean absolute difference of 0.2 mass%. There are two noticeable HTA outliers at 13.1 mass% and 14.8 mass% on an NMR basis. The fuel with 13.1 hydrogen mass% (CRC #33) had a relatively high concentration of alkylbenzenes and diaromatics compared to the median values from this survey. The high concentration of these aromatic species could have suppressed the hydrogen content of this fuel. The fuel with 14.8 hydrogen mass% (CRC #2) had a high concentration of monocycloalkanes and dicycloalkanes, which could have increased the hydrogen content. The high concentration of heavy aromatic species such as C16+ alkylbenzenes, C15+ cycloaromatics, and C15+ diaromatics would also increase the hydrogen content of CRC #2 relative to lighter aromatic species.

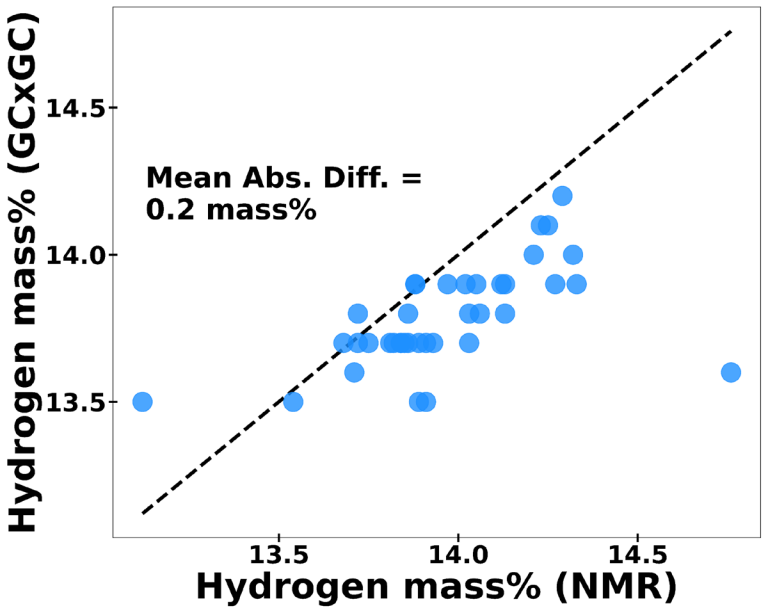

Figure 77. GCxGC versus NMR hydrogen content.

Appendix C: Coefficient of Thermal Expansion

CRC Report 647 reported density at 15.6°C (60°F). The median coefficient of volumetric thermal expansion (β) was calculated to correct the CRC Report 647 density values to 15°C for comparison with the current survey. β, as calculated using Equation *2* below [54], was 9.4×10^{-4} (°C)$^{-1}$. The density correction from 15.6 °C to 15 °C was performed using the coefficient of thermal expansion rather than the full ASTM D1250 procedure [55], due to the small temperature difference. 15°C and 20°C were used for T_1 and T_2, respectively. ρ_1 and ρ_2 were the densities at T_1 and T_2. $\bar{\rho}$ was the mean of ρ_1 and ρ_2. The coefficient of thermal expansion of 9.4×10^{-4} (°C)$^{-1}$ is lower than the value of 9.9×10^{-4} (°C)$^{-1}$ reported for kerosene-type jet fuels in the literature [56].

Equation 2: $\beta = \frac{\rho_1 - \rho_2}{\bar{\rho}(T_2 - T_1)}$

The CRC Report 647 density values were corrected to 15°C using the coefficient of thermal expansion calculated above and Equation 3 below. Values of 15.6°C and 15°C were used for T_1 and T_2, respectively. Since ρ_2 is not known, code was written to solve for it using a trial-error approach. ρ_2 values were iterated from 775 to 840 kg/m^3 with 0.01 kg/m^3 increments. The ρ_2 value producing the lowest error (i.e., LHS – RHS of Equation *3*) was then selected as the corrected value for each fuel in CRC Report 647. The median value from CRC Report 647 shifted from 801.9 kg/m^3 to 802.3 kg/m^3 when it was corrected from 15.6°C to 15°C.

Equation 3: $\rho_2 = -\beta\bar{\rho}(T_2 - T_1) + \rho_1$

Appendix D: Prediction of Cycloalkane Content

Measurements of cycloalkane content, which is important for materials compatibility [57] and energy density [58] among other properties, may not be available at refineries. Here, PLS regression was used to predict total cycloalkane content (i.e., mono + di + tricycloalkanes, as measured using GCxGC HTA) with methods commonly available at refineries. Specifically, density at 15°C (ASTM D4052), aromatic content (ASTM D1319), and 50% recovered (ASTM D86) were used as training features. RMSE and NRMSE values of 3.1 vol% and 7.5% were achieved, respectively, with a model using two latent variables. Figure *78* shows a parity plot for the cycloalkane regression. The data agree with the line of equality, with an R^2 of 0.65. The model coefficients indicate that density had a larger effect than aromatic content or 50% recovered for predicting cycloalkane vol%. The high outlier fuel at 35 vol% measured cycloalkanes was CRC fuel #14. This was a Jet A fuel with a D1319 aromatics value of 11 vol%. This is far lower than the mean aromatics value of 18%, which could lead to model instability.

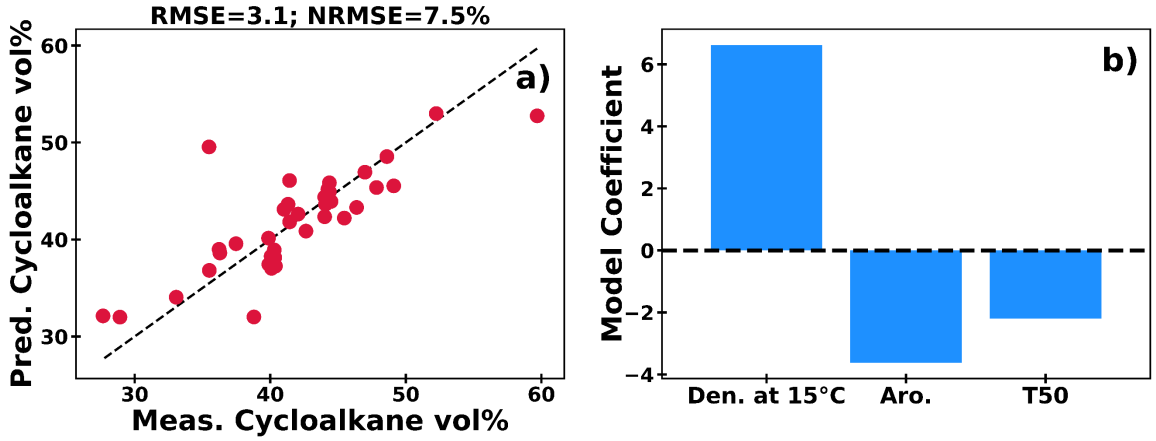

Figure 78. a) PLS cycloalkane vol% predictions made using density at 15°C (ASTM D4052), aromatic vol% (ASTM D1319), and 50% recovered (ASTM D86) as training features. b) Model coefficients for the PLS cycloalkane vol% model.

Equation 4 below is from the PLS regression, with cycloalkanes, density, aromatics, and 50% recovered in units of vol%, kg/m^3, vol%, and °C, respectively. The training data was not scaled for ease of use.

Equation 4: $Cyclo\% = (6.62 \times \rho) - (3.62 \times Aro\%) - (2.20 \times T50)$

Appendix E: SwRI Breakpoint Determination Method

The SwRI Breakpoint Method is the result of four decades of experience with Breakpoint Testing, and is shown in the below flow chart.

Breakpoint Test Sequence

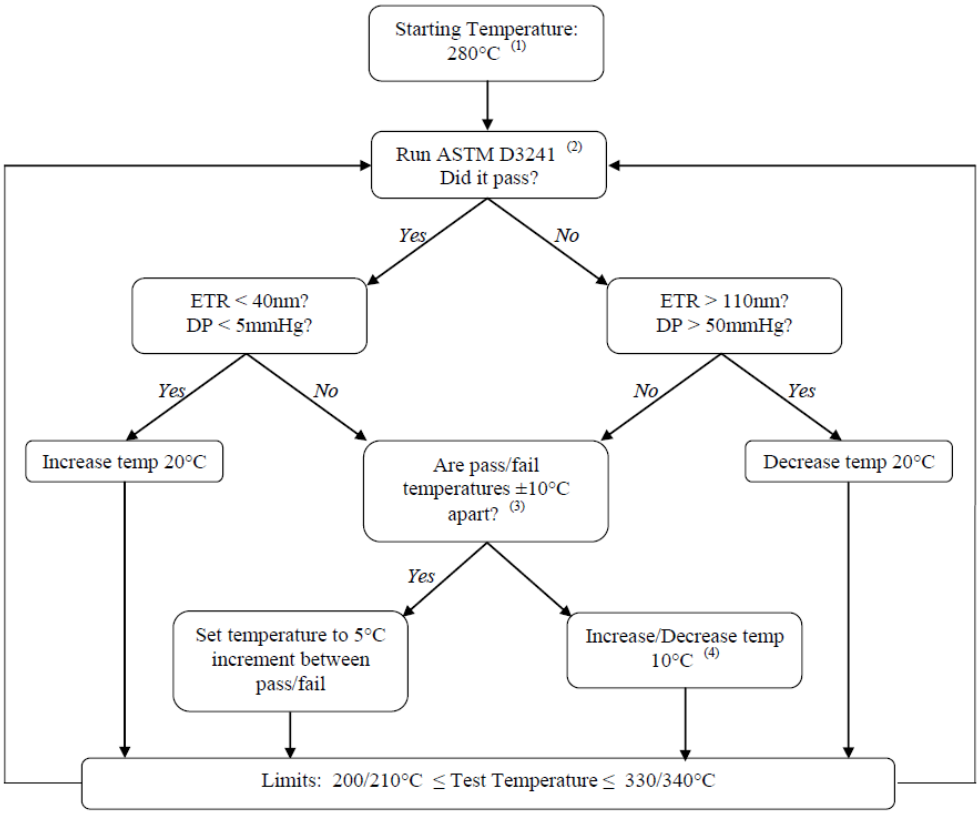

Notes:

1. 280°C is the typical starting point for unknown sample. If a sample already has a reported breakpoint value, start at that value.
2. Testing finished after the 5°C test run
   a. **The highest passing temperature is the breakpoint**
3. Pass/fail temperatures refer to the highest temperature that resulted in a pass and the lowest temperature that resulted in a fail, at this time.
4. If the previous test run passed, increase temperature 10°C. If the previous test run failed, decrease temperature 10°C.

Appendix F: QCM Deposition

To calculate QCM deposition, frequency versus time data were smoothed using a Savitzky-Golay filter with a window length of 49 and a polyorder of two. The start point was taken at the temperature steady state, and the deposition was calculated 15 hours later. To identify the temperature steady state, code was written that searched backwards from five hours to find the time where the temperature crossed +0.2°C above the mean operating temperature. The temperature was held at approximately 140°C for the 15 h time interval, and the sampling frequency was 0.016 Hz. QCM deposition was calculated using Equation 5 below [59]. The deposition was taken as the mean of five datapoints (15 hours ± 2 measurements).

Equation 5: $Deposition = -2.21 \times 10^5 \times \frac{f(t)-f_0}{f_0^2}$

Figure *79* shows a linear fit of the inverse of QCM deposition versus breakpoint. The correlation was moderate, with an R^2 value of 0.36. There was one low and one high outlier with breakpoint values >350°C. Spearman's rank correlation was used to assess the monotonicity of the two transformed measurements. There was a moderate positive correlation ($Spearman's\ \rho = 0.59$) which was found to be statistically significant ($p = 0.00$). In other words, as breakpoint increases, QCM deposition tends to decrease, albeit in a nonlinear fashion. This monotonic behavior was explored in greater depth a previous publication [60].

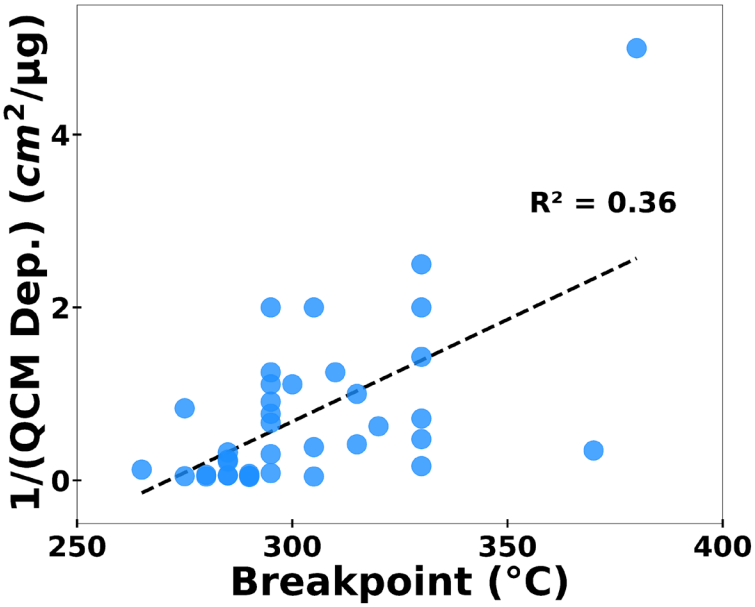

Figure 79. Linear fit of the inverse of QCM deposition versus breakpoint.

Appendix G: Air Solubility

Hydrocarbon chain length generally correlates positively with density and inversely with air solubility such that there is an overall inverse correlation between air solubility and density. Figure *80* shows oxygen solubility versus density at 24.8°C (assuming the air concentration of oxygen matches the standard U.S. atmosphere of 21%).

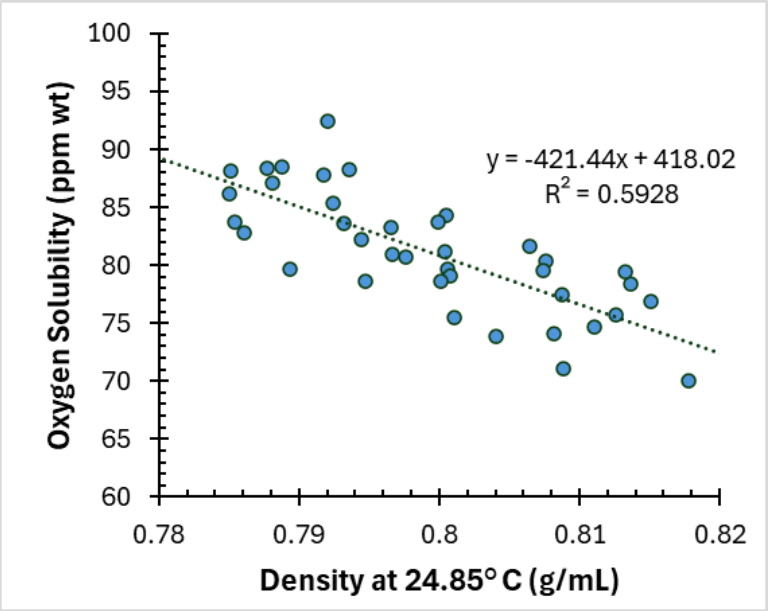

Figure 80. Oxygen solubility (ppm wt) versus density at 24.8° C (g/mL) assuming oxygen concentration in air of 21%. The dashed line and equation are the results of the linear least squares regression analysis.

Dissolved gas concentrations are a function of the gas solubility (i.e., the limit of saturation of air in a fuel), the hydrocarbon composition, and the composition of the gas. Plotting the individual dissolved gas concentrations from this study versus overall air solubility shows strong linear relationships (see Figure *81*). Here, air solubility is approximated as the sum of nitrogen, oxygen, and argon for each sample. The slopes of 0.64, 0.34, and 0.02—which represent the solubility of each gas relative to the total detected air concentration—do not align with the standard atmosphere values of 78% nitrogen, 21% oxygen, 0.9% argon by volume and by moles. Oxygen and argon are overrepresented, and nitrogen is underrepresented.

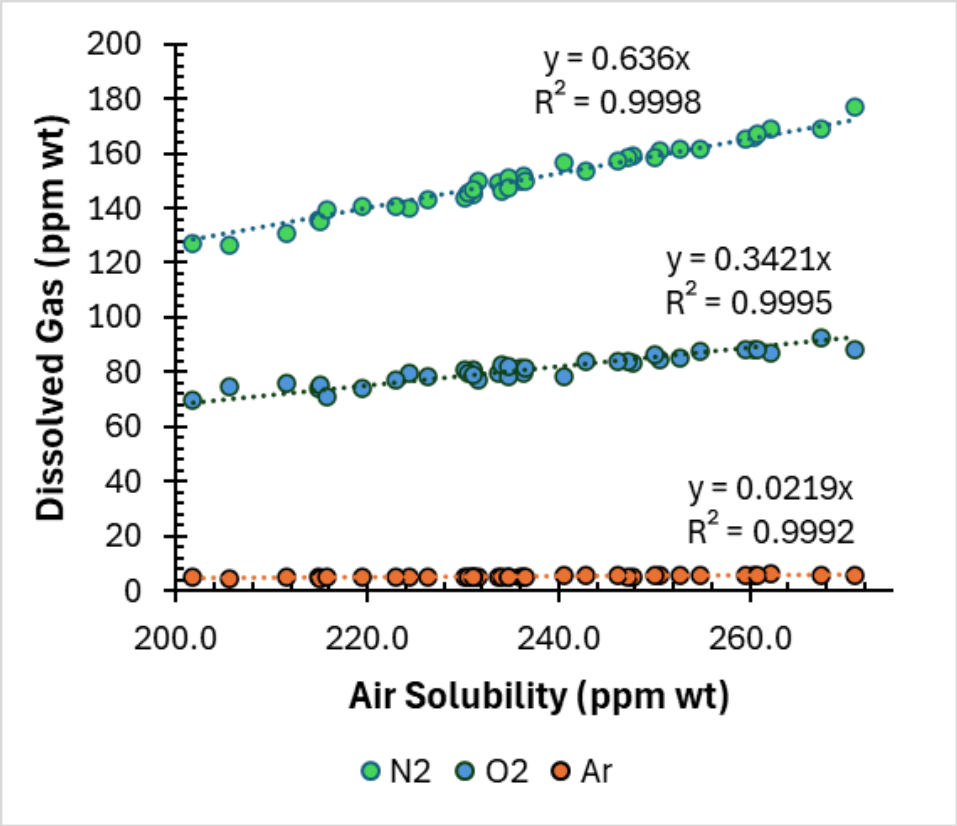

Figure 81. Dissolved gas concentrations plotted against air solubility. The dashed lines, equations, and regression coefficients are the results of linear least squares regression analysis.

Appendix H: Dielectric Constant versus Density

Figure *82* is a plot of density versus dielectric constant at 20°C, like ASTM D4054 Figure A1.8. The correlation was strong, with an R^2 value of 0.70. This aligns with the strong correlations shown in ASTM D4054 Figure A1.8.

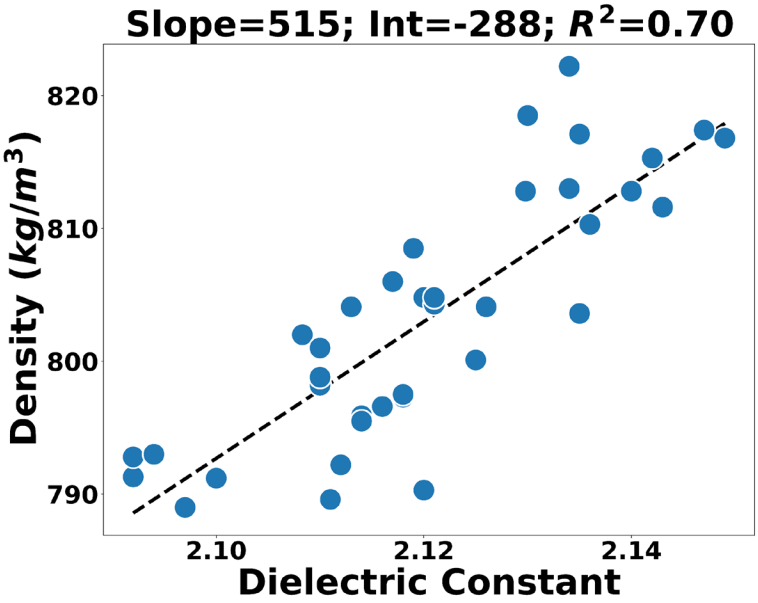

Figure 82. Density versus dielectric constant at 20°C.

Figure *83* shows a plot of gauging or Clausius-Mossotti intercept (a) versus slope (b). R^2 values were generated from linear regression versus temperature using Equation 6 [61]. The slope and intercept from Equation *6* are calculated by measuring dielectric constant and density over a range of temperatures, effectively modeling the temperature-dependence of these properties [58]. The Clausius-Mossotti slope was shown to distinguish between *n*-/*iso*-alkanes and aromatics, while the intercept provided further distinction between *n*-/*iso*-alkanes and cycloalkanes [61]. The contours in the plot represent areas where the combined ARINC Report 611-1 [62] and CRC Report 647 datasets have a KDE density greater than 0.01. Fuels below the 0.01 threshold are considered outside the typical range of the ARINC/CRC dataset. The ARINC/CRC data is also plotted as small grey circles. Two ARINC/CRC fuels with R^2 less than 0.90 were dropped before generating the plot. The results form a relatively narrow band, which the data from the current generally overlaps with. Two fuels from the current survey fell outside the ARINC/CRC contours at the lower right of the plot. R^2 values from the current survey were high, with all samples having R^2 values ≥ 0.99. The range of gauging slopes and intercepts in this report was 0.29-0.42 mL/g and 0.92-1.06 mL/g, respectively. This variation shows that conventional fuels can have a significant impact on gauging behavior. For reference, the range of

gauging slopes and intercepts for SBCs in the literature (i.e., alcohol-to-jet synthetic paraffinic kerosene and synthetic aromatic kerosene) was approximately 0.26-0.45 mL/g and 0.98-1.09 mL/g, respectively [61].

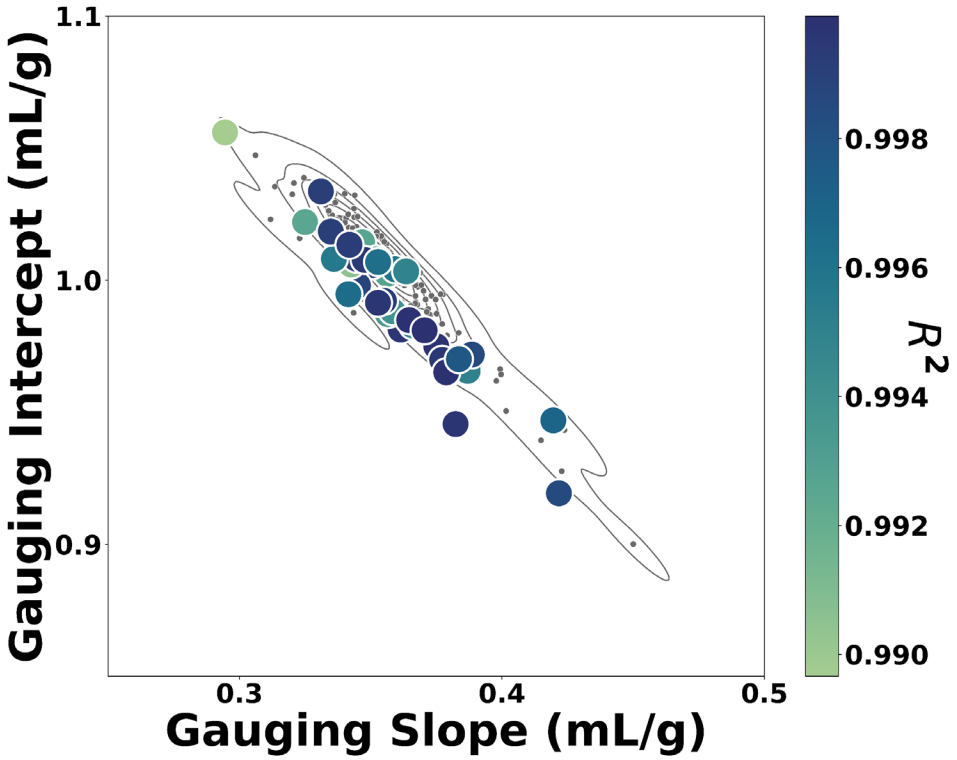

Figure 83. Dielectric constant gauging intercept versus slope. The colormap represents R^2 values from linear regression.

Equation 6: $\frac{K-1}{\rho} = b(K-1) + a$

The Lorentz-Lorentz one-third rule, which is detailed in the literature [45] [63], can be calculated using either the refractive index (LL_n) or the dielectric constant (LL_K) with Equation 7 and Equation 8.

Equation 7: $LL_n = \left(\frac{n^2-1}{n^2+2}\right)\frac{1}{\rho} \approx \frac{1}{3}$

Equation 8: $LL_K = \left(\frac{K-1}{K+2}\right)\frac{1}{\rho} \approx \frac{1}{3}$

LL_n has been validated for 12 crude oil samples, toluene, and α-methyl naphaltene in the literature [64]. LL_n and LL_K were also recently validated for one Jet A and four SBCs [45]. Figure *84* shows LL_K versus LL_n, which were calculated for the fuels in the current survey. The dashed lines are positioned at 1/3 on the x-axis and y-axis for reference. The fuels formed an ellipse with a few outliers at $LL_n < 0.330$ and $LL_n > 0.335$. Median LL_n and LL_K values were 0.333 ± 0.001 and 0.338 ± 0.002, respectively (± represents the standard deviation). It follows that the one-third rule was met for LL_n but not LL_K. The median LL_K may be above one third due to the presence of aromatics in the fuels, which was also the case for synthetic aromatic kerosene in the literature [45].

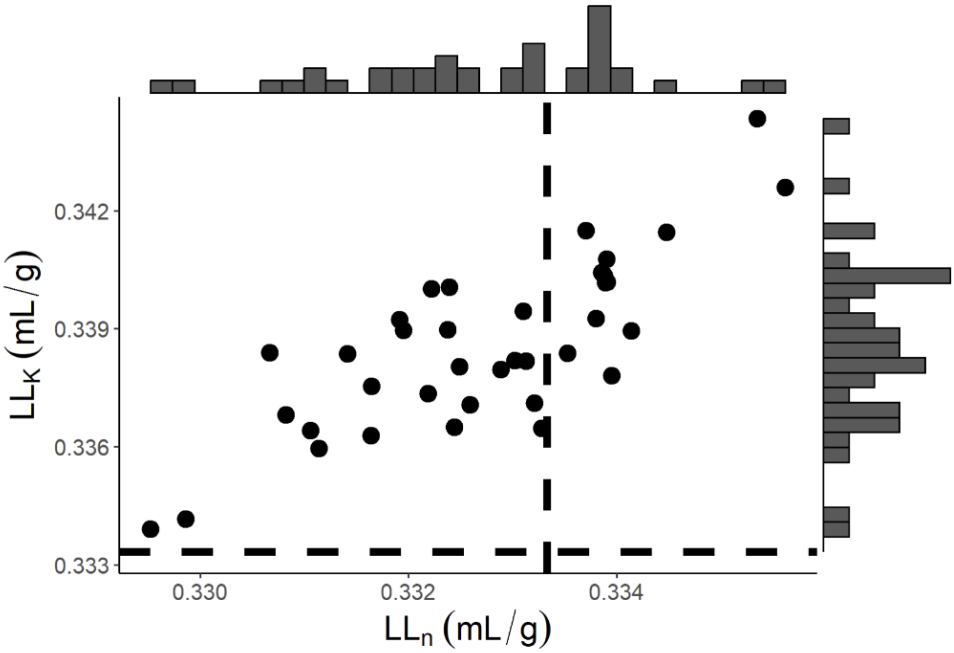

Figure 84. LL_K versus LL_n as calculated using Equation 7 and Equation 8.